Exploring the Ecohydrological Impacts of Woody Plant Encroachment in Paired Watersheds of the Sonoran Desert, Arizona

by

Nicole A. Pierini

A Thesis Presented in Partial Fulfillment
of the Requirements for the Degree
Master of Science

Approved March 2013 by the
Graduate Supervisory Committee:

Enrique R. Vivoni, Chair
Zhi-Hua Wang
Larry W. Mays

ARIZONA STATE UNIVERSITY

May 2013

ABSTRACT

Woody plant encroachment is a worldwide phenomenon linked to water availability in semiarid systems. Nevertheless, the implications of woody plant encroachment on the hydrologic cycle are poorly understood, especially at the catchment scale.

This study takes place in a pair of small semiarid rangeland undergoing the encroachment of *Prosopis velutina* Woot., or velvet mesquite tree. The similarly-sized basins are in close proximity, leading to equivalent meteorological and soil conditions. One basin was treated for mesquite in 1974, while the other represents the encroachment process. A sensor network was installed to measure ecohydrological states and fluxes, including precipitation, runoff, soil moisture and evapotranspiration. Observations from June 1, 2011 through September 30, 2012 are presented to describe the seasonality and spatial variability of ecohydrological conditions during the North American Monsoon (NAM). Runoff observations are linked to historical changes in runoff production in each watershed. Observations indicate that the mesquite-treated basin generates more runoff pulses and greater runoff volume for small rainfall events, while the mesquite-encroached basin generates more runoff volume for large rainfall events.

A distributed hydrologic model is applied to both basins to investigate the runoff threshold processes experienced during the NAM. Vegetation in the two basins is classified into grass, mesquite, or bare soil using high-resolution imagery. Model predictions are used to investigate the vegetation controls on soil moisture, evapotranspiration, and runoff generation. The distributed model shows that grass and mesquite sites retain the highest levels of soil moisture. The model also captures the

runoff generation differences between the two watersheds that have been observed over the past decade. Generally, grass sites in the mesquite-treated basin have less plant interception and evapotranspiration, leading to higher soil moisture that supports greater runoff for small rainfall events. For large rainfall events, the mesquite-encroached basin produces greater runoff due to its higher fraction of bare soil.

The results of this study show that a distributed hydrologic model can be used to explain runoff threshold processes linked to woody plant encroachment at the catchment-scale and provides useful interpretations for rangeland management in semiarid areas.

DEDICATION

This thesis is dedicated to my dad, Lou, my mom, Paula, and my brother, Sam, for their care, patience, never-ending support and love.

ACKNOWLEDGMENTS

I would like to thank my advisor Dr. Enrique Vivoni for the opportunity to pursue the research presented in this document and for his invaluable guidance, insight, and inspiration through this research work. I would like to also thank Ryan Templeton, Agustin Robles-Morua, and Cody Anderson for their immense help in installing and troubleshooting the environmental equipment. Special appreciation goes to the Army Research Office (ARO) for funding this research project. Additionally, I would like to thank the managers of the Santa Rita Experimental Range for their cooperation with this project and Russ Scott for his insight and guidance with the environmental equipment and data collection and providing datasets for comparative analysis or gap filling purposes. Lastly, I'd like to thank all members of the hydrology research group at Arizona State University for their support and encouragement.

TABLE OF CONTENTS

Page

LIST OF TABLES

Table Page

Table Page

LIST OF FIGURES

Figure Page

Figure Page

Figure Page

Figure Page

INTRODUCTION

Semiarid environments are important ecosystems that are distinctive of the southwestern United States. Semiarid systems are characterized by low annual precipitation, generally in the range of 250 to 500 mm, and high potential evapotranspiration. These environments are sensitive to landscape changes due to various factors, both natural and anthropogenic, such as overgrazing, increasing agricultural pressure, climate change, increases in CO_2 and N deposition, and wildfires (Archer, 1994; Scholes and Archer, 1997; Van Auken, 2009; Eldridge et al., 2011).

In the arid and semiarid environments of southern Arizona, annual precipitation falls in two separate rainfall seasons. The dominant rainfall season occurs in the summer months, typically July through September, and is characterized by highly localized, short, intense rainfall. This season is associated with the North American Monsoon (NAM) (Adams and Comrie, 1997). The second rainfall season occurs during winter months and is characterized by more widespread, longer, less intense rainfall. With the onset of the NAM, the hydrologic cycle is uniquely affected. Soil moisture is elevated and the short, intense storms become capable of producing runoff due to the intensity of precipitation exceeding the soil infiltration capacity, commonly known as Horton overland flow (Douglas et al., 1993; Gochis et al., 2006; Vivoni et al., 2008). Increases in soil moisture lead to decreases in sensible heat flux and increases in latent heat flux or evapotranspiration. The high evapotranspiration rates lead to less groundwater recharge and affect the amount of soil moisture in storage. In dryland ecosystems, evapotranspiration typically accounts for more than 90% of the total precipitation

(Wilcox et al., 2003); however the small differences in runoff can have large ecohydrological impacts. For these semiarid landscapes that are susceptible to change, it is vital to understand how water moves through the system. Several studies have explored hydrologic implications of changing landscapes within an ecosystem, such as under vs. between woody canopies (e.g., Breshears et al., 1998; Kurc and Small, 2004; Scott et al., 2004), or across a landscape (e.g., Browning et al., 2008; Huxman et al., 2005; Wilcox et al., 2003). However, there is a gap in understanding the ecohydrological dynamics at a catchment scale as well as the linkage between vertical and horizontal water and energy fluxes.

Woody plant encroachment is a worldwide phenomenon that has been observed in semiarid rangelands as they undergo a conversion from grasslands to savannas. This phenomenon has been well studied and documented in North America (e.g., Archer et al., 2001; Van Auken, 2000; Huxman et al., 2005; Browning et al., 2008), Australia (e.g., Burrows et al., 1990; Fensham, 1998), southern Africa (e.g., Moore et al., 1970; Burgess, 1995; Hudak and Wessman, 1998; Roques et al., 2001), and South America (e.g., Soriano, 1979; Silva et al., 2001). Woody plant encroachment can be defined as the increase in density, cover, and biomass of indigenous woody or shrub plants (Van Auken, 2009), and can be due to indigenous or invasive woody plants. Several hypotheses have emerged as the driver to encroachment. Grazing, for example, can lead to woody plant encroachment directly by reducing perennial grasses and so reducing competition or by spreading seeds (Brown and Archer, 1990; Harrington, 1991) or indirectly by reducing fire frequency and intensity (Savage and Swetnam, 1990; Archer, 1995; Oba et al., 2000).

The effect of woody plant encroachment in semiarid areas on the landscape properties has been widely researched as this shift may significantly alter the structure and function of these ecosystems (e.g., Archer et al., 2001; Van Auken, 2000, 2009). An important concern is to better understand how this phenomenon affects the components of the water cycle within semiarid ecosystems (Huxman et al., 2005) as water is the limiting resource for semiarid environments. It is also established that water is a primary control over net primary production in semiarid ecosystems (Ogle and Reynolds, 2004; Huenneke and Schlesinger, 2004; Turnbull et al., 2009). The implications of woody plant encroachment for both water and biogeochemical cycles are not well understood (Huxman et al., 2005). Turnbull et al. (2009) points out the importance of understanding the interactions between ecosystem structure and function at different stages during the transition from grassland to shrubland or woody plant encroached savannas. Huxman et al. (2005) explored two extreme vegetation possibilities for a given site: (a) little or no woody plant cover and (b) maximum woody plant cover that the landscape could maintain, however intermediate levels of woody plant encroachment and its ecohydrological effect were not explored. There is little insight on how runoff and soil moisture vary spatially and temporally during the transition stages from a grassland to a woody plant encroached savanna (Turnbull et al., 2009).

In semiarid ecosystems, vegetation patterns are important in controlling hydrologic processes and are subject to spatiotemporal changes. Infiltration, soil moisture, runoff generation, and evapotranspiration are all dependent on vegetation distribution (Breshears et al., 1998; Abrahams et al., 2003; Gutiérrez-Jurado et al., 2006; Mueller et al., 2007). First, woody plants can either increase or decrease soil infiltration

(Wilcox, 2002). They may increase infiltration via stemflow and preferential root channels, which could lead to more runoff. They may decrease infiltration and soil moisture by intercepting precipitation or by transpiring water that would instead reach the ground cover, leading to less runoff. Plant interception could cause a decrease in bare soil evaporation as the canopy acts as a barrier, or it may cause an increase if the encroachment leads to more bare ground cover. Woody vegetation can be expected to alter both surface and subsurface flow. More exposed soil surfaces may also be more susceptible to more runoff generation as the surface can become sealed and reduce infiltration (Scholes and Archer, 1997). Woody plant and grass coexistence may alter hydrologic variable differently. Grass cover can improve infiltration, but is more vulnerable to drought, grazing, and fire. Tree litter may also increase infiltration. Water may reach the stream channel through both surface and subsurface pathways (Dunne, 1978); therefore the explicit mechanisms of stream flow generation need to be identified so that the role of woody plant encroachment can be better known (Huxman et al., 2005). All hydrological implications are important as they can determine how best to manage these semiarid rangelands that are undergoing a conversion toward savannas.

There is a common perception that woody plant encroachment will lead to considerable changes in runoff generation, however there is no evidence that this is necessarily the case unless degradation or desertification processes are also taking place (Wilcox et al., 2006). Reducing or controlling woody plants has been suggested to increase stream flow (Bednarz et al., 2001; Lemberg et al., 2002), however a better understanding of the tree-grass interactions and coexistence is needed to determine if this is a proper management strategy. Soil moisture is a primary indicator to understanding

how grasses and woody plants may coexist as is the case in semiarid woody plant savannas. Soil moisture varies spatially and temporally and is important in describing the biotic response and their influence on hydrologic responses (Gosz, 1993; Huenneke and Schlesinger, 2004; Kurc and Small, 2007). Most roots of trees and grasses are in the upper soil horizons in semiarid systems because that is where water and nutrients are found. Scholes and Archer (1997) have stated that moisture in the subsoil has little influence on the covering of grass, instead only moisture in the superficial soil is important to it, and woody plants are favored by the moist subsoil. Woody plants will extract water for longer periods compared to grasses, and thus may reduce soil water content consistently throughout a year (Kemp 1983; Scott et al., 2006). Thus, it is important to highly characterize a system to explore the spatial variability and implications of soil moisture, possibly by using a distributed hydrologic model. Current knowledge lacks a comprehensive understanding of spatial and temporal controls on hydrologic patterns at the catchment scale.

Physically-based distributed hydrologic models have the capability to account for the spatiotemporal dynamics of soil moisture, precipitation, vegetation, soil attributes, and topography. Application of a distributed hydrologic model can aid in the understanding of the physical hydrologic processes with respect to catchment characteristics (e.g., Anderson et al., 2001; Ivanov et al., 2004a; Vivoni et al., 2007) In particular, the spatiotemporal patterns of surface and root zone soil moisture can be analyzed as they each affect runoff, infiltration, groundwater recharge, and evapotranspiration. Additionally, runoff generation patterns across the catchment can be evaluated relative to soil and vegetation types and topographic features. Analysis of the

hydrologic distribution can help identify key vegetation or soil characteristics that stem from woody plant encroachment and alter runoff or other hydrologic processes.

This study features two small rangeland watersheds that are located in the Santa Rita Experimental Range in the Sonoran desert in southeast Arizona, and are representative of this ongoing landscape shift of grassland to woody savanna. This unique paired catchment study allows for a comparison of two watersheds with similar characteristics in terms of slope, aspect, soils, area, and climate as they are located adjacent to one another. The encroaching woody plant species is *Prosopis velutina,* commonly known as the velvet mesquite tree. One catchment has undergone a mesquite tree removal process while its paired catchment has continued its shift from a grassland to a savanna. This study focuses on the NAM season, as both watersheds have historically generated more than 90% of annual runoff between July and September. The study area receives approximately 55% of the annual rainfall falls during the NAM season. Using high temporal resolution datasets, a fully distributed hydrologic model is applied to help describe the actual hydrologic mechanisms that are taking place in the catchments. Based on this effort, this thesis has the following main objectives:

1. To understand the spatial and temporal variability of watershed-scale hydrologic and energy states and fluxes using a dense environmental sensor network in a semiarid woody plant encroached system.
2. To examine soil moisture and temperature variability across watershed vegetation patterns, topography, and soil variability at different depths during the NAM season.

3. To develop two site-calibrated paired watershed-scale models using the TIN-based Real-Time Integrated Basin Simulator (tRIBS) to explore the hydrologic fluxes across the watershed during the NAM season, specifically the spatiotemporal variability of soil moisture with respect to woody plant encroachment.
4. To investigate the impact of woody plant encroachment on runoff generation using tRIBS and identify a possible threshold with respect to rainfall events during the NAM that lead to more or less runoff generation between the paired, mesquite-treated and mesquite-encroached, basins.

Few studies have explored the ecohydrological impacts of woody plant encroachment at the catchment scale (Nie, W. et al., 2012). The distributed hydrologic model coupled with comprehensive observations from the dense environmental network allows for a thorough analysis of hydrologic fluxes and runoff generation. The model is capable of identifying spatial patterns of runoff generation during the NAM season in the basins. Prior studies on woody plant encroachment have conflicting results as to whether encroachment causes more or less runoff generation. Understanding the ecohydrological states and fluxes during the NAM brings awareness to possible storm event thresholds that result in either more or less runoff at the mesquite-treated basin and the mesquite-encroached basin. A better comprehension of what ecosystem functions change with woody plant encroachment and how they affect the water budget will benefit rangeland management decision-makers as the landscape continues to change.

METHODS

2.1 Site Description

The study area is located on the Santa Rita Experimental Range (SRER), approximately 45 km south of Tucson, AZ. The range represents the Sonoran Desert and varies from 900 to 1400 meters in elevation. The SRER was established in 1902 with the purpose of desert rangeland management and ecology research. The primary land use on the range for the past century has been cattle grazing. In the past century, the rangeland has undergone a shift in vegetation from a semi-desert grassland into a savanna due to the encroachment of the woody leguminous tree, *Prosopis velutina* Woot., or velvet mesquite (common name), (McClaran, 2003). The U.S. Department of Agriculture, Agricultural Research Service (USDA-ARS) established eight watersheds in 1975, ranging in area from 1.1 to 4.0 ha, to support hydrology research. The goal was to quantify the interaction of rainfall intensity patterns, soils, vegetation, and management on the rates and amounts of runoff and sediment production (Stone et al., 2008). Each watershed was instrumented to measure rainfall, with a rain gauge at each site, runoff, through an outlet flume at each site, and sediment, which provides a long term record of rainfall and runoff measurements at our study sites. Additionally, the eight watersheds were paired to investigate the effects of different vegetation treatments on hydrological processes. Our study area consists of a pair of these watersheds, Watershed 7 and Watershed 8, located on the eastern side of the range at approximately 1,160 meters in elevation, and shown in Figure 1. Watershed 7 is approximately 10,790 square meters (1.079 ha) and watershed 8

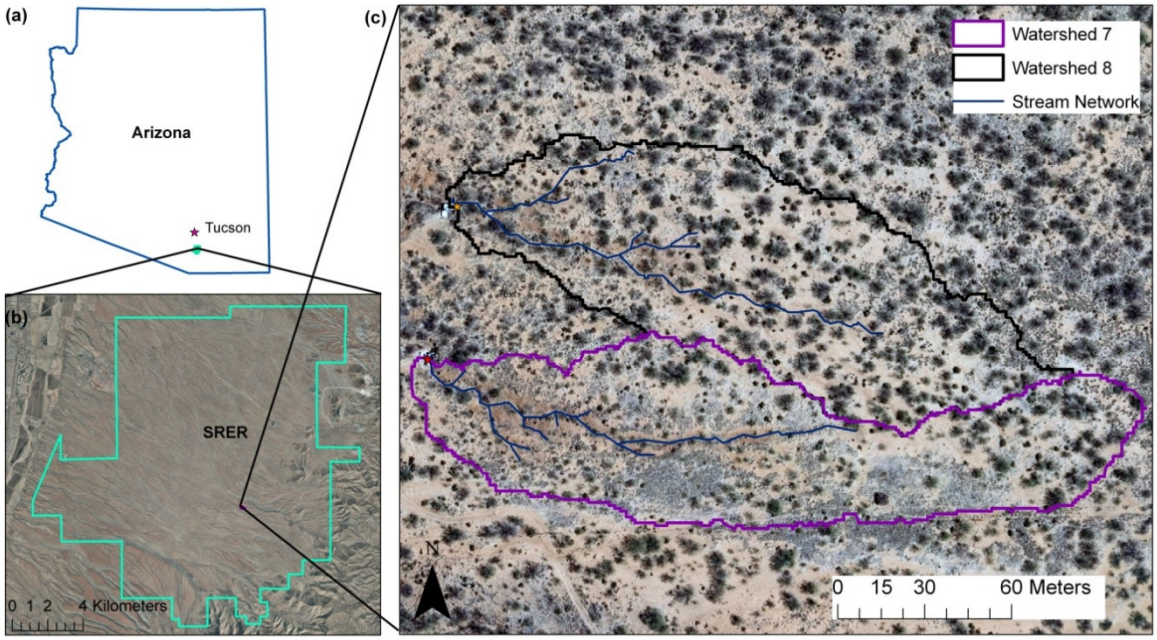

Figure 1: Location of watersheds 7 and 8 south of Tucson, AZ, shown in (a), within the Santa Rita Experimental Range (SRER), shown in (b). Boundaries and stream networks were determined through digital elevation map (DEM) analysis and confirmed with manual GPS sampling, and are shown in (c). The aerial image was obtained through a light and detection ranging (LiDAR) data acquisition flight.

is approximately 10,975 square meters (1.098 ha). In 1974, watershed 7 was treated to remove mesquite by applying diesel oil basally, with reapplication as needed to keep the watershed mesquite free (Martin and Morton, 1993). Based on field assessments, mesquite treatment was effective but encroachment is occurring on the previously treated watershed.

2.2 Watershed Characterization

A light detection and ranging (LiDAR) data acquisition flight took place in April 2011, and the sampling extent is shown in Figure 2. LiDAR technology uses pulses from a laser to measure the distance to a certain target. It is able to measure the bare earth

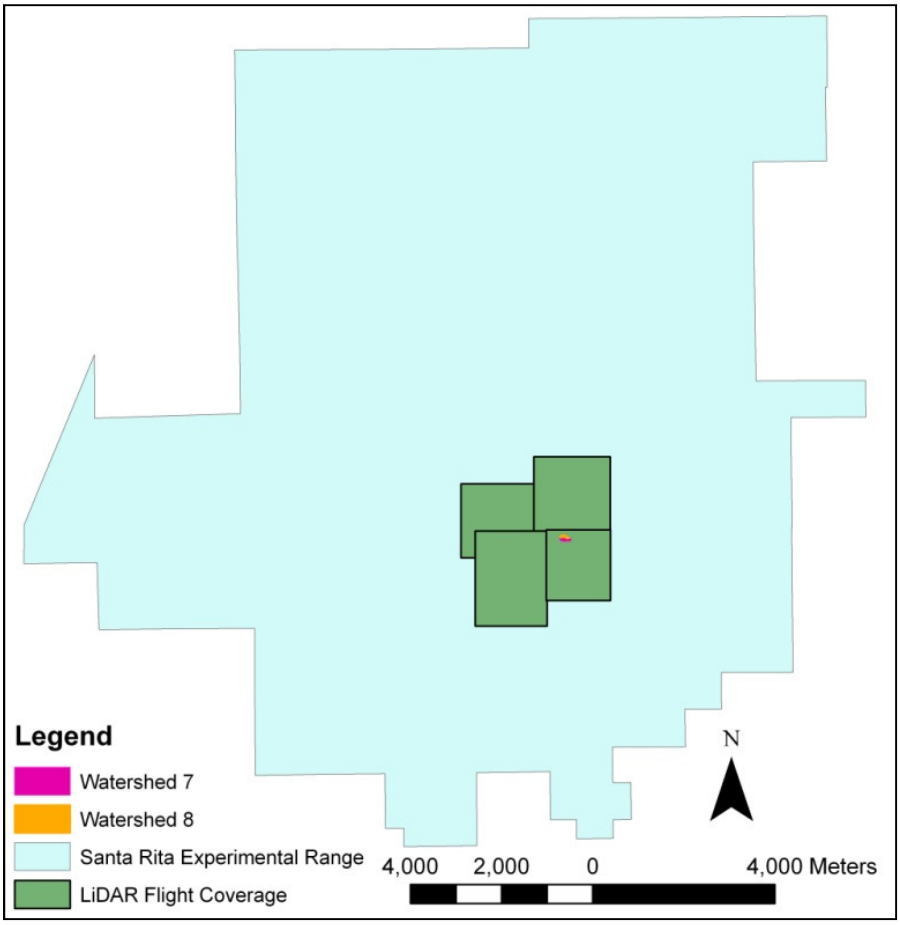

Figure 2: The sampling extent of the light detection and ranging (LiDAR) data acquisition flight within the Santa Rita Experimental Range (SRER).

elevation as well as the elevation of the canopy heights. LiDAR points were taken at a 0.183 meter resolution, allowing a 1 meter bare earth digital elevation model (DEM) and a 1 meter earth with canopy elevation model to be derived. This dataset was utilized to delineate the watershed boundaries upstream of each outlet flume. Ground dGPS (differential Global Positioning System) points were taken using a Leica Geosystems GPS 1200 to map each watershed's ephemeral stream network as well as the boundaries for each watershed. Furthermore, the dataset allowed further topographic analysis of each watershed, such as slope, aspect, and curvature, and a comparison of canopy heights

Table 1: Soil texture analysis at the watershed site at three different depths averaged across the different sampling locations.

Averages	Sand %	Silt %	Clay %
5 cm	64.56	24.80	10.64
15 cm	70.74	20.80	8.46
30 cm	75.63	17.74	6.63

between the two basins. Due to their proximity and similar characteristics, the watersheds provide a fair comparison to one another, and their topographic characteristics are shown in Figure 3. The mean elevation as determined from the LiDAR data for watershed 7 and watershed 8 is 1,166.79 m and 1,166.10 m, respectively. The average slope at watershed 7 is 2.39° and at watershed 8 is 2.26°. Both watershed 7 and watershed 8 have westerly aspects.

The soils at the watershed are characterized as coarse-textured sandy loam derived from Holocene-aged alluvium eroded from the nearby Santa Rita Mountains (Potts et al., 2010). Soil sampling was conducted at multiple locations within our study site (21) at depths up to 30 cm and one site at depths up to 1 m. Soil texture analysis for several samples at three different depths, 5 cm, 15 cm, and 30 cm, and one sample at 50 cm, 75 cm, and 1 m, confirmed that the dominant soil type is sandy loam. The results from the soil texture analysis are shown in Table 1. The procedure followed is further explained in Appendix D.

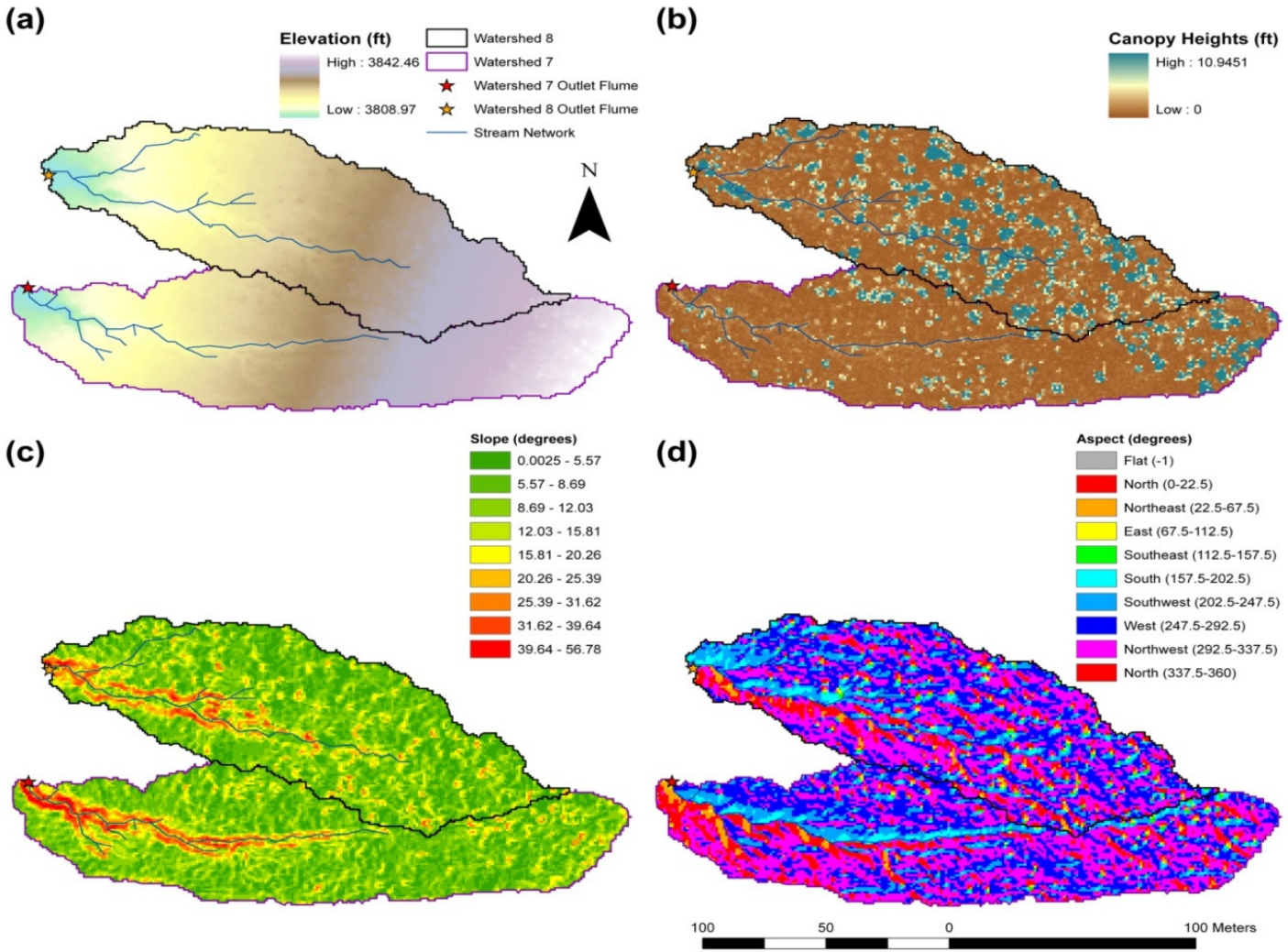

Figure 3: Topographic characterization of both catchments as determined from the DEM obtained from the LiDAR flight. Each watershed delineation boundary and stream network is shown in addition to (a) elevation (b) canopy heights (c) slope in degrees, and (d) aspect in degrees.

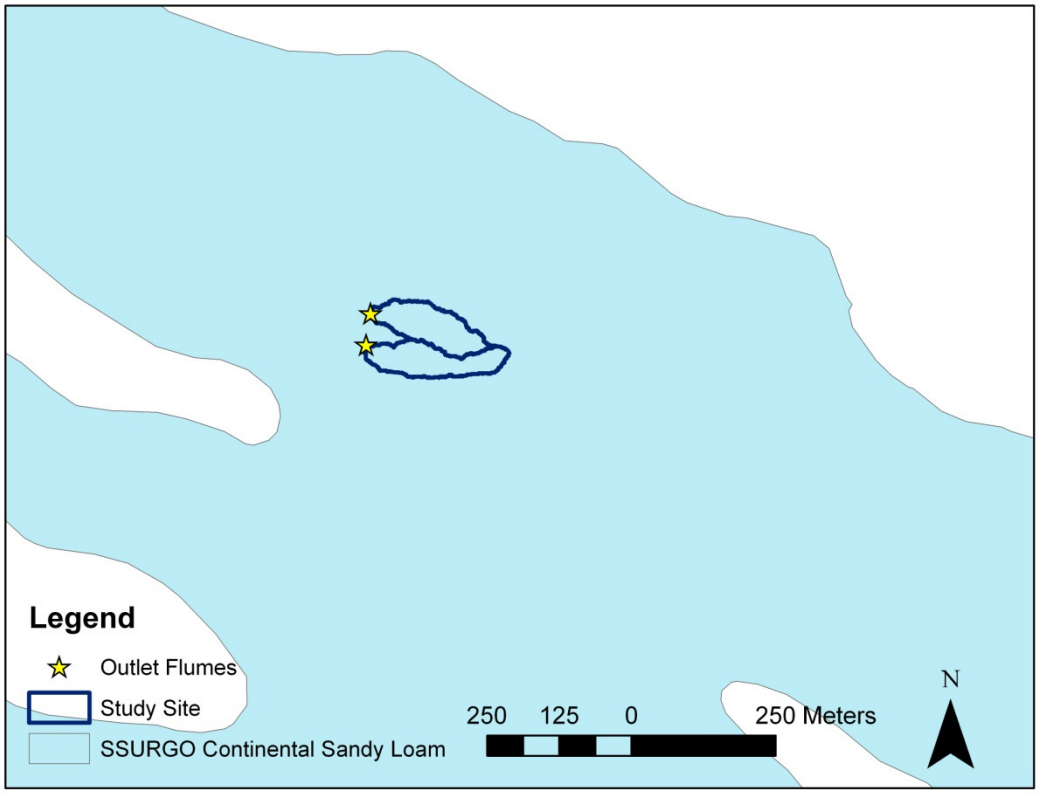

Figure 4: SSURGO data extent relative to watershed 7 and 8 locations, verifying a soil classification of continental sandy loam.

To further verify the sandy loam classification, SSURGO (Soil Survey Geographic Database) data was evaluated. The extent of Continental Sandy Loam is shown in Figure 4. The different particle size percentages associated with this soil type are 66.0% Sand, 23.0% Silt, and 11.0% Clay, which matches fairly well with the lab analysis.

Vegetation at the study watersheds consists of the non-native velvet mesquite (*Prosopis velutina* Woot.), perennial non-native Lehman lovegrass (*Eragrostis lehmanniana* Nees.), warm-season perennial bunchgrasses (black gramma (*Bouteloua eriopoda* Torr.), Arizona cottontop (*Digitaria californica* Benth.), Santa Rita threeawn

Table 2: Summary of vegetation classifications as determined from the LiDAR ortho-image for both watershed study sites.

Vegetation Type	Watershed 7	Watershed 8
Grass (%)	61.47	44.09
Mesquite (%)	19.17	31.98
Bare Soil (%)	19.36	23.93

(*Aristida glabrata* Vasey.)), and cacti (cholla (*Opuntia spinisor* Engelm.), prickly pear (*Opuntia engelmanni* Salm-Dyek.), fishhook barrel (*Ferocactus wisilizenii* Britt.)), (Polyakov et al., 2010).

An ortho-image was also obtained from the LiDAR flight. The image was taken at a 30 cm resolution. ArcGIS was utilized to classify the image into vegetation types. Points where the vegetation was easily recognized were used to reclassify the image based on the color bands associated with the distinguishable points. The vegetation was identified and generalized into three classifications: Mesquite, Grass, and Bare Soil. These vegetation classifications were later employed in the hydrologic model. Table 2 summarizes the classification percentages of the vegetation types in each watershed. Figure 5 shows the vegetation classes and the development of the classes from the LiDAR ortho-image.

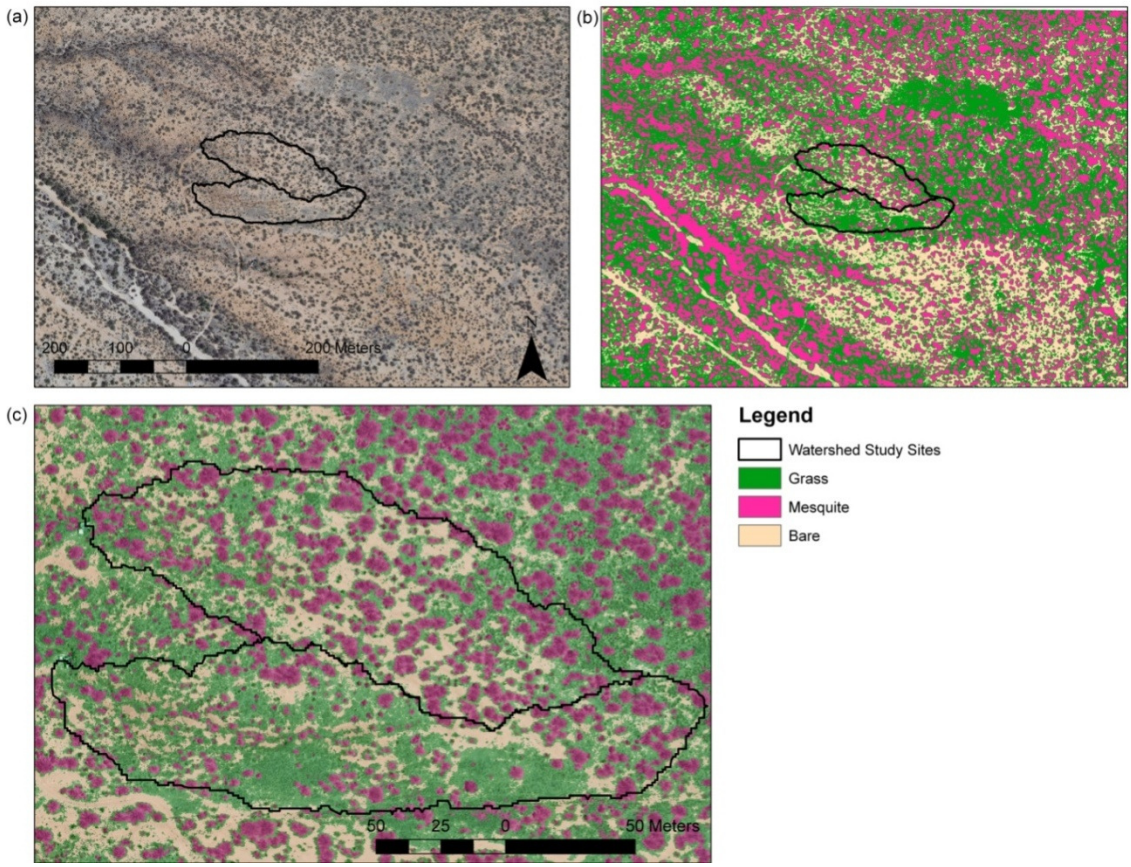

Figure 5: Utilization of the LiDAR ortho-image, shown in (a), to obtain a vegetation classification map based on three different vegetation types: Grass, Mesquite, or Bare Soil, shown in (b). An overlay of the ortho-image and vegetation classification is shown in (c) to display the vegetation classification accuracy relative to the ortho-image.

2.3 Environmental Sensor Network

An essential component in quantifying hydrological states and fluxes at the catchment scale is to measure hydrological variables at a high temporal and spatial resolution. A dense environmental sensor network was installed at watershed 8 in May 2011 to measure rainfall, runoff, soil moisture and temperature, and meteorological variables. Table 3 gives a summary of the sensors, sensor ID's, locations, and elevations. Figure 6 shows the sensor locations relative to the two study basins.

Table 3: Sensor locations and identifiers within the watershed study sites for all installed instrumentation. Locations of sensors are in the following coordinate system: UTM – WGS 1984, 12N.

Sensor Type	ID	Northing (m)	Easting (m)	Elevation (m)
Rain Gauges	RG1	3520152.894	513985.591	1164.488
	RG2	3520152.135	514038.895	1166.495
	RG3	3520120.183	514088.655	1168.396
	RG4	3520124.596	514132.724	1169.717
	RG_Tower	3520199.391	514120.715	1168.323
	RG_ARS	3520123.864	513968.864	1161.085
Flumes	F1	3520153.197	513955.513	1162.570
	F2	3520139.551	513990.919	1164.195
	F3	3520124.217	514035.176	1166.462
	F_Outlet	3520154.279	513942.385	1161.951
Eddy Covariance Tower	ECT	3520195.491	514119.008	1168.292
Soil Moisture and Temperature Probes	T1-012	3520180.433	513984.636	1164.501
	T1-345	3520165.871	513984.154	1164.421
	T1-678	3520155.225	513988.730	1164.618
	T1-9AB	3520139.297	513987.001	1164.076
	T1-CDE	3520123.799	513988.101	1165.005
	T2-012	3520181.507	514036.234	1166.068
	T2-345	3520165.854	514038.309	1166.301
	T2-678	3520149.628	514036.022	1166.399
	T2-9AB	3520140.206	514040.170	1166.580
	T2-CDE	3520127.189	514040.652	1166.794
	T2-GHI	3520112.458	514042.364	1167.464
	T3-012	3520148.198	514082.881	1167.876
	T3-345	3520133.885	514085.532	1168.146
	T3-678	3520119.872	514089.696	1168.438
	T3-9AB	3520106.638	514089.951	1168.585
	T3-CDE	3520091.232	514092.007	1168.794
	T4-012	3520152.376	514123.468	1169.085
	T4-345	3520137.891	514128.390	1169.435
	T4-678	3520121.899	514136.050	1169.856
	T4-9AB	3520111.430	514138.004	1170.062
	T4-CDE	3520097.097	514142.520	1170.408

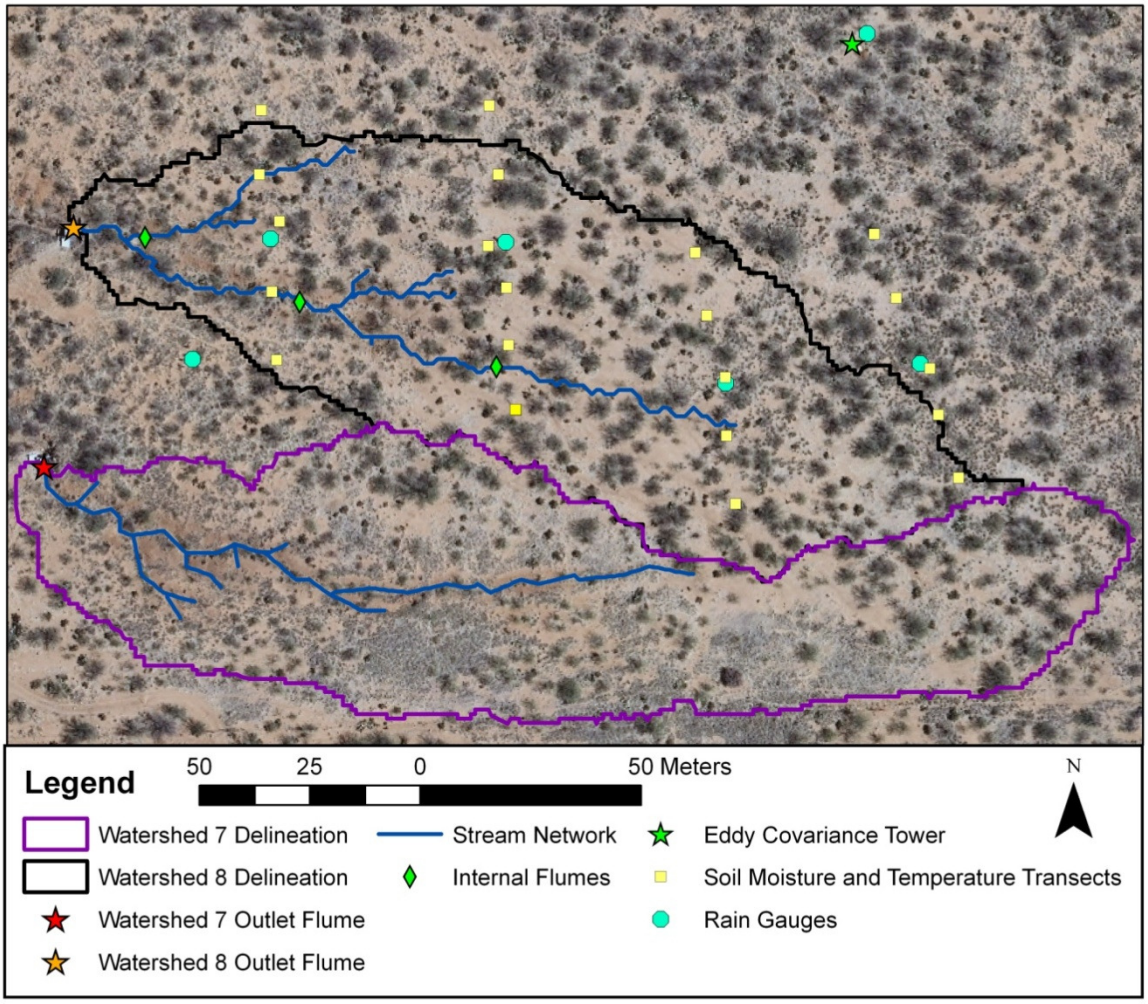

Figure 6: Environmental network sensor locations including both watershed outlet flumes, which are managed by USDA-ARS, 6 rain gauges, 3 internal flumes, 21 soil moisture and temperature measurements at three different depths (5 cm, 15 cm, and 30 cm) and an eddy covariance tower.

Four parallel transects running north to south, approximately 100 meters from one another, were established to measure soil moisture and temperature across the watershed. Three transects consisted of 15 soil dielectric sensors (Stevens Water Monitoring, Hydra probe) with five sensor locations, running approximately 200 meters north to south, while one transect consisted of 18 soil dielectric sensors and six sensor locations, running 250 meters north to south. The sensors are able to determine the dielectric permittivity of soil

by measuring reflected voltages. With the dielectric permittivity, the probe can simultaneously measure soil moisture and electrical conductivity. The signal response is converted to soil moisture and temperature using built-in algorithms. The Hydra probes connect to a datalogger through a SDI-12 data port. At each sensor location there were three Hydra probes measuring at 5 cm, 15 cm, and 30 cm depths. The goal was to distribute the probes relatively equally among the three different vegetation types along the four established transects spanning the basin. The soil moisture and temperature measurements were collected as 30 minute averages.

Tipping bucket rain gauges (Texas Electronics, TE525MM) allowed for instantaneous sampling of rainfall. One rain gauge was installed at each transect, plus one rain gauge at the eddy covariance tower location outside of the basin. Additionally, the USDA-ARS operates a high-resolution weighing type rain gauge which lies between watershed 7 and watershed 8. This setup provides 6 rain gauges to describe the spatial distribution of rainfall at the watershed site. Each gauge was mounted at 1 meter above ground in a clearing to negate any interception effects from surrounding vegetation.

Three trapezoidal flumes were installed to measure interior flow in the basin in addition to channel flow being measured at the outlet flume, which had been installed and maintained by the USDA-ARS. The flume dimensions are specified in Appendix A. These flumes were developed and constructed at the Jornada Experimental Range for surface flow research applications (Wainwright et al., 2002). To measure runoff with the flume, pressure transducers (Campbell Scientific, CS450) were installed in the stilling wells of each flume, and took pressure measurements every minute. Calibration curves

were produced for each internal flume that related the pressure measurements to height of water in the flume and are further explained in the data processing section.

To measure meteorological variables, a 10 meter eddy covariance tower was installed approximately 20 meters north of the watershed. The tower is primarily used to measure heat, water, and carbon fluxes, as well as other meteorological variables. Measurements included a precipitation using a tipping bucket rain gauge (Texas Electronics, TE525) mounted at 1 meter; soil surface temperature (Apogee Instruments Inc, SI-111 Infrared Radiometer); two sets of 2 and 4 cm depth soil temperature representing a bare soil area and a vegetation shaded area (Campbell Scientific, TCAV-L, Thermocouple); two sets of soil heat flux at 5 cm depth representing a bare soil area and a vegetation shaded area (Hukseflux, HFP01-SC, Self-Calibrating Soil Heat Flux Plates); volumetric soil moisture at 5 cm, 15 cm, 30 cm, 50 cm, 75 cm, and 100 cm depth (Campbell Scientific, CS616); barometric pressure (Setra, CS100); air temperature and humidity at a 1.5 meter height (Campbell Scientific, HMP45C); net long and short wave radiation at a 5 meter height (Kipp and Zonen, CNR2-L, Net Radiometer); incoming solar radiation at a 5 meter height (Kipp and Zonen, CMP3, Pyranometer); and sensible heat, latent heat and carbon fluxes using H_2O and CO_2 concentrations (LICOR, LI7500, Open-Path Infrared Gas Analyzer) sonic temperature, and the three components of the wind velocity vector (Campbell Scientific, CSAT7500, Sonic Anemometer), measured at a 7 meter height. Precipitation measurements were taken instantaneously. The CO_2 and H_2O concentrations and wind velocities were all sampled at a 20 Hz frequency. All other

measurements were recorded as averages over 30 minutes or sampled at 30 minute intervals.

2.4 Data Processing

All of the raw data collected from the environmental sensor network was carefully processed. The soil moisture and temperature sensors on the transects (Stevens Water Monitoring, Hydra probe) were corrected to the site specific soil. These corrections were performed using representative soil samples taken near the site up to a depth of 30 cm. The procedure developed and followed is further explained in Appendix B.1. The probes are factory calibrated to measure 'loam soil' types. The correction allowed the transformation of the soil moisture values measured in the field to the actual soil moisture for the sandy loam soil at the site. The correction developed is:

$$Soil\ Moisture_{C\_HP} = \left(\frac{Hydra\ Probe\ Reading}{0.7983}\right)^{1.27845} \qquad \text{Equation 1}$$

where the Hydra probe reading is the volumetric soil moisture from the field (m^3/m^3) with the factory calibration and the Soil $Moisture_{C\_HP}$ is the actual soil moisture (m^3/m^3).

A similar procedure was followed for the volumetric soil moisture sensors (Campbell Scientific, CS616) near the eddy covariance tower. A correction equation was developed to transform the field measured soil moisture values to the site specific soil type, and is:

$$Soil\ Moisture_{C\_616} = 0.1944 * ln(CS616\ Reading) + 0.5749 \qquad \text{Equation 2}$$

where CS616 Reading is the volumetric soil moisture from the field (m^3/m^3) with the factory calibration and the Soil $Moisture_{C\_616}$ is the actual soil moisture (m^3/m^3) given the study area's soils.

The rain gauges (Texas Electronic, TE525 and T525MM) were statically and dynamically calibrated upon installation. To statically calibrate the rain gauges, known volumes of water were dripped into the tipping bucket to ensure the accuracy of the individual tip volumes. Dynamic calibration was performed by using nozzles that released water into the tipping buckets at different rates.

The pressure transducers (Campbell Scientific, CS450) measure pressure within the stilling wells for each internal flume. Each pressure transducer was calibrated at each flume upon installation, following the procedure as outlined in Templeton (2010). For calibration, water height was measured in each flume and recorded with the pressure (psig) reading from the pressure transducer. A linear calibration curve was then created following the general form of:

$$h=m*p+b \qquad \text{Equation 3}$$

where h is the height of the water in the flume (cm), m is the rate of change of height with pressure change (cm/psig), p is the measured pressure (psig), and b is the height offset (cm). To calculate individual hydrographs for each storm event, a normalization constant was necessary due to the effect of diurnal fluctuations on the pressure transducers. The standard procedure was to set the height reading at 0 cm approximately 2 minutes before precipitation was recorded for the storm event. The normalization constant required to set the height reading to 0 was applied to all pressure transducer

values from that point to approximately 30 minutes after the last precipitation amount was recorded. The calibration equation developed was then applied to these normalized pressure transducer values. The International Organization for Standards (ISO) protocol 4359 was followed to determine flow rates at each internal flume based on flume dimensions and water height for a trapezoidal flume. Equations were developed for each internal flume using the water height to find the flow rate, and are specified here:

$$Q \text{ (flume 1)} = 10.299x^2 + 0.1176x + 0.0174 \quad \text{Equation 4}$$

$$Q \text{ (flume 2)} = 10.333x^2 + 0.3177x + 0.0013 \quad \text{Equation 5}$$

$$Q \text{ (flume 3)} = 11.051x^2 + 0.257x + 0.0006 \quad \text{Equation 6}$$

where x represents the water height in the flume (cm) as determined from the calibration relations for each pressure transducer.

The CO_2 and H_2O concentrations and the wind velocities measured in three dimensions were filtered for spikes, instrument malfunction, and rainfall periods. Using the EdiRe software tool (The University of Edinburgh), the high resolution measurements then underwent a sequence of processing steps. Signal lag was removed and the data was averaged over 30 minute intervals. The coordinate frame was then rotated (Lee et al., 2004), and stability and density fluctuations (Webb et al., 1980) were corrected for prior to calculating the final fluxes. The sonic temperature was used to calculate the sensible heat flux (Schotanus et at., 1983). Negative latent heat fluxes were set to equal zero. The finalized fluxes were visually inspected for out of range values, which were removed, and linear interpolation was used to fill short periods of missing data.

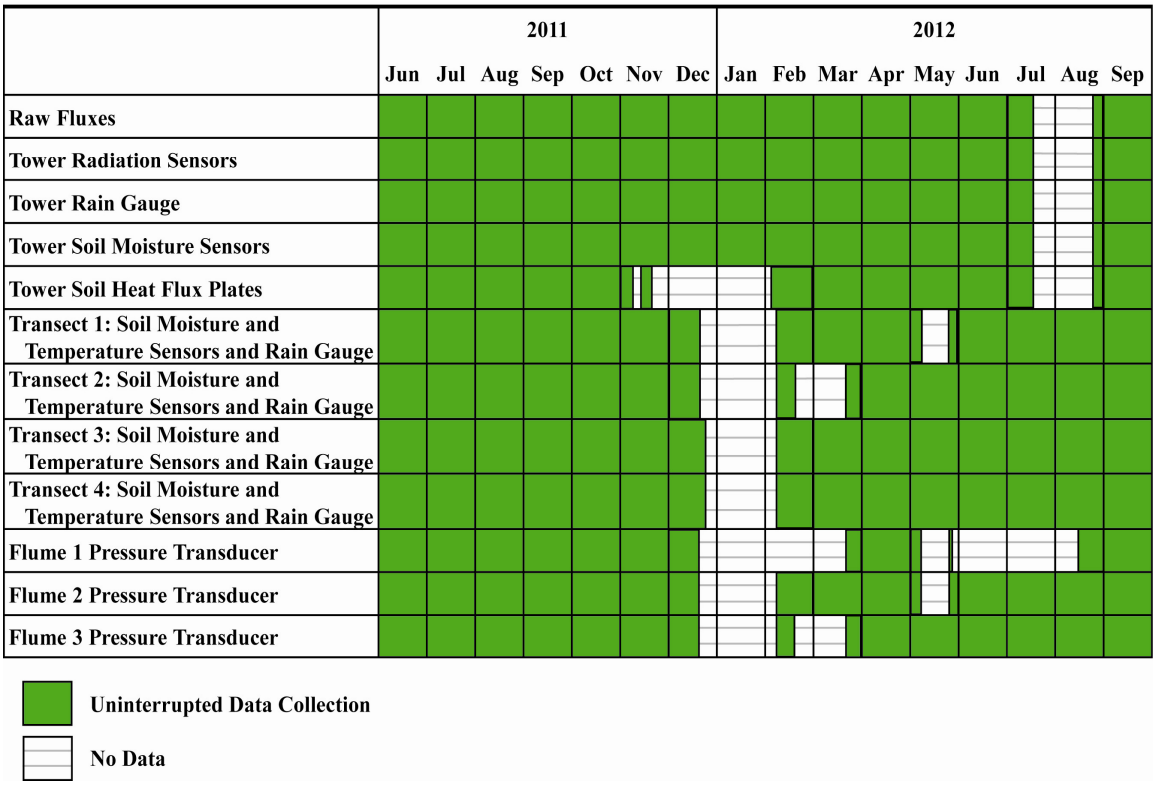

Figure 7: Missing observation periods for all environmental sensors between 6/1/2011 to October 1, 2012. Missing datasets are due to equipment malfunction or theft.

Soil heat flux plates (Hukseflux, HFP01-SC) were placed at a 5 cm depth, overlying soil temperature sensors (Campbell Scientific, TCAV) which were placed at 2 and 4 cm depths. Soil heat flux is calculated by using the two soil temperatures at the two different depths to measure the average soil temperature above the heat flux. Soil moisture at the 5 cm depth is used to help calculate the heat capacity of soil. Once this is determined, the heat flux is calculated at the surface using the heat capacity of soil and the change of temperature over the thermocouple depths.

Missing periods in the datasets are summarized in Figure 7. The missing periods are due to equipment malfunction or stolen equipment.

2.5 Distributed Hydrologic Model

The Triangulated Irregular Network (TIN)-based Real-time Integrated Basin Simulator (tRIBS) is used to study the influence of the mesquite encroachment patterns on the watershed dynamics. tRIBS is a physically based, fully distributed hydrologic model that has been employed for numerous hydrologic studies, for example, the semi-arid Sierra Los Locos basin (Vivoni et al, 2010) in Sonora, Mexico and a semi-arid ponderosa pine hillslope in the Los Alamos National laboratory in New Mexico, USA (Mahmood and Vivoni, 2011). The study basins are partitioned into a TIN and each TIN node is associated with a Voronoi polygon. The TIN is generated from a 1 meter bare earth DEM. To account for spatial heterogeneity of soil and land use, tRIBS assigns a specific soil type or land use type to each Voronoi polygon. The vegetation classification shown in Figure 5 specifies three different vegetation types that are captured within the basin representation. Additionally, three different soil types were used in the basin models to differentiate soil characteristics relative to their vegetation cover. tRIBS is able to parameterize rainfall interception, evapotranspiration, infiltration while accounting for soil moisture, lateral moisture transport, and runoff production and routing. A more in depth description of the model physics can be found in Ivanov et al. (2004a, b) and Vivoni et al. (2007, 2010).

The two study periods were chosen to represent the North American Monsoon (NAM) season. The first study period includes June 1, 2011 through September 30, 2011 and will be referred to as the summer 2011 study or simulation period. The second study period is June 1, 2012 through September 30, 2012 and will be referred to as the summer

2012 study or simulation period. By starting the study at the beginning of June, it is ensured that the start of the monsoon season is captured. The study periods end on September 30 as the NAM season has culminated. Model forcing consisted of half-hour precipitation from each of the 6 rain gauges, and the following variables from the eddy covariance tower: air temperature, relative humidity, wind speed, barometric pressure and incoming solar radiation. For the missing data periods, an alternate dataset was obtained from a nearby eddy covariance tower, described in Scott et al. (2009). Since the forcing parameters had a temporal resolution of 30 minutes, simulations were run at a 30 minute resolution. Initial ground water depth was critical for the two different simulation periods. The basin was relatively dry prior to the summer 2011 period while there was greater soil moisture prior to the summer 2012 period. The initial water tables for each simulation period were specified to reflect this initial moisture difference. To further account for the initial soil moisture difference, the soil parameter of residual soil moisture was different for the two simulation years. The parameter value used for each simulation is specified in Appendix G.1. The assumed soil depth for both basins is 1 meter.

In this study, a point scale model was developed at the eddy covariance tower location to analyze the hydrologic dynamics and verify the soundness of the model performance as compared to observations at the tower. A single Voronoi polygon was centered at the tower with a grass vegetation and soil classification. The summer 2011 simulation period was used to calibrate certain soil and vegetation parameters related to the grass cover, with the summer 2012 simulation period serving as a validation period. The full set of soil and vegetation parameters are summarized in Appendix G.1.

Simulated results for each simulation period were compared against field observations and three different error metrics were calculated: bias (B), mean absolute error (MAE), and correlation coefficient (CC). The following equations calculated each of these error metrics:

$$B = \bar{O} / \bar{S} \qquad \text{Equation 7}$$

$$MAE = \frac{1}{N} \sum_{i=1}^{N} |O_i - S_i| \qquad \text{Equation 8}$$

$$CC = \frac{\sum_{i=1}^{N} (O_i - \bar{O})(S_i - \bar{S})}{\left[\sum_{i=1}^{N} (O_i - \bar{O})^2\right]^{0.5} \left[\sum_{i=1}^{N} (S_i - \bar{S})^2\right]^{0.5}} \qquad \text{Equation 9}$$

where S is the simulation, O is the observation, and N is the number of time steps. An analysis of the bias gives an indication how the temporal mean of the observations compare to the temporal mean of the simulations. The mean absolute error gives the absolute differences between the observations and simulations. The correlation coefficient describes the linear dependence between the observations and simulations.

Two basin models were also developed at each study watershed to analyze the hydrologic dynamics, such as soil moisture and evapotranspiration, over the spatial representation of each basin. Watershed 8 is represented with 10,548 voronoi polygons, while watershed 7 is represented with 10,309 voronoi polygons, which were determined from the 1 meter DEM. Further calibration was necessary as the basin models consist of three vegetation and soil types and the point scale model only consists of one. Again, summer 2011 served as the calibration period while summer 2012 validated the calibrated parameters. The full set of soil and vegetation parameters for each model is summarized

in Appendix G.2. By comparing the two basin models, a better understanding of the impact of mesquite trees, which are well represented with the unique Voronoi polygons, on hydrological processes will be explored.

RESULTS AND DISCUSSION

3.1 Basin Temporal Dynamics

The spatial and temporal variability of hydrologic and energy states and fluxes are important in characterizing a semiarid system. The seasonal variability of said fluxes is shown for specific seasonal periods. The different seasons are classified as summer (July 1 to September 30), fall (October 1 to December 31), winter (January 1 to March 31), and spring (April 1 to June 30). Five seasons in total were evaluated during the study period and each is shown in the following way: summer 2011 in Figure 8, fall 2011 in Figure 9, winter 2012 in Figure 10, spring 2012 in Figure 11, and summer 2012 in Figure 12. Any missing data gaps are due to battery malfunction, power equipment theft, or some other equipment failure. The basin-averaged soil moisture and temperature presented is an average of the 21 sensors at each depth across the basin. The fluxes are calculated at the eddy covariance tower site, just north of watershed 8. The runoff measurement presented is the outlet at watershed 8. Total annual rainfall for 2011 was 382.02 mm and for 2012 was 337.31 mm. Both totals are below the reported annual average rainfall of 458 mm from Polyakov et al. (2010). In 2011, 257.43 mm of rain fell during the summer, or 67.4% of the annual rainfall. The proportion was even greater in 2012 when 251.46 mm fell, accounting for 74.5% of the annual rainfall. Polyakov et al. (2010) reported that average rainfall between the months of July and September is 247.9 mm. The two study years appear to be relatively dry years, yet received above average monsoon rains.

The soil moisture sensors responded readily with a storm event. The 5 cm depth

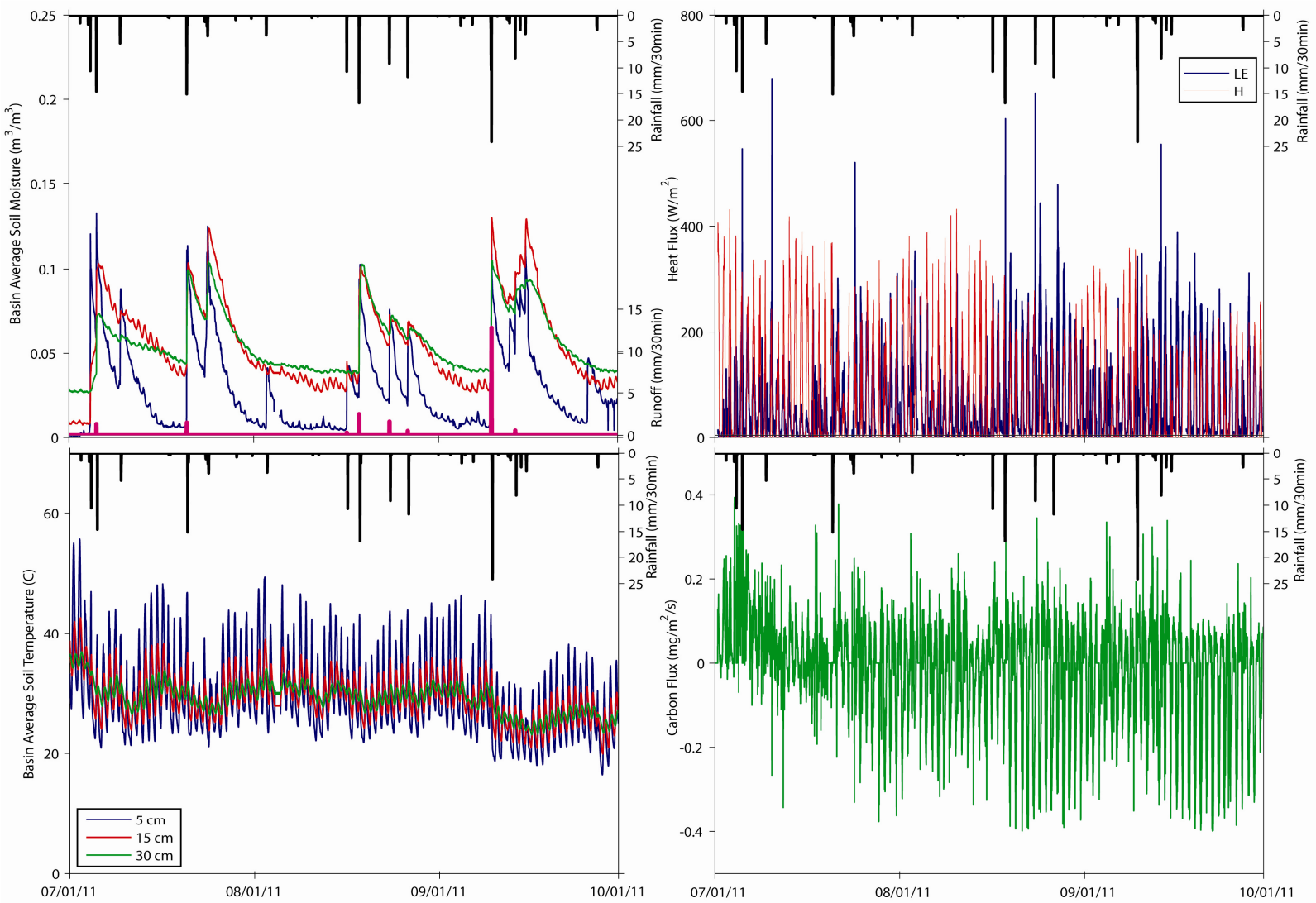

Figure 8: Summer 2011 (a) basin averaged soil moisture (m^3/m^3) and (b) soil temperature (^oC) at 5 cm, 15 cm, and 30 cm, (c) latent heat (LE) and sensible heat (H) flux (W/m^2) and (d) carbon flux ($mg/m^2/s$).

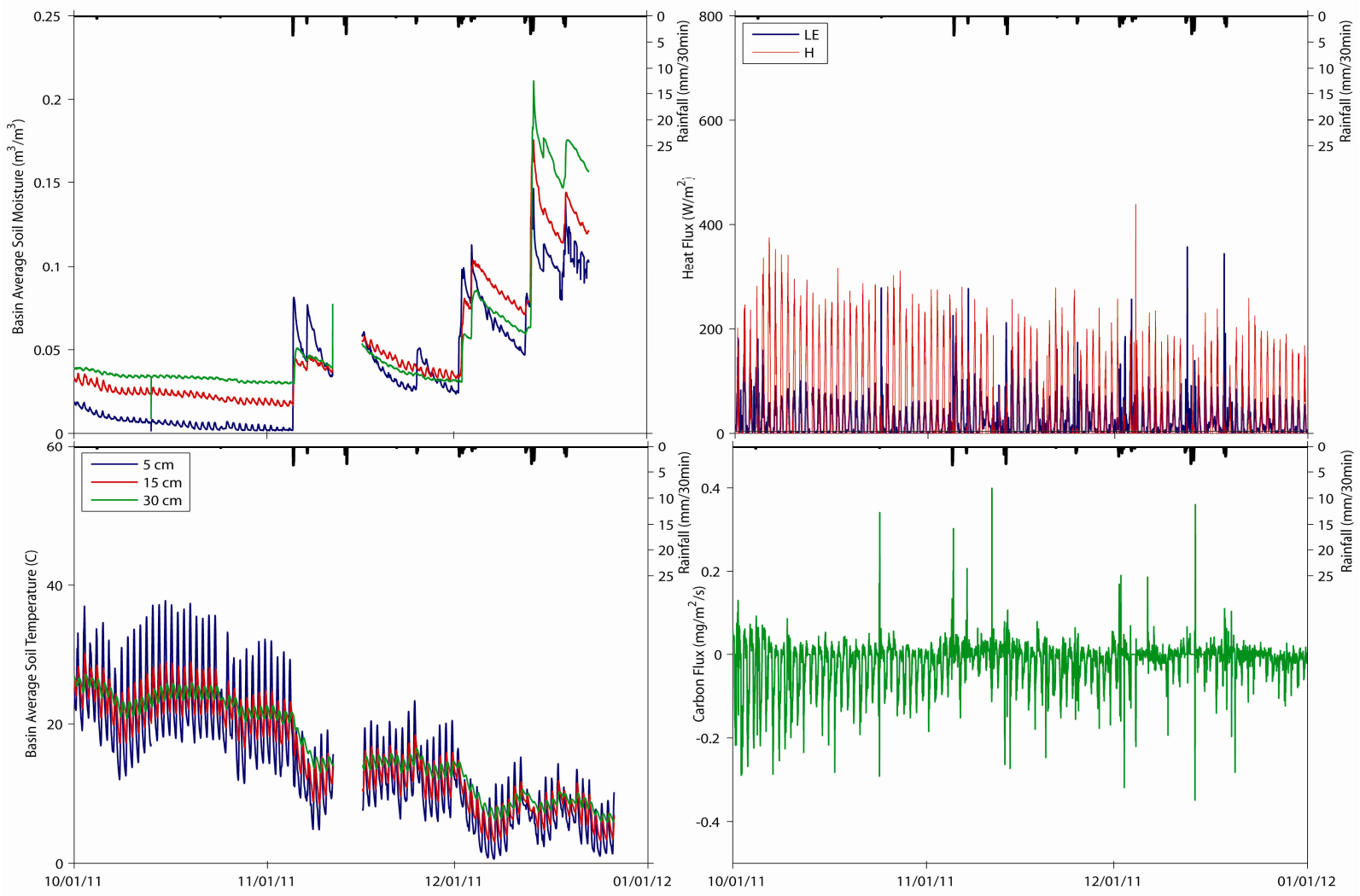

Figure 9: Fall 2011 (a) basin averaged soil moisture (m^3/m^3) and (b) soil temperature (^oC) at 5 cm, 15 cm, and 30 cm, (c) latent heat (LE) and sensible heat (H) flux (W/m^2) and (d) carbon flux ($mg/m^2/s$).

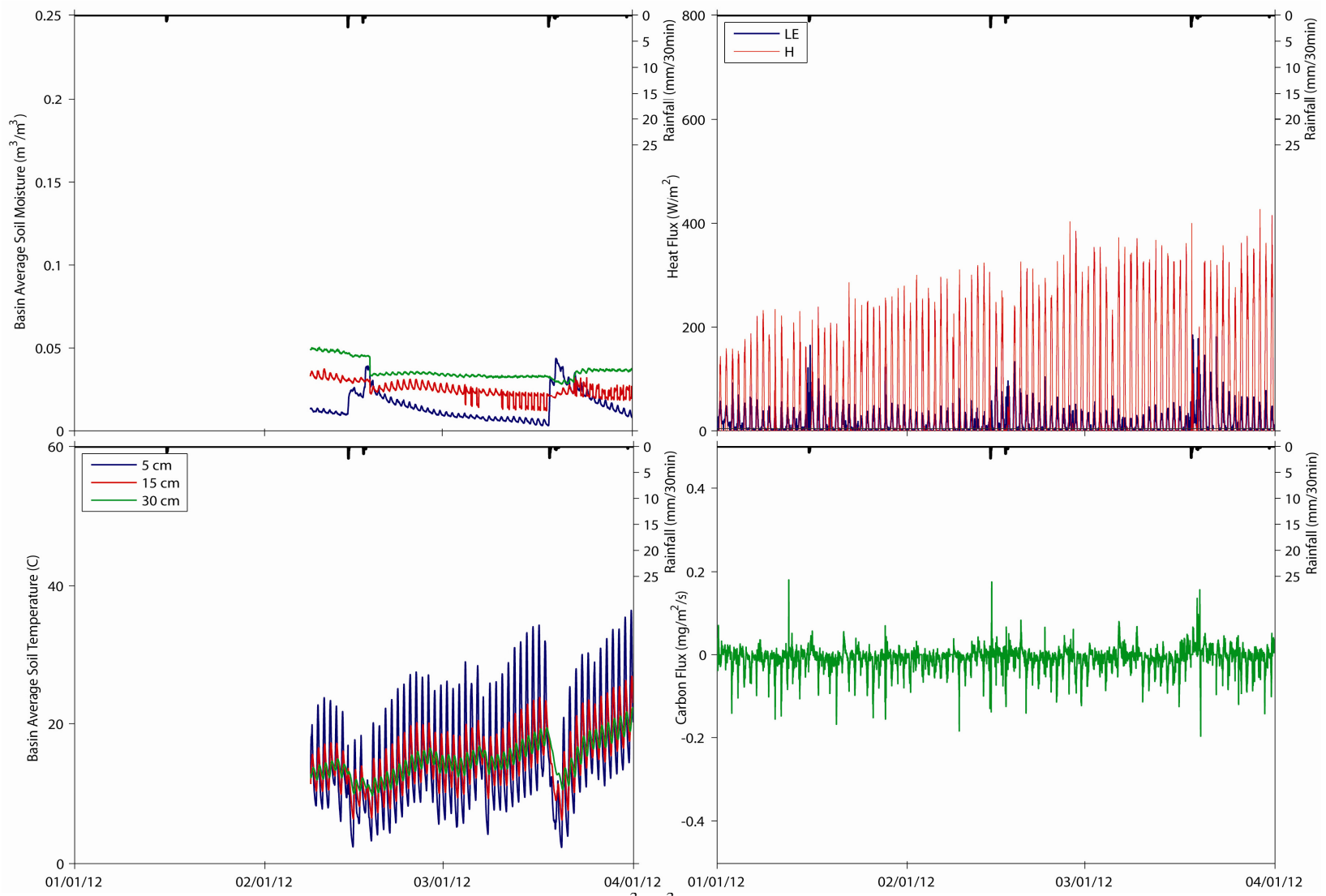

Figure 10: Winter 2012 (a) basin averaged soil moisture (m^3/m^3) and (b) soil temperature (^oC) at 5 cm, 15 cm, and 30 cm, (c) latent heat (LE) and sensible heat (H) flux (W/m^2) and (d) carbon flux ($mg/m^2/s$).

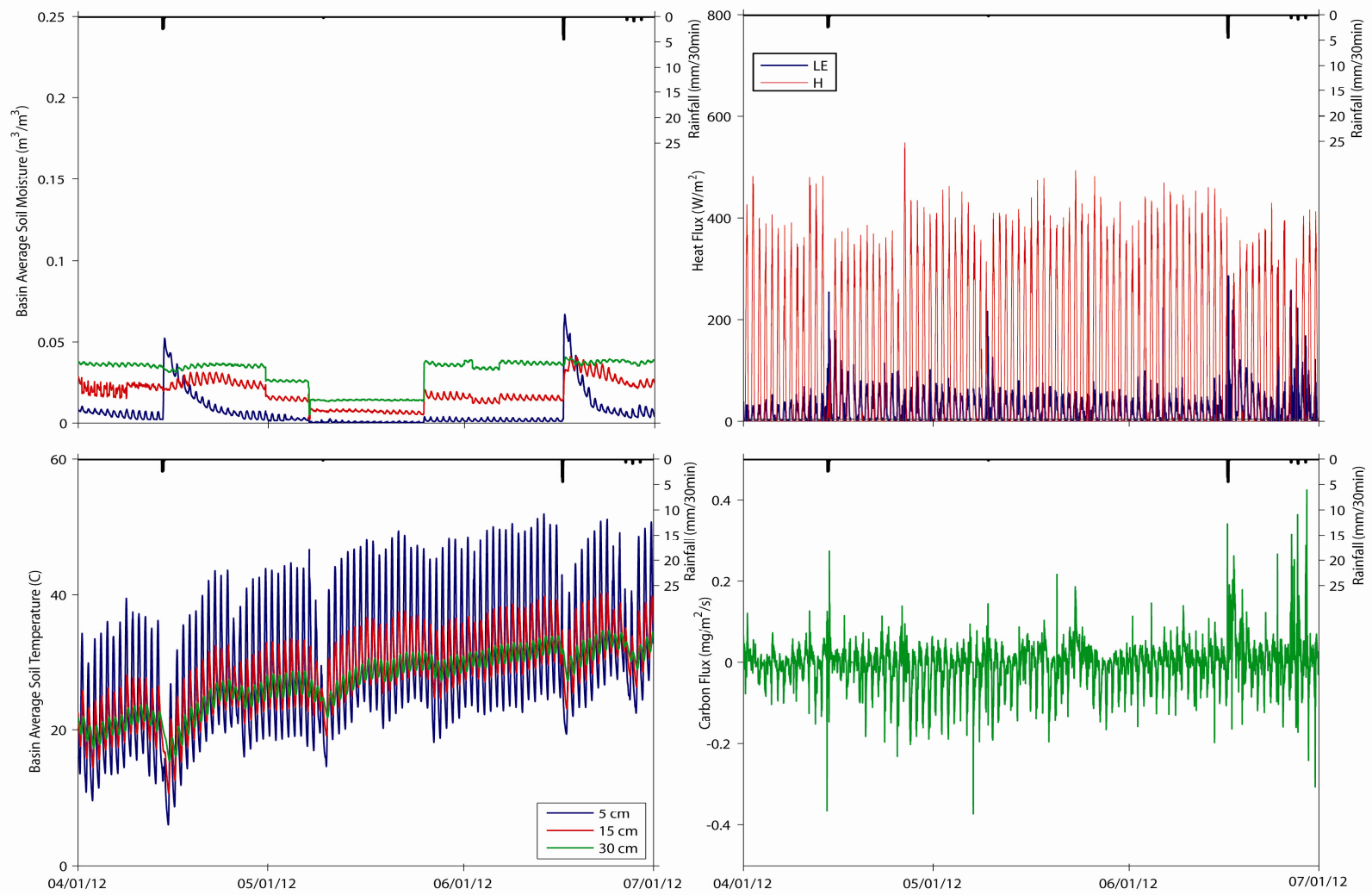

Figure 11: Spring 2012 (a) basin averaged soil moisture (m^3/m^3) and (b) soil temperature (^oC) at 5 cm, 15 cm, and 30 cm, (c) latent heat (LE) and sensible heat (H) flux (W/m^2) and (d) carbon flux ($mg/m^2/s$).

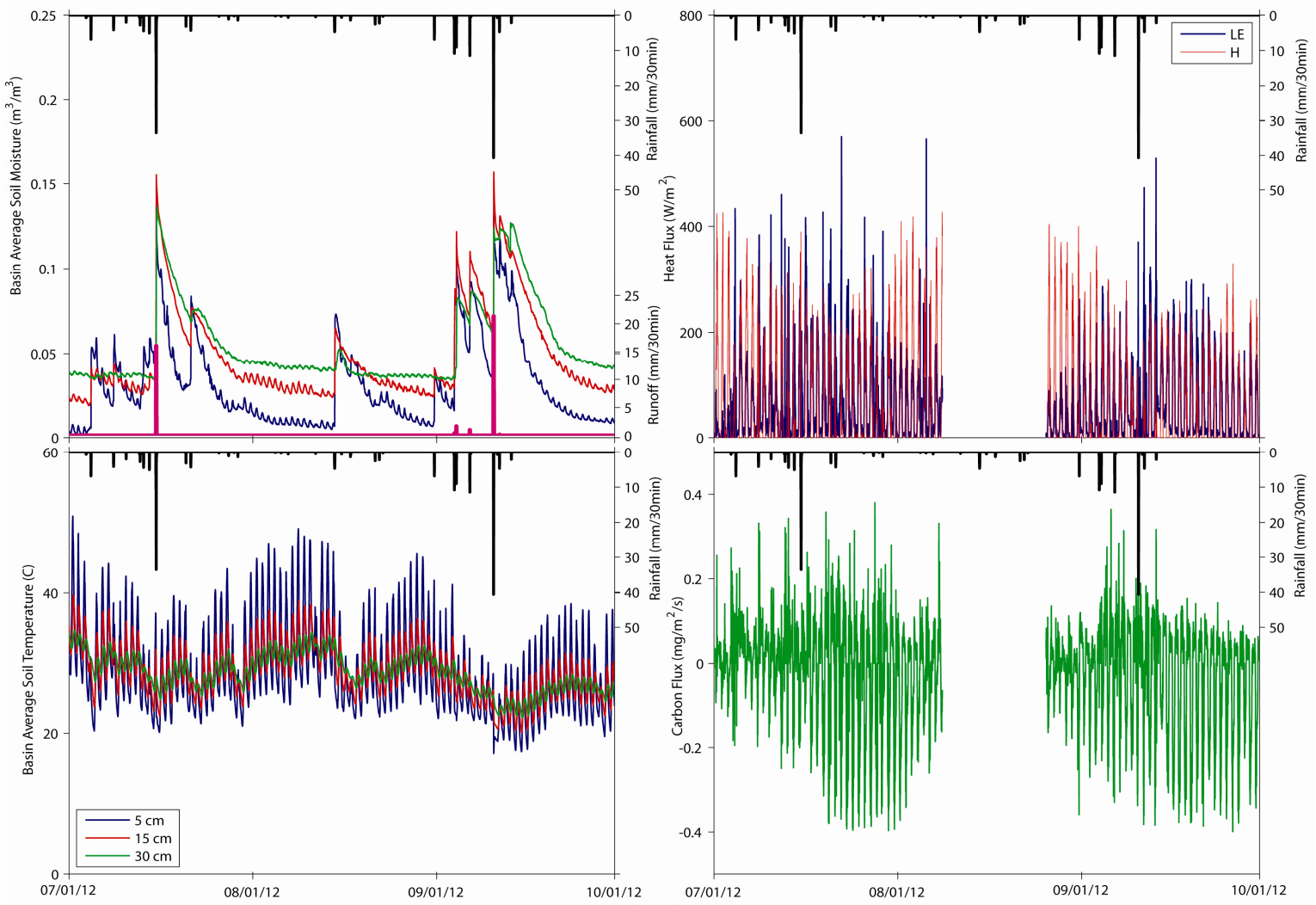

Figure 12: Summer 2012 (a) basin averaged soil moisture (m^3/m^3) and (b) soil temperature (^oC) at 5 cm, 15 cm, and 30 cm, (c) latent heat (LE) and sensible heat (H) flux (W/m^2) and (d) carbon flux ($mg/m^2/s$).

was most sensitive and soil moisture increased with minimum input of precipitation. The 15 cm depth had fewer, fairly high peaks in the summer. The 30 cm depth had the smallest peaks, but took the longest to dry down after an event. The 5 cm depth had the steepest recession limbs, due to the high evapotranspiration rates. High evapotranspiration rates most likely contributed to the recession of soil moisture at 15 cm depth as well. Soil moisture steadily decreased until the winter precipitation season began, as shown in Figures 8 and 9. The 5 cm depth had the largest initial peak, but as the season progressed, the 30 cm depth experienced the largest soil moisture peaks during the study period, indicating that recharge could be occurring. The winter precipitation events were smaller, however they characteristically are longer and allow for more infiltration to occur (Cable, 1980; Scott et al., 2000). After the winter precipitation, the soil moisture generally decreased until the next NAM onset. Runoff events only occurred during the summer periods. Only 1 large runoff event (>5 mm) occurred during summer 2011 and two occurred during summer 2012. Soil temperature was most variable at the 5 cm depth and least variable at the 30 cm depth. During a precipitation event, the temperatures decreased at all depths. Soil temperature was lowest during the winter and highest during the summer.

Energy fluxes exhibit strong variability across the five seasons. Throughout the fall, winter, and spring, sensible heat flux is much higher than latent heat flux. Sensible heat flux peaks during the spring time, at approximately 500 W/m^2. This is concurrent with rising soil temperature. Latent heat flux is dominant after precipitation events during the NAM season, or summer periods. Peaks reaching 600 W/m^2 were observed, concurrent with high soil moisture values at shallow depths. Otherwise, latent heat flux rarely rose above 200 W/m^2. Carbon flux was most variable during the summer seasons. This is due to the NAM onset and the vegetation

greening of annual herbs and perennial grass beneath the mesquite canopies. This green-up leads to increased evapotranspiration and daytime carbon assimilation, however there is also an increase in respiration at night, which leads to a decrease in net daily carbon uptake relative to the system pre-monsoon (Scott et al., 2004). The various hydrologic and energy states and fluxes provide a solid foundation to understanding the hydrological cycle at the study basins. Most of the hydrologic and energy states and flux variability occurs during the summer seasons, which is consistent with the onset of the NAM. Given that the majority of the rainfall and runoff occurs during the summer seasons, the remaining analysis is focused on the NAM season.

3.2 Soil Moisture Network Temporal Dynamics

The unique set up of the soil moisture and temperature sensor network across watershed 8 allows for a detailed analysis of temporal variability in soil moisture and temperature during the monsoon season. Upon installation, each sensor was classified by the vegetation type that overlaid it, specifically as grass, mesquite, or bare soil. After defining the watershed 8 boundary, it was determined that fifteen sensors actually lied within the delineated basin. Of these fifteen sensors, seven are measuring bare areas, five are measuring under mesquite trees, and three are measuring herbaceous vegetation. The average values for soil moisture and temperature were computed for the three different vegetation classes.

Figure 13 shows the soil moisture and temperature averaged across the bare sensors, the grass sensors, and the mesquite sensors for June 1, 2011 to September 30, 2011. The data is analyzed for this time period because it was determined to capture the basin dynamics prior to and at the onset of the North American monsoon through the end of the NAM. Figure 14 shows

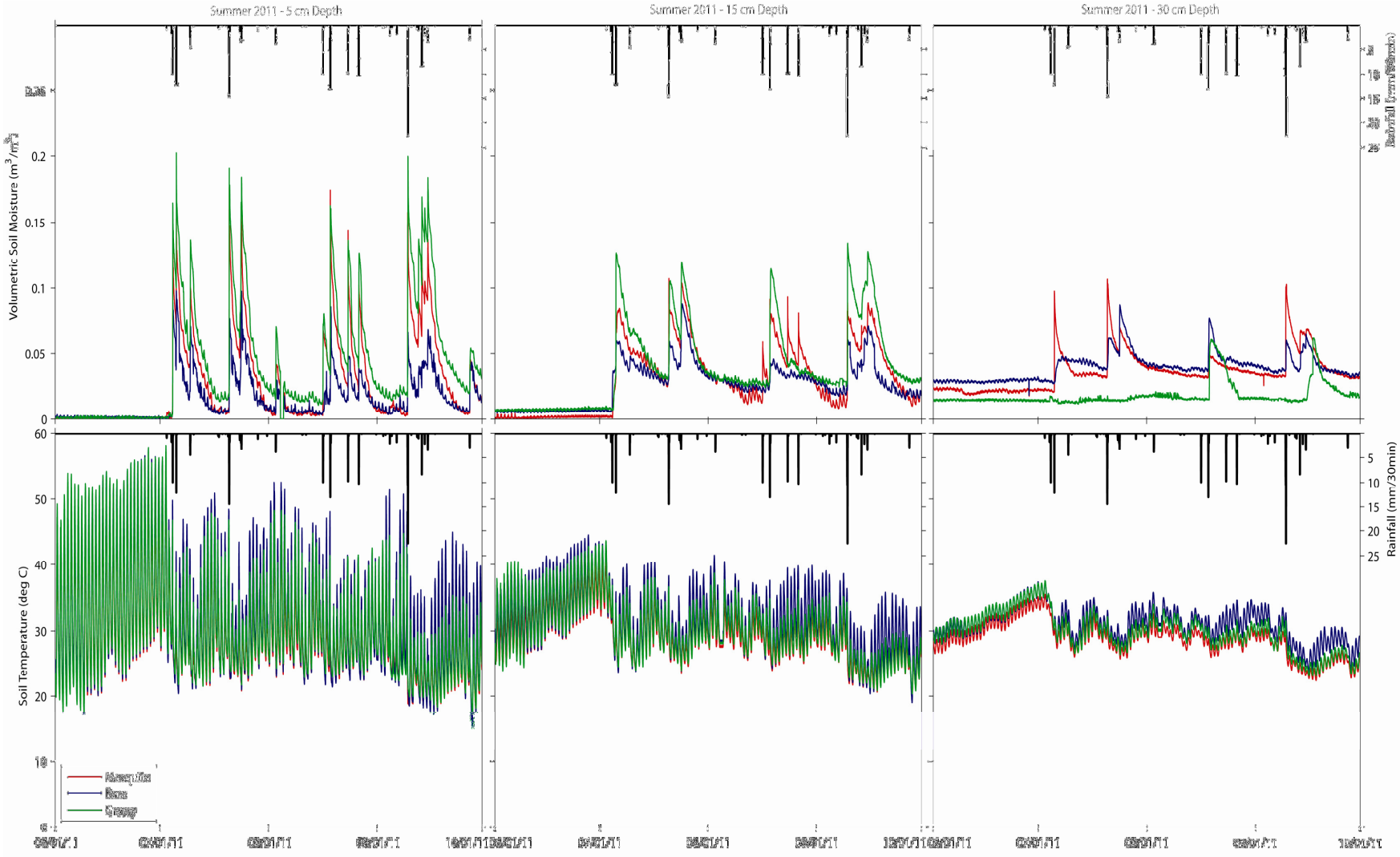

Figure 13: Summer 2011 vegetation specific soil moisture at three depths (a) 5 cm (b) 15 cm and (c) 30 cm and soil temperature at three depths (d) 5 cm (e) 15 cm and (f) 30 cm.

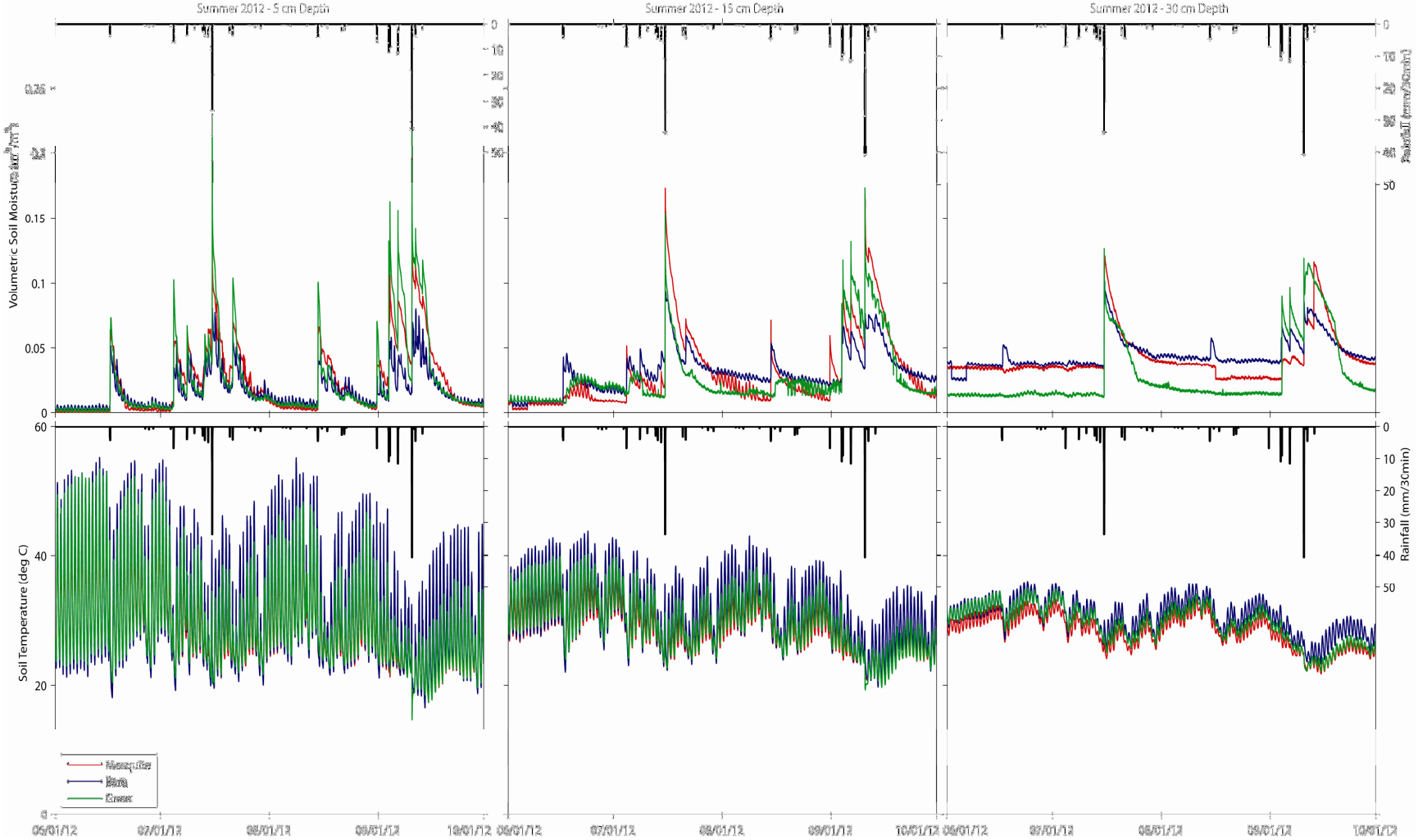

Figure 14: Summer 2012 vegetation specific soil moisture at three depths (a) 5 cm (b) 15 cm and (c) 30 cm and soil temperature at three depths (d) 5 cm (e) 15 cm and (f) 30 cm.

the soil moisture and temperature dynamics for June 1, 2012 to September 30, 2012. At the 5 cm depth for both summer 2011 and summer 2012, the grass locations have the highest soil moisture, the bare locations have the lowest, and the mesquite locations are intermediate. Bare locations would be expected to have the lowest soil moisture because of the high evaporation. Precipitation that falls onto a bare area presumably hits bare soil. It is then more likely to evaporate from the bare soil since there is more exposure to radiation and no vegetation is present to either intercept the precipitation or uptake the soil water. The precipitation may also be more likely to runoff as bare soil areas may have lower infiltration capacities compared to vegetated areas. Mesquite locations may be expected to have less soil moisture values than grass locations due to plant interception. The mesquite canopies would be more prone to capturing precipitation as it fell and then the water would evaporate. Grass areas would be expected to receive a greater precipitation input compared to the mesquite sites. Grass areas would also be able to partially shade the ground, allowing more water to infiltrate. It is hypothesized then that bare areas will have the highest temperatures, followed by grass sites, and finally mesquite sites. Bare areas have the highest maximum surface soil temperatures. Grass areas actually have the next highest maximum temperatures, with mesquite areas having the lowest temperature, which can be explained by shading that the mesquite canopies provide. The bare areas generally have the lowest minimum temperature, followed by grasses and mesquite respectively. Interestingly, before the onset of the NAM season, the grass sites had higher maximum temperatures than the bare areas. This is probably due to the grasses being dormant from no precipitation input and not having

yet greened, so these sites are acting like bare sites. Bare sites may have a higher albedo compared to the senescent grass, explaining the temperature differences. During precipitation events, soil moisture increased for all vegetation areas and soil temperature decreased. At the 15 cm depth, grass sites generally had the highest soil moisture, followed by mesquite sites and then bare areas. Two events in August in 2011 lead to sharp mesquite soil moisture increases at the 15 cm depth that were not present at the grass sites, shown in Figure 13b. These increases were only present at the grass sites at the 5 cm depth. This could be explained by certain grasses with roots that fall between 5 and 15 cm being capable to uptake the infiltrating water. The first large event in July of 2012 lead to a greater mesquite site spike at the 15 cm depth compared to grasses. Since this was the first significant water input of the NAM season, the grasses were most likely still greening, and were uptaking the extra water. The 15 cm soil temperatures are as expected, with bare soil experiencing the highest temperatures and the most variability. Overall, the variability for all of the vegetation types is much less as compared to the 5 cm depth. The variability is even smaller at the 30 cm depth. At the 30 cm depth, the soil moisture patterns differ from the shallower depths. Mesquite sites have the highest soil moisture, especially in 2011. In the 2011 period, grasses actually have the lowest soil moistures, only spiking above the bare soil moisture during one precipitation event. This may be explained by the rooting depth of the grasses, which is unlikely to be deeper than 30 cm. Most of the water in these areas is then subject to uptake by the grass roots. While mesquite trees also have shallow roots, their depths can span a larger length, as they have a taproot which can draw groundwater. Another possible explanation for the

increased soil moisture at the mesquite sites is due to their ability to spread roots laterally and utilize more soil for uptake, as found in O'Donnell and Caylor (2012). In the 2012 period, grasses do actually have a greater spike with precipitation events, however at 30 cm depths they have the lowest soil moisture during inter-storm periods. The spikes may be explained by the relatively few precipitation events during the NAM season, especially between mid-July and September. Some of the grasses may have become dormant with the lack of water causing these sites to act more similarly to bare soil sites when the late season precipitation events occurred, except with slightly lower temperatures.

Evaluating the different soil moisture and temperature temporal dynamics across the distinct vegetation types is important to understanding how the grasses, mesquite, and bare areas coexist. In addition, the dynamics are able to provide insight into how the precipitation input could be vertically distributed in the system. Higher soil moisture values may indicate that more groundwater recharge can occur at those vegetation sites. Lower soil moisture may imply that more root uptake is occurring, which could lead to more transpiration. Lower soil moisture may also signify that more runoff is being generated at those areas or more evaporation is occurring, as a function of the water balance.

3.3 Rainfall and Runoff Watershed Analysis

Vegetation cover is the essential difference between the two study basins. Watershed 7 has been treated for mesquite, and while mesquite trees are still found in the

basin, there is a greater percentage of grass and bare areas, as quantified with the vegetation classification process. As described previously, the vegetation cover is vital in trying to understand how precipitation will be transformed into soil moisture, evapotranspiration, and runoff in the basin. More grass and bare areas can lead to more runoff generation or more evaporation, while the presence of mesquite trees may redistribute the water via root systems. To better understand the differences between the two study basins, rainfall and runoff data was analyzed using the rain gauge and outlet flumes established in 1976 at both basins and managed by the USDA ARS Southwest Watershed Research Center.

3.3.1 Decadal Analysis

Historical runoff and rainfall data is available for both watersheds from 1976 to present. The total number of runoff events was determined for each basin over the period 2000 to 2012. The number of runoff events for a specific year in watershed 7 was then plotted against the number of runoff events for a specific year in watershed 8, as shown in Figure 15. For clarity, a 1:1 line is included on the graph as well as a linear regression. Ten points fall below the 1:1 line, while only two are above it, indicating that generally more runoff events occur in watershed 7 as compared to watershed 8. Both of the years in this study had more runoff events generated on watershed 7. The slope of the regression line, 0.5904, serves as an indicator that the points generally lay below the 1:1 line. Calculating the slope gives an indicator that allows comparisons over multiple decades, as will be explained next. Figure 16 plots the total amount of runoff (mm), generated from watershed 7 and watershed 8, normalized by the area of each watershed.

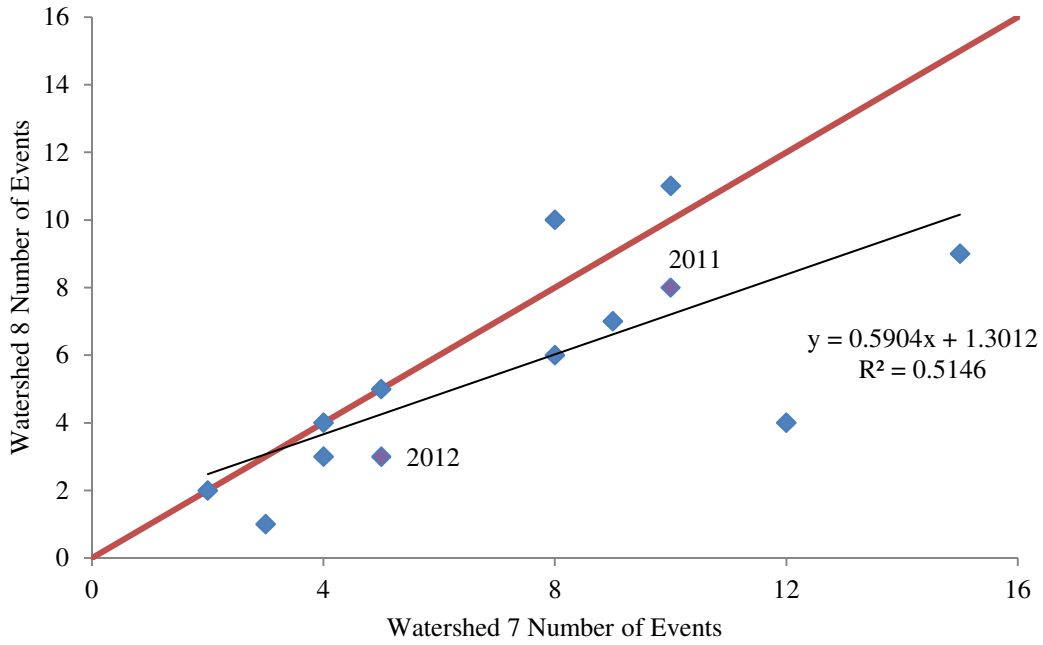

Figure 15: Number of runoff events per year from 2000 to 2012.

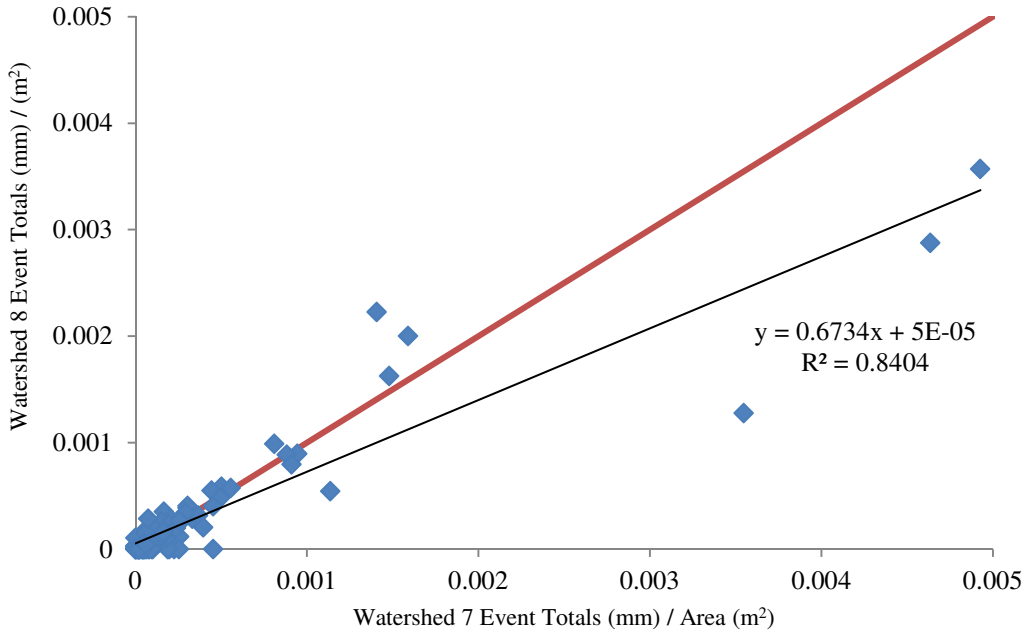

Figure 16: All events at both watersheds from 2000 to 2012.

Again, a 1:1 line was included on the graph and generally more points lie beneath the line than above it. The slope of the regression line, 0.6734, also indicates that watershed 7 tends to produce more runoff per area than watershed 8. For the past decade, runoff data has shown that watershed 7, which had undergone mesquite removal treatment, generally produces more runoff events and generates more runoff per unit area. To better understand how the watershed has been transformed since the treatment in 1976, the number of runoff events and total amount of runoff generated at each watershed was calculated and compared. The data was then lumped into a decade by decade comparison. Similar to the figures described, a linear regression line was fit, with the general understanding that slopes greater than one signify watershed 8 generates more runoff or more runoff events, while slopes less than one signify watershed 7 generates more runoff or more runoff events. The results are shown in Figure 17.

In the 1976 to 1979 period, more runoff events occurred at watershed 8 and more runoff was generated at watershed 8. The 1980 to 1989 period had more events at watershed 8, yet more runoff being generated at watershed 7. The 1990 to 1999 period had more runoff events at watershed 7, yet slightly more runoff totals being generated at watershed 8. Finally, from 2000 to 2012, more total runoff and more runoff events were generated at watershed 7. As a result, the number of runoff events increased over time from watershed 8 to watershed 7, while the runoff totals were more variable.

The patterns may indicate runoff generation relationships between the two watersheds based on vegetation cover. Initially, watershed 8 with mesquite trees produced more runoff. When the mesquite trees were killed in watershed 7, the litter

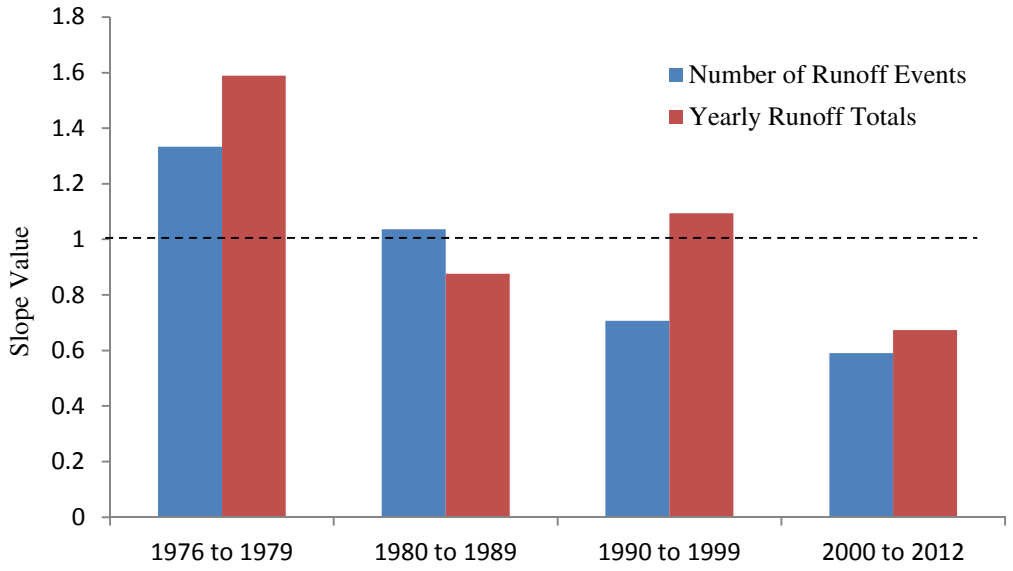

Figure 17: Watershed 7 vs. watershed 8 decadal comparison of yearly runoff total volumes and number of runoff events.

remained onsite and may have been blocking runoff and causing more infiltration. As watershed 7 began to re-establish natural vegetation, specifically grasses, it began producing more runoff. The dominant vegetation type on watershed 7 is grass while the dominant vegetation type on watershed 8 is mesquite. At present time, watershed 7 produces more runoff volume and more runoff events. This may be explained by the vegetation characteristics of grasses versus mesquite trees. Mesquite trees have a greater water holding capacity than grasses. For larger precipitation events, mesquite trees can keep making use of infiltrated water while grass areas would be fully saturated. A more likely difference is that the mesquite canopies prevent more water from reaching the surface, and so less runoff could be produced. Mesquite canopies are also capable of creating a microclimate under the canopy, allowing for more infiltration.

Based on the historical data analysis, mesquite removal treatment alters runoff generation patterns. Shifting landscapes are characteristic of these study basins and so a better understanding of how the vegetation, mesquite trees and grass, specifically affect runoff is critical for describing the hydrological effects of mesquite encroachment.

3.3.2 Study Period Event Analysis

To aid in gaining a more thorough understanding of the runoff events occurring at each basin, each runoff event was analyzed during the study period. Runoff ratios were calculated to help describe how much precipitation was generated into runoff, and what precipitation events led to higher or lower ratios. Tables 4 and 5 describe the runoff event characteristics of watershed 7 and 8, respectively, in 2011. Tables 6 and 7 describe the runoff event characteristics of watershed 7 and 8, respectively, in 2012. As the tables show and previously discussed, watershed 7 had more runoff events for both years and produced more total runoff. Higher runoff ratios were calculated for the larger events (generally volume > 150 m^3). The average runoff ratio for watershed 7 in 2011 is 0.11 and in 2012 is 0.18. The average runoff ratio for watershed 8 in 2011 is 0.12 and in 2012 is 0.25. Both years saw that watershed 8 average a higher runoff ratio, which is contrary to previous analysis. However, it appears that for larger events, watershed 8 does indeed produce more runoff, while watershed 7 typically produces more runoff for smaller events. Also, runoff events that occur on watershed 7 and not 8 are usually very small. As a result, there appears to be a threshold precipitation value that could determine whether watershed 7 or watershed 8 would produce more runoff. To further explore the runoff ratio comparisons, Figure 18 shows the runoff ratios for watershed 7

Table 4: Watershed 7 runoff event characteristics for summer 2011.

Storm Number	Date	Start Time	Max Rainfall Rate (mm/hr)	Duration (min)	Volume (m^3)	Peak Flow (mm/hr)	Time to Peak (min)	Runoff Ratio
1	7.5.11	14:39	91.44	38.25	15.68	8.816	10.25	0.10
2	7.20.11	17:37	83.82	48.5	24.64	7.02	30.25	0.08
4	8.16.11	13:34	68.58	26.5	3.38	2.058	12.25	0.03
5	8.18.11	14:58	106.68	75.5	33.10	12.657	12.25	0.11
6	8.23.11	17:19	106.68	40.25	21.75	11.634	13.25	0.13
7	8.26.11	19:04	76.2	142.5	6.83	4.109	18.25	0.05
8	9.9.11	17:57	137.16	216.25	246.47	49.445	41.25	0.41
9	9.13.11	19:48	106.68	20.5	7.15	5.456	6.25	0.07

Table 5: Watershed 8 runoff event characteristics for summer 2011.

Date	Start Time	Max Rainfall Rate (mm/hr)	Duration (min)	Volume (m^3)	Peak Flow (mm/hr)	Time to Peak (min)	Runoff Ratio
7.5.11	14:39	91.44	42.5	17.96	10.239	14.25	0.12
7.20.11	17:42	83.82	57.5	27.15	7.394	28.25	0.09
7.24.11	5:56	38.1	101.5	8.84	2.168	8.25	0.10
8.16.11	13:38	68.58	30.5	6.46	4.327	10.25	0.05
8.18.11	15:02	106.68	84.5	29.65	11.223	8.25	0.10
8.23.11	17:23	106.68	41.5	19.58	11.223	9.25	0.12
8.26.11	19:09	76.2	65.5	5.35	3.139	13.25	0.04
9.9.11	17:59	137.16	200.5	182.64	35.843	39.25	0.32
9.13.11	19:40	106.68	42.5	10.59	8.326	14.25	0.11
9.15.11	12:53	38.1	47.5	4.70	1.757	4.25	0.06

Table 6: Watershed 7 runoff event characteristics for summer 2012.

Storm Number	Date	Start Time	Max Rainfall Rate (mm/hr)	Duration (min)	Volume (m^3)	Peak Flow (mm/hr)	Time to Peak (min)	Runoff Ratio
1	7.13.12	9:19	38.10	108.25	10.94	28.591	106.5	0.23
2	7.15.12	15:42	320.04	138.75	161.58	74.428	70.0	0.27
3	8.31.12	14:05	53.34	26.25	2.69	2.168	9.75	0.03
4	9.3.12	23:00	76.20	63.25	7.08	2.626	6.25	0.05
5	9.4.12	7:11	68.58	35.25	18.72	12.254	8.5	0.19
6	9.6.12	13:34	68.58	44.00	12.60	7.394	11.5	0.10
7	9.10.12	13:25	152.40	124.50	323.38	52.077	16.75	0.48
8	9.11.12	13:53	45.72	39.50	3.79	2.168	4.5	0.07

Table 7: Watershed 8 runoff event characteristics for summer 2012.

Storm Number	Date	Start Time	Max Rainfall Rate (mm/hr)	Duration (min)	Volume (m^3)	Peak Flow (mm/hr)	Time to Peak (min)	Runoff Ratio
2	7.15.12	15:47	320.04	133.25	274.10	122.619	67.25	0.43
4	9.3.12	23:04	76.20	43.50	5.00	2.058	9.25	0.03
5	9.4.12	7:12	68.58	27.50	19.30	12.657	9.25	0.19
6	9.6.12	13:41	68.58	26.50	11.18	7.020	5.25	0.09
7	9.10.12	13:27	152.40	134.25	520.75	72.561	16.25	0.74
8	9.11.12	13:55	45.72	20.50	2.25	1.668	4.25	0.04

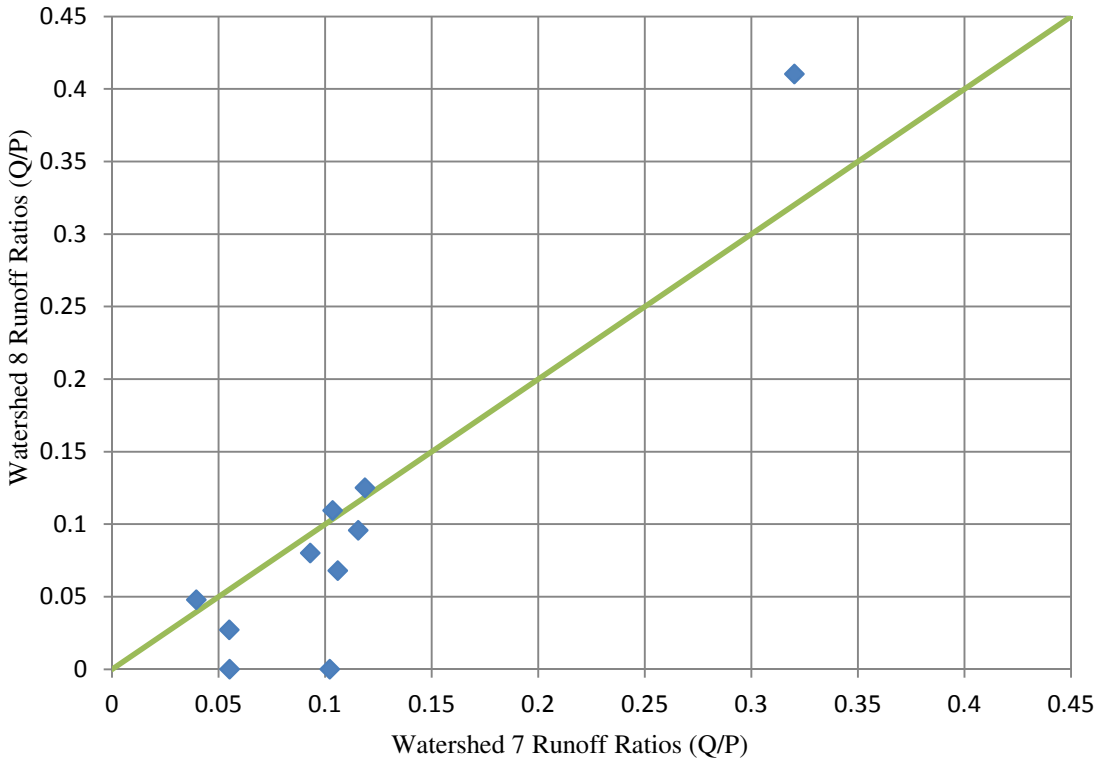

Figure 18: Runoff ratio comparison between watersheds 7 and 8 for summer 2011.

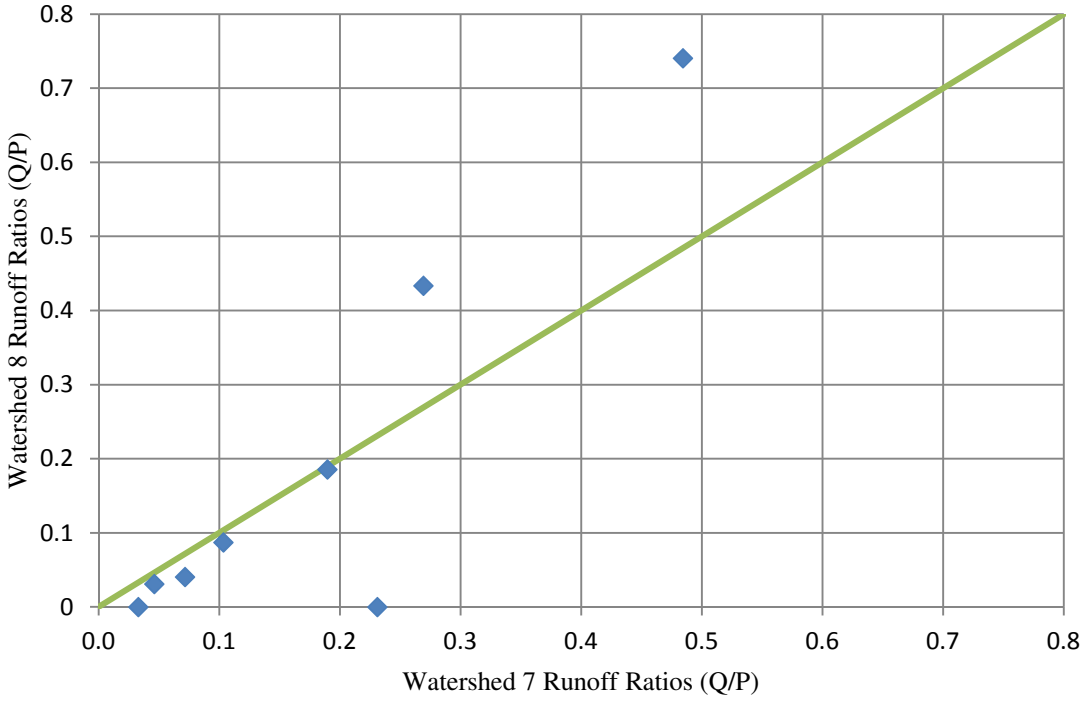

Figure 19: Runoff ratio comparison between watersheds 7 and 8 for summer 2012.

versus watershed 8 for 2011 and Figure 19 shows the runoff ratios for watershed 7 versus watershed 8 for 2012. Both figures include a 1:1 line to help visualize which watershed has higher ratios.

As expected from the table data, the smaller runoff events generally have higher runoff ratios at watershed 7. The unique large events, which occurred once in 2011 and twice in 2012, give a much higher runoff ratio at watershed 8 compared to watershed 7. These large events with high amounts of precipitation cause more runoff generation at watershed 8. These events were characteristic of NAM storms, large amounts of precipitation falling at a very high intensity. Therefore, the canopy storage of the mesquite trees may have been negligible if the rainfall intensity was so high that the drops fell through the canopies and reached the ground. In addition, the very high intensities, shown in the above tables, will typically exceed the soil infiltration capacity regardless of the vegetation cover, resulting in runoff. However the exact vegetation mechanisms playing a role in generating runoff are not well understood.

Another metric to evaluate the runoff characteristics was time to peak discharge for each measured hydrograph. Figures 20 and 21 compare the time to peak runoff at watershed 7 versus watershed 8 for 2011 and 2012, respectively.

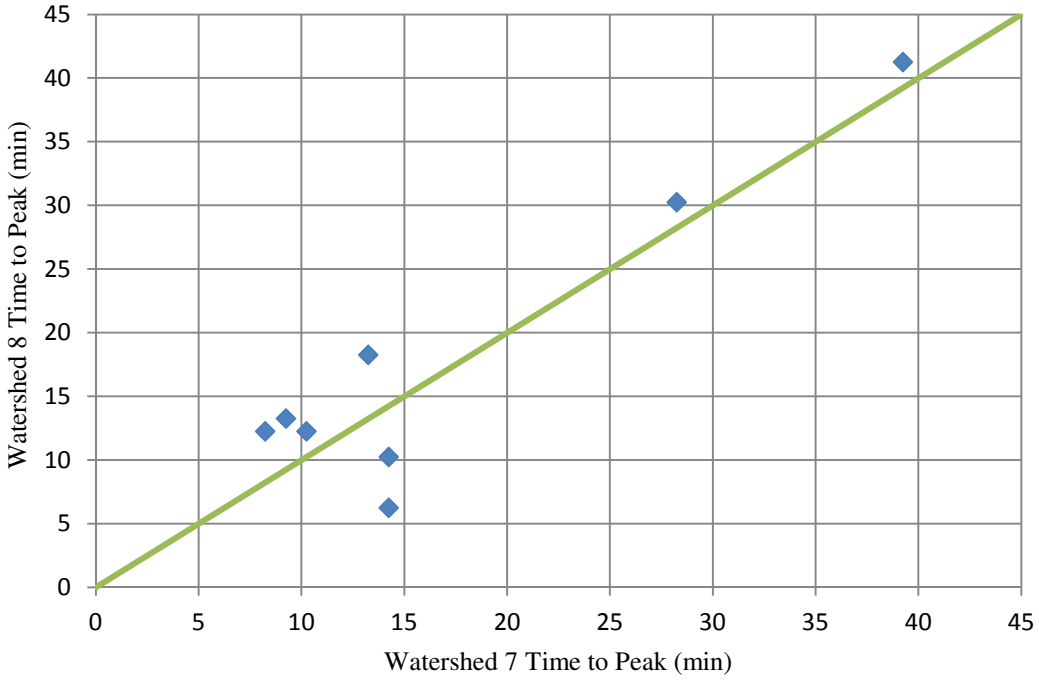

Figure 20: Time to peak runoff comparison between watersheds 7 and 8 for summer 2011.

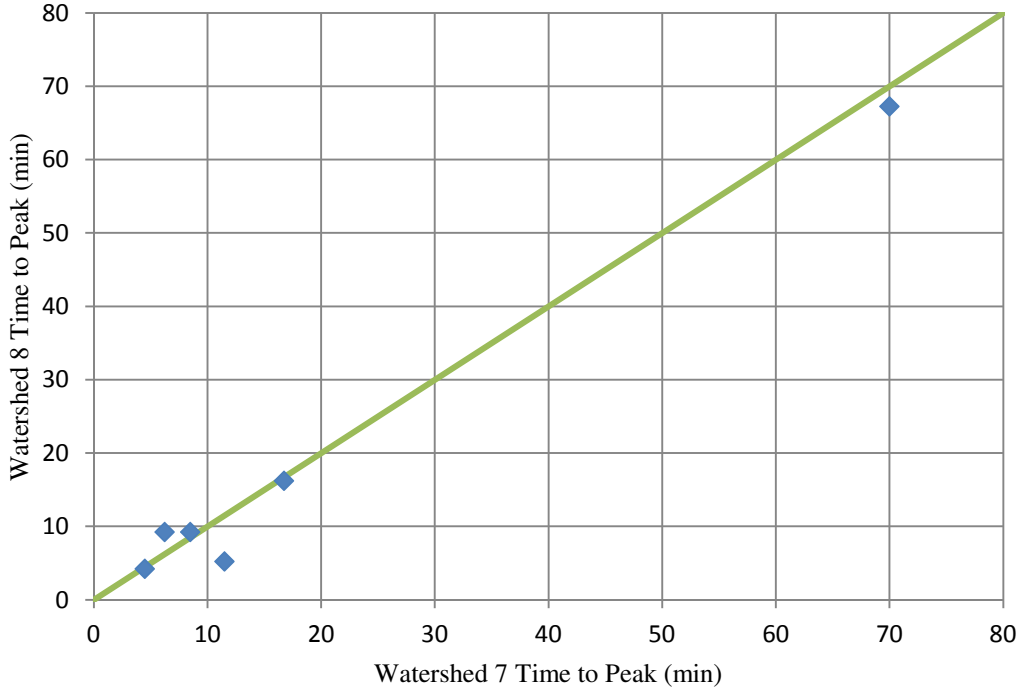

Figure 21: Time to peak runoff comparison between watersheds 7 and 8 for summer 2012.

In 2011, the time to peak runoff rates were generally higher in watershed 8 compared to watershed 7. In 2012, the time to peak runoff rates were more comparable. The average time to peak for watershed 7 in 2011 was 14.95 minutes and in 2012 was 18.18 minutes. The first event in summer 2012 was not included in calculations for watershed 7 because the storm was very long and not characteristic of a NAM event. The peak runoff rate was low and runoff rate was very steady. The average time to peak for watershed 8 in 2011 was 18.0 minutes and in 2012 was 18.58 minutes. Both years saw a longer average time to peak at watershed 8. This may be explained by mesquite trees physically intercepting or obstructing runoff on watershed 8. Therefore, the runoff may take longer to reach its way to the channel. There are also different channel widths and stems, which have been previously derived and field verified in Figure 6 from section 2.3, which can affect the times to peak runoff rate.

Comprehensive analysis of historical rainfall and runoff data has allowed a better understanding of the different runoff generation patterns that have developed on the mesquite encroached watershed and the mesquite treated watershed. The actual ecohydrological mechanisms that are in effect are more difficult to decipher. By employing a distributed hydrological model that can represent different vegetation types, different soil types, and spatial variability in rainfall, a more complete understanding of the basin mechanisms to generate runoff can be obtained.

3.4 Point-Scale Modeling Calibration and Validation

The physical hydrologic model, tRIBS, was applied to compare hydrologic and energy states and flux observations with model simulations. Point-scale simulations were applied at the eddy covariance tower for summer 2011 and summer 2012. The summer 2011 study period was used to calibrate vegetation and soil parameters to obtain a better match between the modeled and observed hydrological and meteorological processes. The point-scale simulations consist of one polygon with one specific soil and vegetation type. At the eddy covariance tower, grass vegetation and soil cover parameters were used and calibrated, and are specified in Appendix G. The summer 2012 study period was used for validation. The calibration strategy followed the outline from Ivanov et al. (2004b) in terms of relative importance for each parameter. The different hydrologic variables that were tested for the simulations and observations included volumetric soil moisture in the top 10 cm (m^3/m^3), volumetric soil moisture in the top 1 m (m^3/m^3), latent heat flux (W/m^2), sensible heat flux (W/m^2), surface temperature (^oC), and net radiation (W/m^2). All parameters are static during the simulations, so the calibration effort was aimed to match observations once the NAM had onset. The simulation was using vegetation and soil values that matched NAM season conditions, so vegetation was 'green' with water in the system, therefore the time period prior to the NAM was not expected to match observations well. The modeled parameters for the calibration period against observations are shown in Figure 22, with Figure 23 showing the modeled parameters against observations for the validation period. To quantify the comparisons,

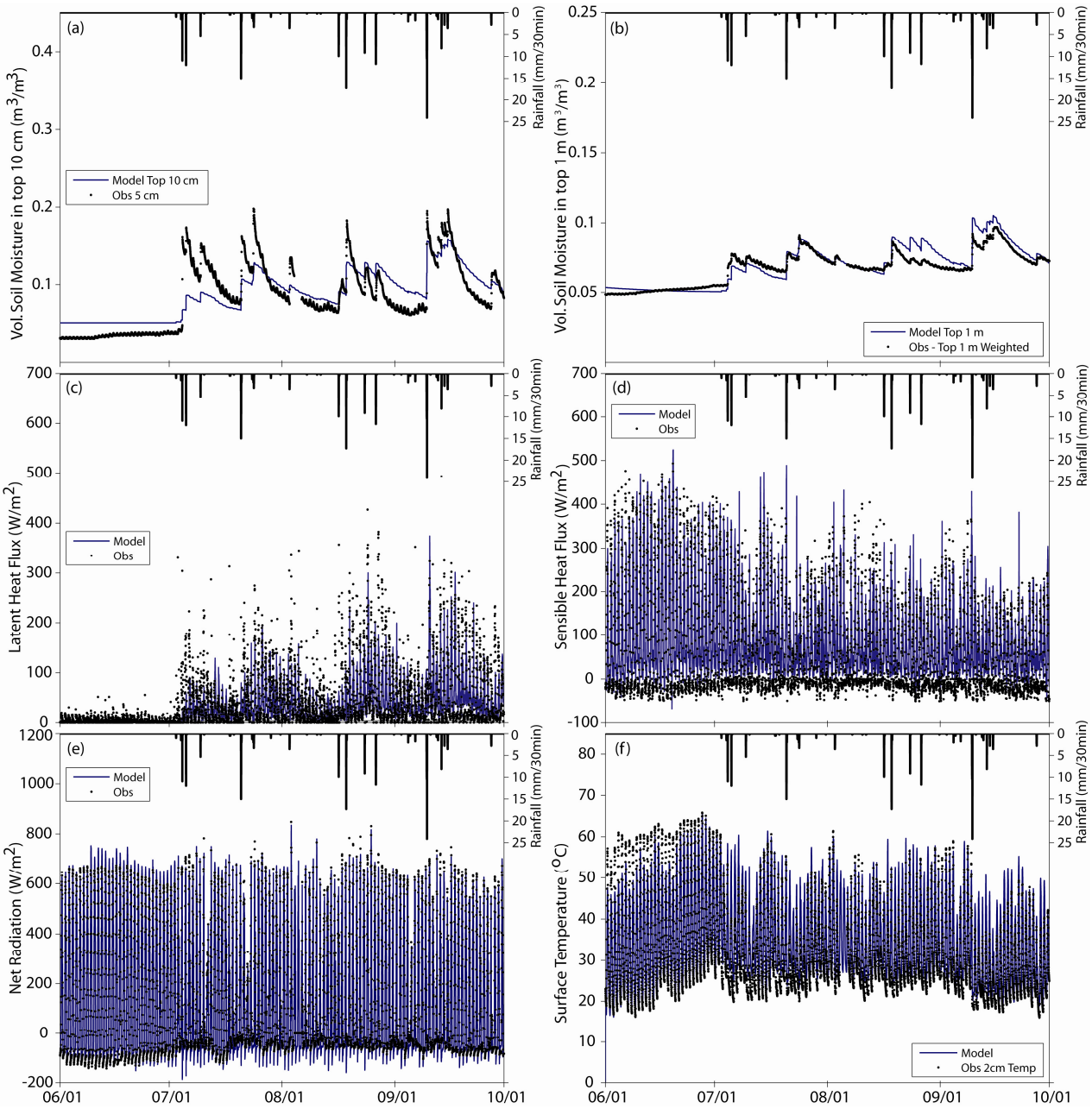

Figure 22: Summer 2011 (calibration period) point-scale simulations vs. observations for (a) volumetric soil moisture in the top 10 cm (b) volumetric soil moisture in the top 1 m (c) latent heat flux (d) sensible heat flux (e) net radiation and (f) surface temperature.

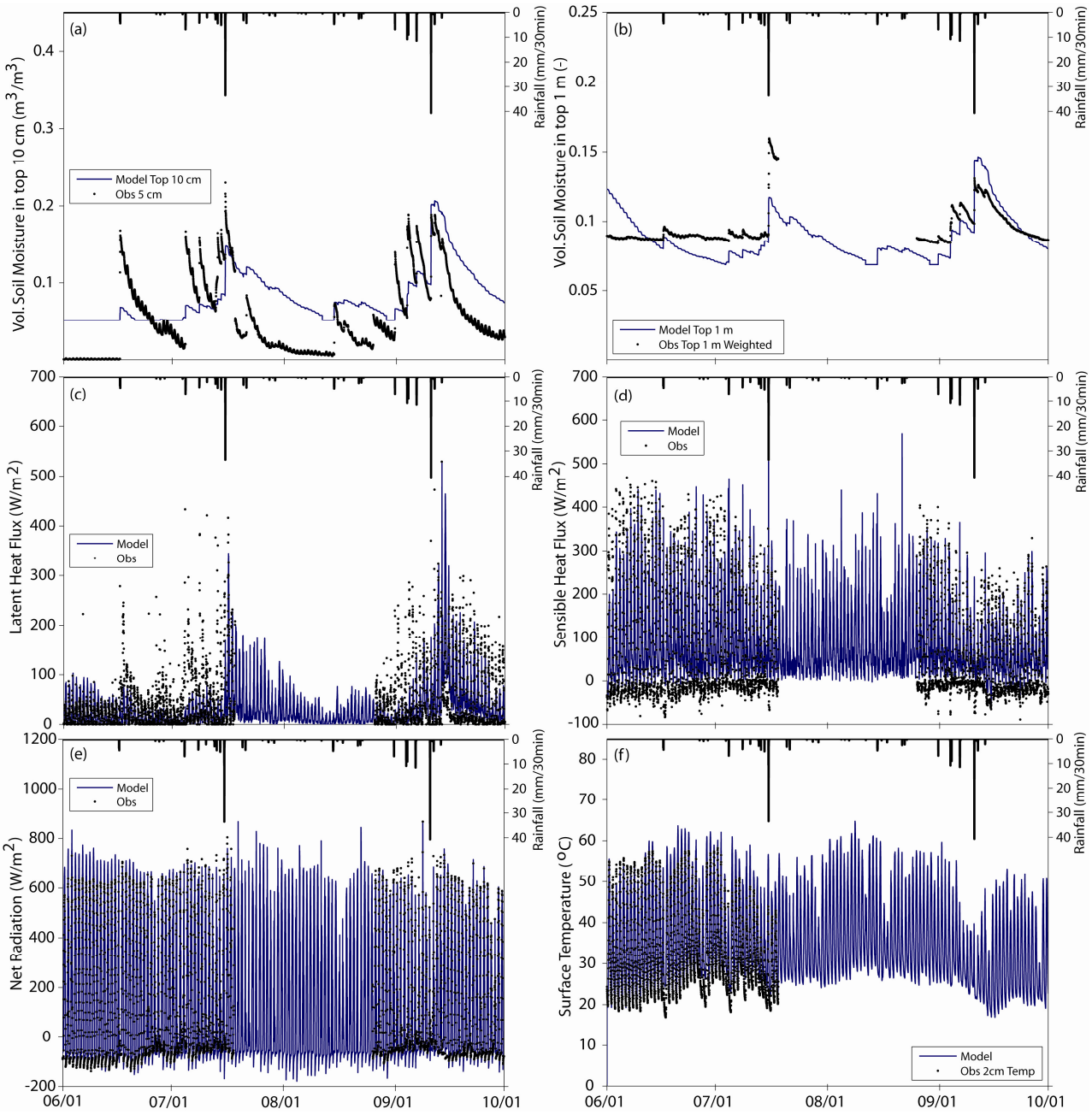

Figure 23: Summer 2012 (validation period) point-scale simulations vs. observations for (a) volumetric soil moisture in the top 10 cm (b) volumetric soil moisture in the top 1 m (c) latent heat flux (d) sensible heat flux (e) net radiation and (f) surface temperature.

Table 8: Statistical metrics to quantify parameter comparability between field observations and simulations at the point scale.

Point Scale Simulations:	*2011 - Calibration*			*2012 - Validation*		
	Bias (-)	MAE (variable units)	CC (-)	Bias (-)	MAE (variable units)	CC (-)
Soil Moisture up to 10 cm (m^3/m^3)	1.05	0.019	0.84	0.75	0.048	0.52
Soil Moisture up to 1 m (m^3/m^3)	1.03	0.004	0.93	0.93	0.012	0.61
Surface Temperature (^oC)	1.09	4.07	0.91	1.08	6.80	0.61
Latent Heat Flux (W/m^2)	0.76	27.6	0.61	0.67	33.9	0.45
Sensible Heat Flux (W/m^2)	1.33	76.6	0.63	1.31	76.4	0.48
Net Radiation (W/m^2)	0.96	62.6	0.92	0.95	107.1	0.80

Table 8 provides a summary of the bias (B), mean absolute error (MAE), and correlation coefficient (CC) calculated for each hydrologic variable.

Summer 2011 precipitation events were more frequent, but smaller compared to summer 2012 precipitation events. Also, the basins were very dry prior to the NAM onset in summer 2011 with no precipitation since April 9, 2011. The NAM onset in summer 2012 was preceded by more late spring rainfall, with events having occurred on April 14, 2012 and May 9, 2012. These differences led to different model initializations.

The summer 2011 simulations were run with depth to ground water table set at 900 mm, while the summer 2012 simulations were run with depth to ground water table set at 800 mm. The volumetric soil moistures in the top 10 cm and the top 1 m match very well for summer 2011. The top 10 cm modeled values are compared against a soil

moisture sensor at the tower place at a 5 cm depth. The top 1 meter observation is a weighted average taken from the six soil moisture sensors at 5 cm, 15 cm, 30 cm, 50 cm, 75 cm, and 1 m depths. Moisture peaks and timing of peaks are captured well by the model. The soil moistures are not as well modeled for summer 2012, as B and CC are lower while MAE is higher. The top 10 cm observations are more sensitive to precipitation input than the model. The model doesn't seem to be able to reach the minimum soil moisture values that are being measured in the field. However, the mean simulation values match favorably with the observations and the CC shows that general patterns are being followed. Both simulations tend to slightly underestimate latent heat flux and overestimate sensible heat flux; however a general correlation between simulations and observations is realized for both years. Before or after precipitation events show the most inconsistency between the simulations and observations which may be a consequence of the eddy-covariance measurement technique for latent heat and sensible heat fluxes (Scott et al., 2004, 2010). It is also notable that the observations are representative of the eddy covariance tower footprint, on the order of several hundred square meters, compared to the modeled voronoi polygon of 100 m^2. The observations also represent the variable vegetation type's onsite, while the model only applies one vegetation type. Net radiation matches fairly well for both simulation periods. Pre-monsoon (June) shows that the model is overestimating net radiation, but this is due to vegetation and soil parameters set to monsoon conditions. Once the NAM has onset, the net radiation matches much better. The surface temperature for both simulation periods is comparable. Generally the model is not capturing the night-time low surface

temperatures. This also may be the cause to the overestimation of sensible heat flux seen in the simulations. Both the surface temperature and net radiation statistical metrics showed strong correlation between the modeling efforts and the observations.

As another caveat, most of the tower sensors were non-operable for a large part of summer 2012, mid-July to late-August, due to missing batteries. Since the parameters are static and were calibrated to match the observations during the NAM (July to September), few observations are available to compare to the model. The observation pre-monsoon were used in the calculation of the statistical metrics shown in Table 8. This leads to generally worse statistical matches than what may be obtained had the missing observation period been able to be included.

3.5 Spatiotemporal Soil Moisture Variability with Basin Scale Modeling

Once satisfactory calibration was obtained for the grass vegetation type, basin scale simulations for both years were run for watershed 7 and 8. General patterns observed from the point scale calibration methods were applied to the mesquite and bare vegetation and soil parameters. Volumetric soil moisture in the top 10 cm (m^3/m^3) was compared from the simulations to observations. Observations were based on the soil moisture network distributed through watershed 8. Upon installation, the sensors were placed under grass, under mesquite, or in a bare area. The distributed hydrologic model is capable of producing a time series of hydrologic variables for a specific polygon specified by the user. The spatial locations of the sensors in the field were matched to their locations in the distributed model. The vegetation type assigned to the polygon in

the model was verified to match the field sensor vegetation specification. Then the averages of the observations across a specific vegetation type (grass, mesquite, or bare sites) were taken and compared to the averages of the simulations across that vegetation type. The results of this analysis are shown in Figure 24. Standard deviations were also computed to understand variability across the sites. Additional statistical metrics were computed to evaluate the differences between the observations and the simulations and are summarized in Table 9.

Generally for both simulation periods, the grass observation sites match very well with the simulations. The timing of the soil moisture peaks is modeled well and indicative of the precipitation pulses. The recession curves during inter-storm periods are also simulated very well for the grass sites. The ability to calibrate the grass parameters at the point-scale enabled a good grass representation for the basin dynamics. Variability between sites is the largest at the grass sites for both the observations and the simulations. The grass sites also show the highest moisture values compared to the mesquite sites and bare sites for both simulation periods. The mesquite sites are the next wettest with the bare sites have the lowest soil moisture values. The mesquite soil moisture averages match well between observations and simulations. For the summer 2011 period, the soil moisture peaks are comparable; however the observations have a steeper recession curve compared to the model. The model is keeping more moisture at the mesquite sites than what is observed. For the summer 2012 simulation, the model simulates the early season soil moisture peaks well, but overestimates the amount of moisture later in the season. Again, the model keeps more moisture at the mesquite sites with less steep recession

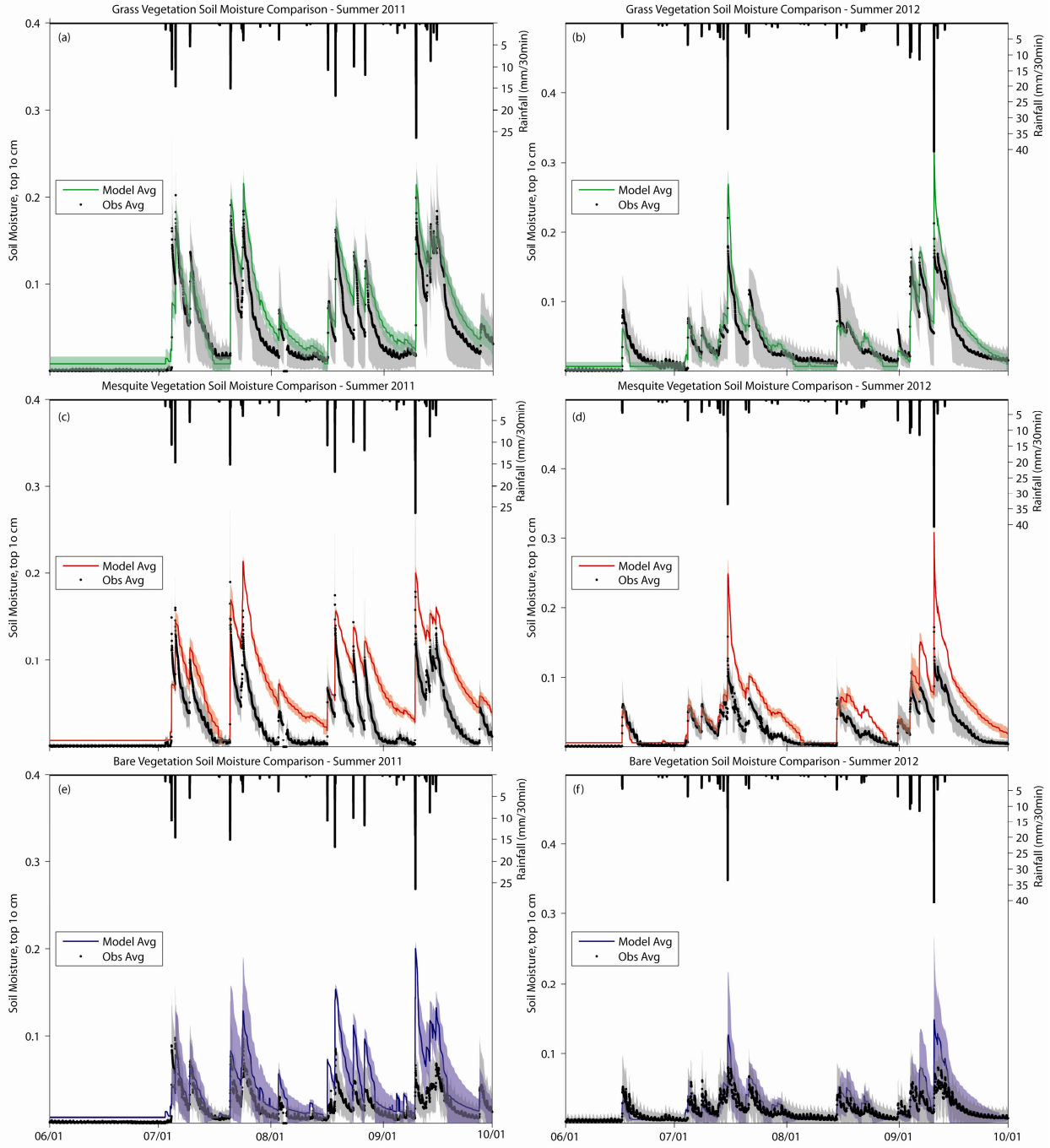

Figure 24: Comparisons of spatially averaged soil moisture in the top 10 cm (m^3/m^3) from simulations and observations for (a) grass sites for summer 2011 (b) grass sites for summer 2012 (c) mesquite sites for summer 2011 (d) mesquite sites for summer 2012 (e) bare sites for summer 2011 and (f) bare sites for summer 2012. Standard deviations for the simulations are shown with the color (green, red or blue) shading and standard deviations for the observations are shown with the gray shading.

Table 9: Watershed 8 basin scale simulations for summer 2011 and summer 2012 comparing the simulated average soil moisture values at each vegetation type to the average observations.

Watershed 8 Basin Scale Simulations:	2011 - Calibration			2012 - Validation		
	Bias (-)	MAE (variable units)	CC (-)	Bias (-)	MAE (variable units)	CC (-)
Grass Soil Moisture up to 10 cm (m^3/m^3)	1.3774	0.1138	0.9447	1.1396	0.1160	0.9420
Mesquite Soil Moisture up to 10 cm (m^3/m^3)	2.2768	0.1254	0.8901	1.9061	0.1071	0.9202
Bare Soil Moisture up to 10 cm (m^3/m^3)	2.0316	0.0639	0.8182	1.2744	0.0497	0.8569

curves. The mesquite sites have the lowest variability for the model and the observations. The simulations for the soil moisture at the bare sites is consistently overestimating compared to the observations for both simulation periods. There is relatively large variability in the simulations for the bare sites. The timing of the soil moisture peaks for the bare sites match very well between the simulations and the observations.

Overall, the model is able to capture the spatial variability of volumetric soil moisture specific to the vegetation type. It gives higher soil moisture values at the grass and mesquite sites, with the lowest soil moisture at the bare sites. The model is indicating that the mesquites sites retain higher values of soil moisture during inter-storm periods. The model is also revealing that even at times of very high precipitation input, the bare sites do not have the soil moisture peaks that the vegetated sites have, which is also recognized in the observations. The lack of soil moisture peaks in the top 10 cm indicate that the precipitation at these sites is most likely turning into runoff. It is important that the model is able to capture a possible runoff generating dynamic to aid in the understanding of runoff implications due to woody plant encroachment.

To further explore the vegetation dynamics on the basin scale models, various time-integrated spatial maps were explored. Figure 25 shows the number of infiltration-excess runoff occurrences observed at each polygon over the simulation period, relative to the 30 minute time step. There were zero occurrences of saturation-excess runoff. As Figure 25 shows, the summer 2012 simulation period was generally wetter. More runoff occurrences were present at all of the vegetation types with the highest number occurring at bare sites. There is slight evidence of the different rain gauges used as a meteorological input. The rain from the gauges was modeled using theissen polygons. Figure 26 shows the average evapotranspiration (mm/hr) across both basins for both simulation periods. There is a greater influence of the theissen polygon precipitation forcing. The summer 2012 simulation had larger amounts of evapotranspiration for both basins.

The time-integrated spatial patterns of volumetric soil moisture (m^3/m^3) up to 10 cm and up to 1 m are shown in Figures 27 and 28, respectively. The soil moisture patterns are linked with one another and are very similar to the evapotranspiration rates. Although summer 2012 was generally wetter, there is no evidence to higher soil moisture in the top 10 cm between the two simulation periods. Interestingly, over both simulation periods, there is a threshold to the amount of soil moisture in the top 10 cm. This may indicate that differences in other processes, such as average evapotranspiration or runoff, would then be dictated by variables other than soil moisture in the top 10 cm. There is

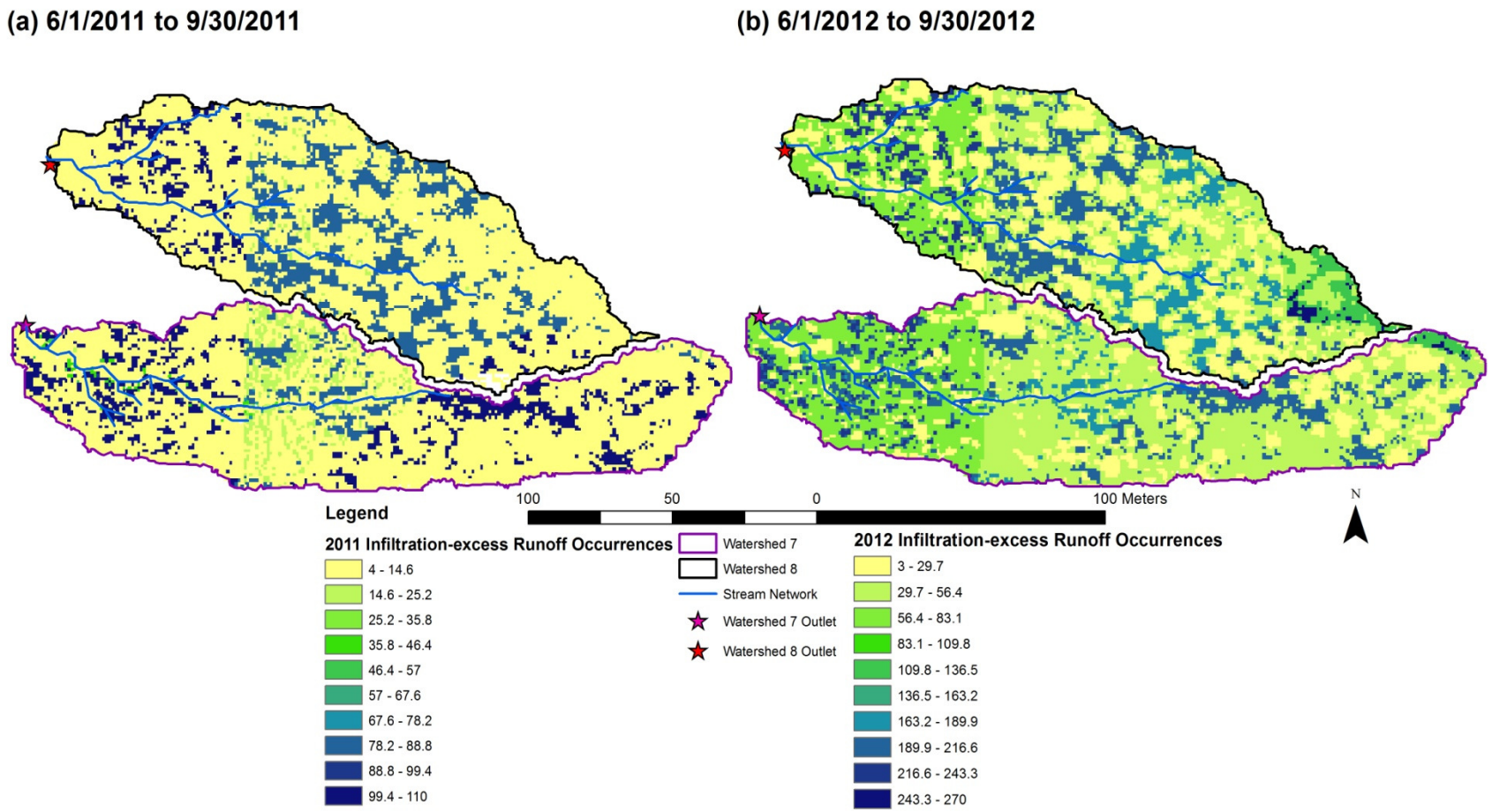

Figure 25: Number of infiltration-excess runoff occurrences relative to the 30 minute time step at each polygon in the distrusted model for (a) summer 2011 simulation period and (b) summer 2012 simulation period.

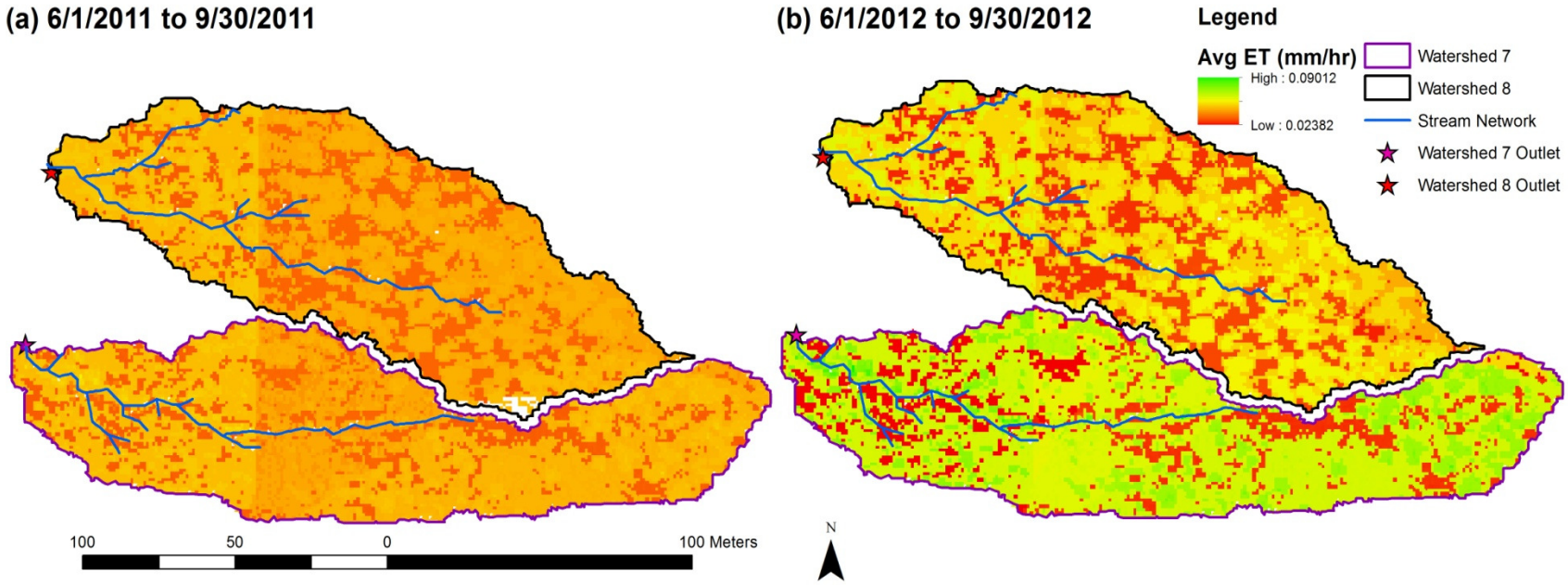

Figure 26: Time-integrated spatial representation of average evapotranspiration (mm/hr) for (a) summer 2011 simulation period and (b) summer 2012 simulation period.

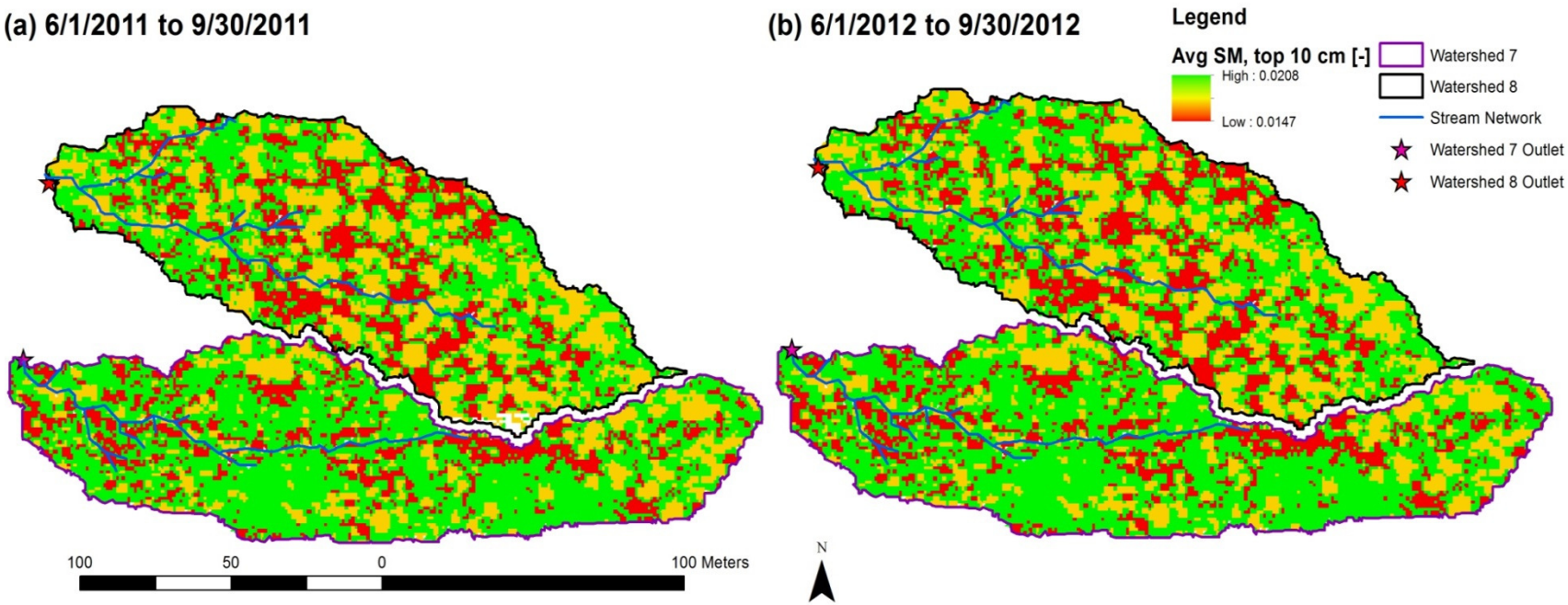

Figure 27: Time-integrated spatial representation of average volumetric soil moisture up to 10 cm (m^3/m^3) for (a) summer 2011 simulation period and (b) summer 2012 simulation period.

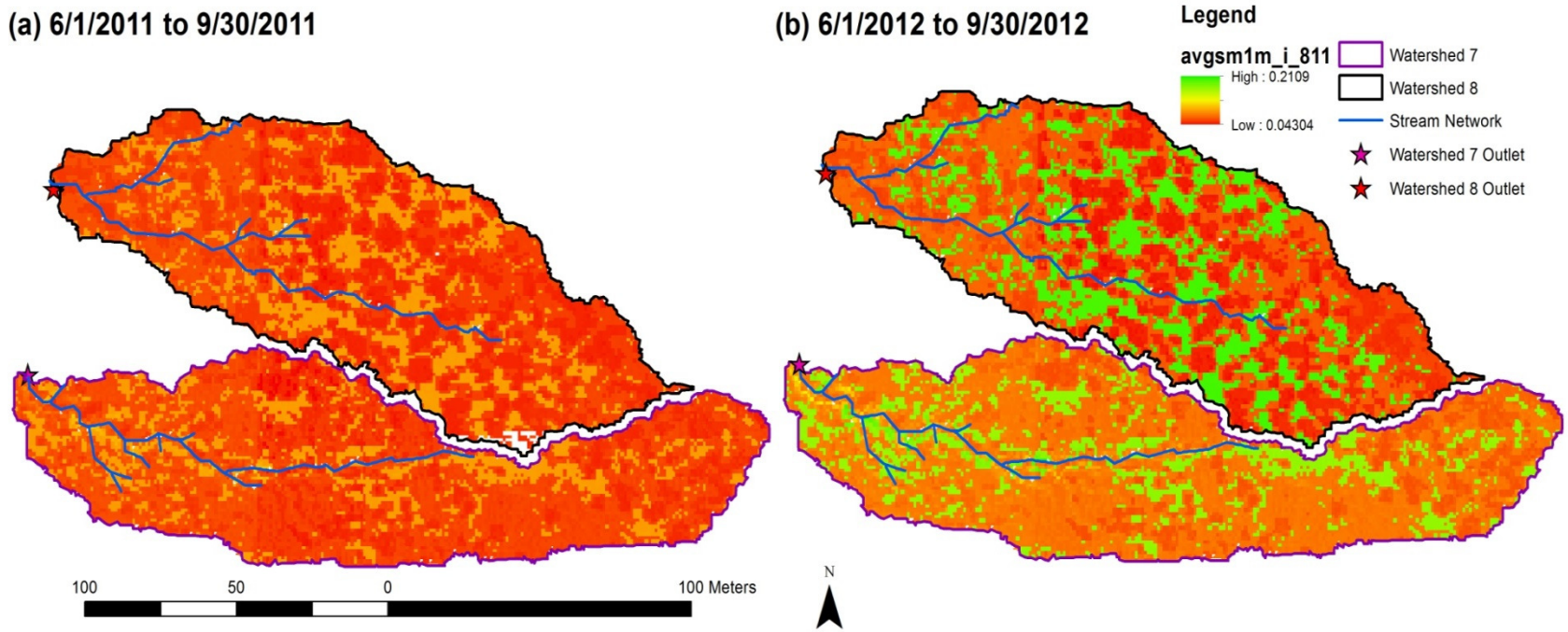

Figure 28: Time-integrated spatial representation of average volumetric soil moisture up to 1 meter (m^3/m^3) for (a) summer 2011 simulation period and (b) summer 2012 simulation period.

much more variability between the two simulation years for soil moisture in the top 1 m. The summer 2012 period has higher values, indicating that more infiltration occurred.

3.6 Basin Scale Runoff Modeling

To further analyze the basin scale simulations for both simulation periods, the runoff at each watershed outlet was compare and analyzed. The model is capable of producing runoff hydrographs over the simulation period at specified internal nodes along the stream network. Three internal nodes were specified to match the locations of the three installed internal flumes at the watershed 8 site. The basin calibrated vegetation and soil parameters were not altered. The first objective in the calibration approach was to best match soil moisture dynamics in the basin. The second objective was to match runoff timing and volume. This proved to be a difficult task. Tables 10 and 11 give statistical metrics that were used to compare the observed runoff to the simulated runoff for watershed 7 and watershed 8, respectively.

Generally, the internal flumes (Flume 1, 2, and 3) did not match well with the simulated runoff. There are multiple possibilities for error to be introduced. In the field, the runoff data at the internal flumes is determined through pressure transducer measurements of water height through the flume. Since these systems are ephemeral, the pressure transducer is only measuring water height when a significant runoff event occurs. However the design of the flume is to place the pressure transducer in a still, which sits lower than the throat of the flume. This causes the initial water flowing through the flume at the beginning of a runoff event to fill the still, rather than flow

Table 10: Watershed 7 basin scale simulations for summer 2011 and summer 2012 comparing the simulated runoff rates to the observed runoff rates

Watershed 7 Basin Scale Simulations:	2011 - Calibration			2012 - Validation		
	Bias (-)	MAE (variable units)	CC (-)	Bias (-)	MAE (variable units)	CC (-)
Outlet Flume Runoff (m^3/s)	18.80	0.00073	0.027	21.92	0.0012	0.297

Table 11: Watershed 8 basin scale simulations for summer 2011 and summer 2012 comparing the simulated runoff rates to the observed runoff rates

Watershed 8 Basin Scale Simulations:	2011 - Calibration			2012 - Validation		
	Bias (-)	MAE (variable units)	CC (-)	Bias (-)	MAE (variable units)	CC (-)
Outlet Flume Runoff (m^3/s)	12.58	0.00049	0.328	7.43	0.00056	0.579
Flume 1 Runoff (m^3/s)	13.73	0.00014	0.287	51.3*	0.00016*	-0.011*
Flume 2 Runoff (m^3/s)	70.06	0.00046	0.308	1.75	0.00077	0.502
Flume 3 Runoff (m^3/s)	40.15	0.00017	0.273	1.22	0.00034	0.443

* Flume 1 sensor was only operating for 8/22/2012 to 9/30/2013 of the simulation period, resulting in poor statistical correlation

through the flume and give an accurate pressure measurement. To attempt to alleviate this design flaw, the stills were filled with water upon every data collection trip, approximately every 3 to 4 weeks. However, these are semiarid environments with high evaporation rates, so unless a runoff event occurred directly after the filling of a still, there is a high likelihood of a lagged response in the pressure transducer measurements. This effect was also considered when post-processing the data, however depending on the size and intensity of the event, there was a different lag to fill the still. This is the most likely reason behind the large discrepancies between the modeled and observed runoff at these internal locations. The second cause is due to an overestimation of total runoff for both simulations in general. The validation period, summer 2012, actually saw a better

Table 12: Total runoff (m^3) and number of runoff events simulated at the outlet flumes for watersheds 7 and 8 for both simulation periods.

Basin	Total Runoff (m^3)	Number of Runoff Events
Watershed 7 2011	157.3566	6
Watershed 8 2011	68.8875	4
Watershed 7 2012	227.1861	10
Watershed 8 2012	105.6344	5

correlation with outlet runoff at watershed 8 than the calibration period, summer 2011. The bias at watershed 7 was much higher for both simulation periods compared to watershed 8. Figure 29 shows the runoff rates over both simulation periods for both study basins at the outlet flumes compared to observations. Watershed 7 produced more runoff events for both summer 2011 and summer 2012 in both the observations and simulations. Watershed 7 also produced more total runoff volume, as summarized in Table 12. Watershed 8 however produced larger runoff volumes for the largest precipitation events, again similar to patterns observed in Section 3.3. Figure 30 shows the runoff rates from observations and simulations over both simulation periods for the three internal flumes at watershed 8. More runoff was simulated at flume 2 compared to flume 1, which matches field observations. Flume 2 is downstream from flume 1.

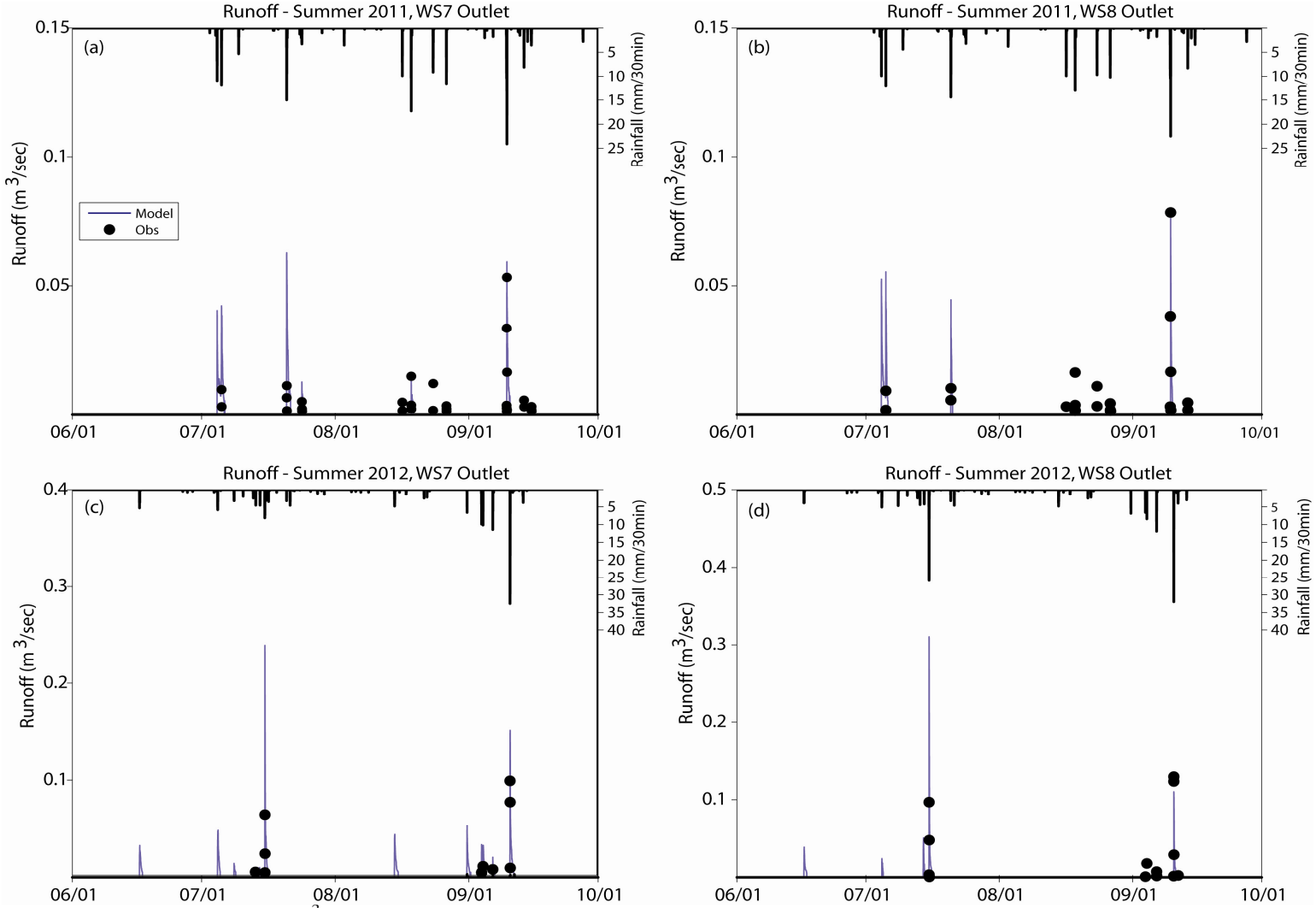

Figure 29: Simulations of runoff (m^3/sec) compared to observations at (a) watershed 7 outlet flume, summer 2011 (b) watershed 8 outlet flume, summer 2011 (c) watershed 7 outlet flume, summer 2012 and (d) watershed 8 outlet flume, summer 2012.

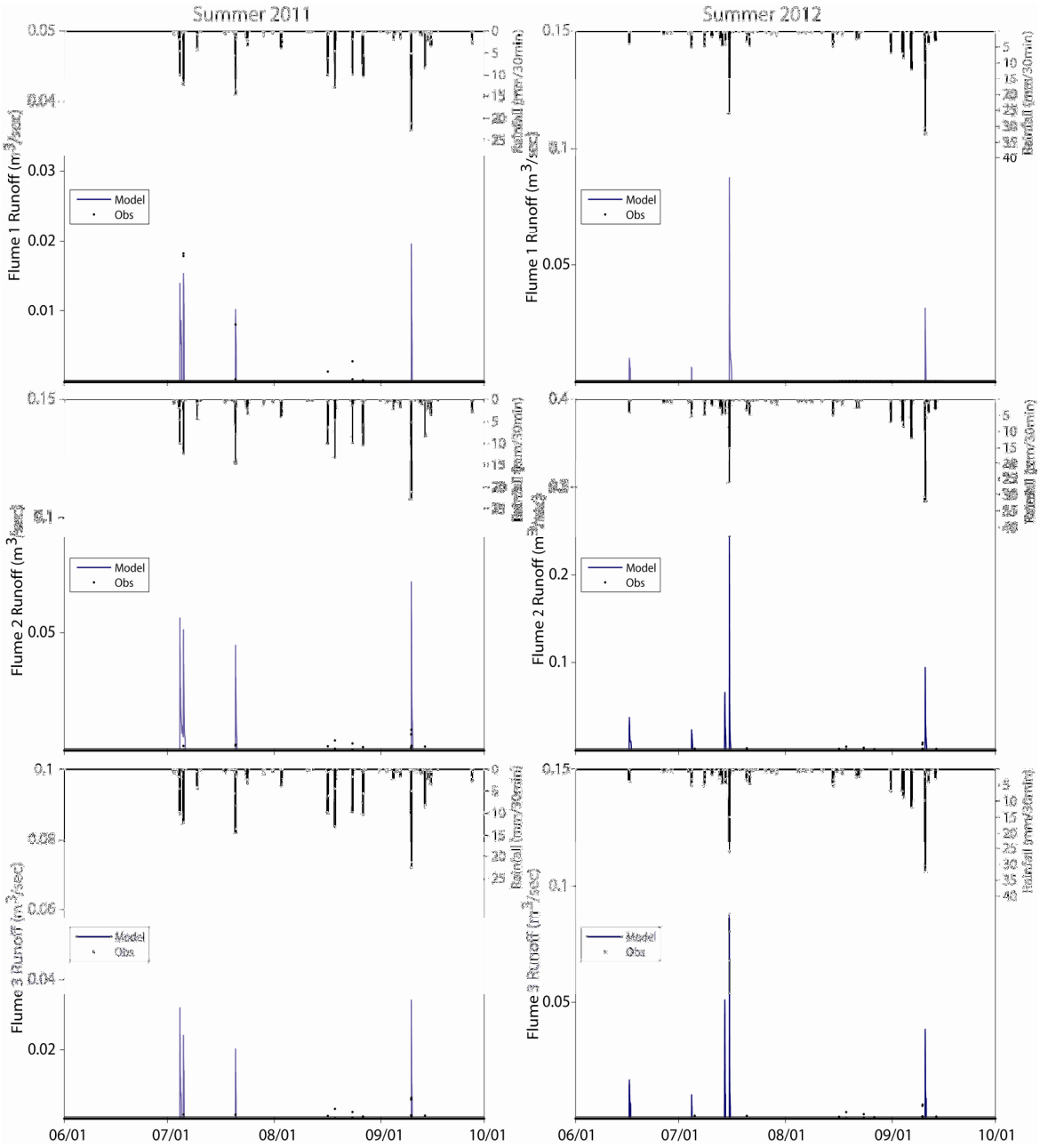

Figure 30: Simulations of runoff (m^3/sec) compared to observations at (a) flume 1 during summer 2011 (b) flume 1 during summer 2012 (c) flume 2 during summer 2011 (d) flume 2 during summer 2012 (e) flume 3 during summer 2011 and (f) flume 3 during summer 2012.

3.7 Basin Scale Runoff Sensitivity to Vegetation

To test the sensitivity of the runoff output from the model simulations, three additional vegetation maps were examined. The three different vegetation scenarios tested are as follows: all grass, all bare soils, and all mesquites. By comparing how the runoff varies between the two basins for the two simulations years under the three different vegetation scenarios, emerging patterns should help identify the mechanisms at work in generating runoff.

Runoff generation was examined at the outlet flume for both watersheds 7 and 8 for both simulation periods. Figures 31, 32, and 33 present the outlet flume runoff simulated at each basin for the grass scenario, the bare soil scenario, and the mesquite scenario, respectively. The grass scenarios produced less total runoff than the variable vegetation maps for watershed 7 and 8 in summer 2011 and watershed 7 in summer 2012. However, the grass only simulation for watershed 8 in summer 2012 generated more total runoff. The bare scenarios produced more total runoff for both basins in summer 2011 and summer 2012. The mesquite scenario generated the least total amount of runoff. Compared to the variable vegetation maps, the mesquite only scenarios generated less total runoff volume for both watersheds for both simulation periods. Summer 2012 had more total runoff and more runoff events from observations, and each of the three simulated scenarios were able to capture that same pattern. The grass scenarios produced less runoff events for summer 2011 in both watershed 7 and 8. For summer 2012, less runoff events were produced for the grass scenario compared to the observations in watershed 7, however a greater number of events were produced in watershed 8. The

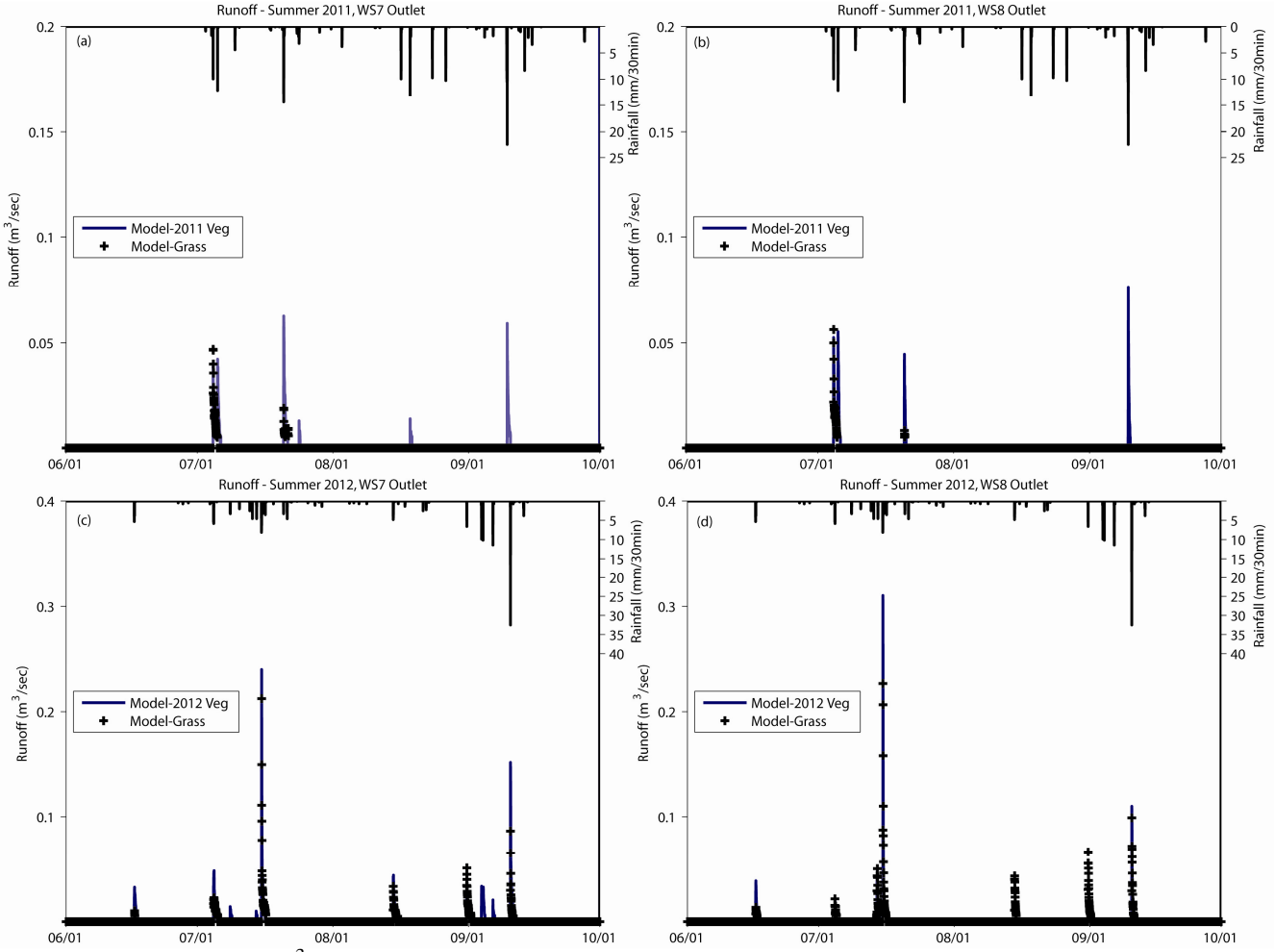

Figure 31: Comparison of the runoff (m^3/sec) at the outlet flumes for the spatially variable vegetation pattern vs. grass only vegetation for (a) outlet at watershed 7 for summer 2011 (b) outlet at watershed 8 for summer 2011(c) outlet at watershed 7 for summer 2012 and (d) outlet at watershed 8 for summer 2012.

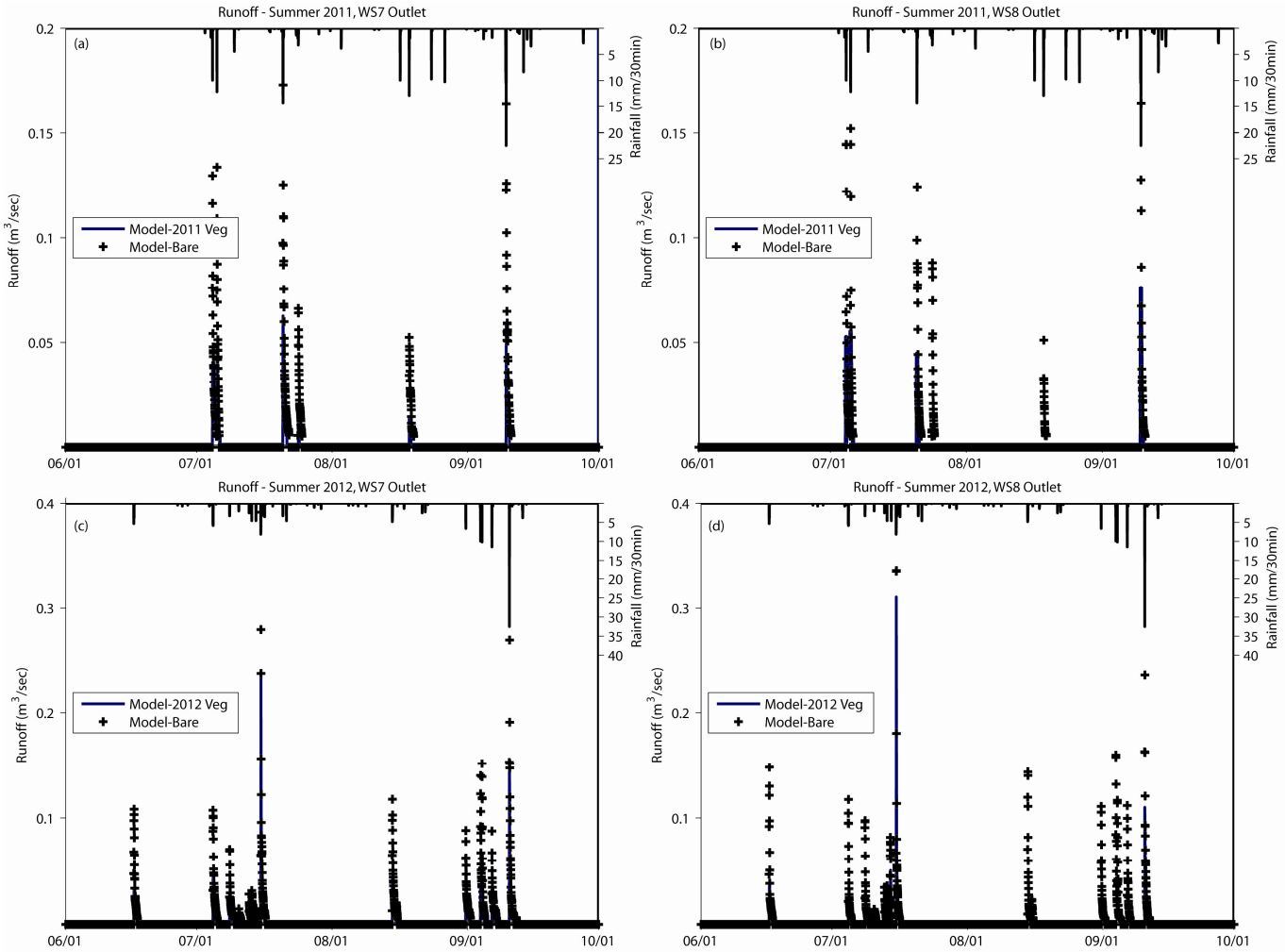

Figure 32: Comparison of the runoff (m^3/sec) at the outlet flumes for the spatially variable vegetation pattern vs. bare only vegetation for (a) outlet at watershed 7 for summer 2011 (b) outlet at watershed 8 for summer 2011(c) outlet at watershed 7 for summer 2012 and (d) outlet at watershed 8 for summer 2012.

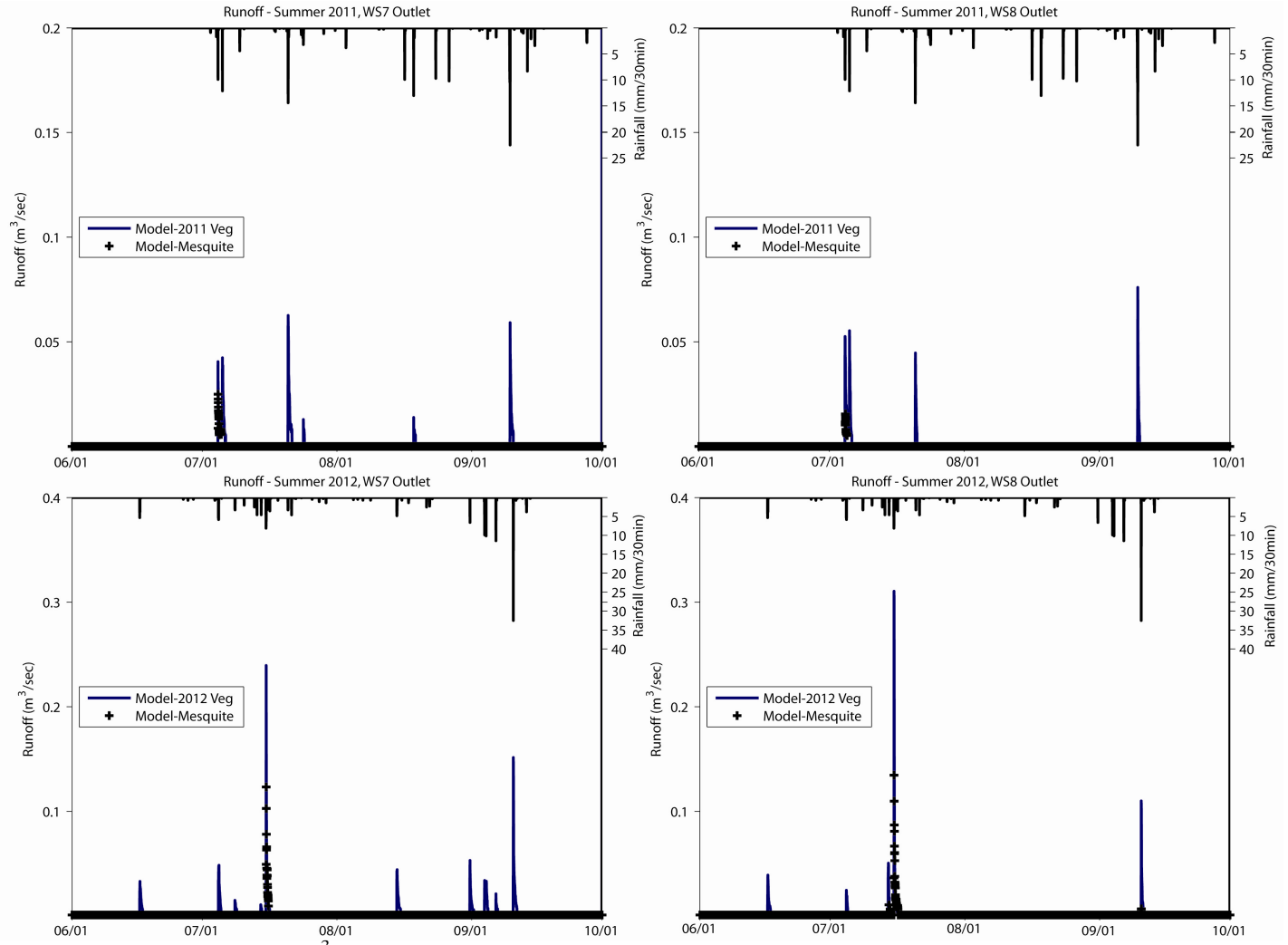

Figure 33: Comparison of the runoff (m^3/sec) at the outlet flumes for the spatially variable vegetation pattern vs. mesquite only vegetation for (a) outlet at watershed 7 for summer 2011 (b) outlet at watershed 8 for summer 2011(c) outlet at watershed 7 for summer 2012 and (d) outlet at watershed 8 for summer 2012.

bare scenarios always generated more runoff events for both basins and both periods. The mesquite scenarios always generated less runoff events for both basins and both periods. Table 13 summarizes the grass only vegetation simulation runoff compared to the variable vegetation for both watersheds during both simulation periods. The change in total runoff volume is analyzed as the difference between the runoff generated with variable vegetation land cover map compared to the runoff generated with the grass only vegetation land cover map. The change in the number of runoff events is also evaluated. Comparisons of the bare only vegetation and mesquite only vegetation runoff generation patterns are also evaluated against the variable vegetation land cover maps and summarized in Table 15 and Table 17, respectively. To further understand the runoff generation patterns for the different vegetation land cover scenarios, the bias and correlation coefficients were calculated for the simulations versus the observations. Metrics were calculated for both watersheds (7 and 8) for both simulations periods (summer 2011 and summer 2012). Tables 14, 16, and 18 summarize the metrics for the grass only vegetation, bare only vegetation, and mesquite only vegetation, respectively. The summer 2011 simulations for watershed 8 did not match well with regards to bias for the grass only or mesquite only vegetation simulations, but was acceptable for the bare only vegetation simulation. Otherwise, the remaining simulations showed good agreement with correlation coefficient to observations.

Table 13: Comparison of variable vegetation vs. grass only vegetation on total runoff (m^3) and number of runoff events for watersheds 7 and 8 during summer 2011 and summer 2012 simulations.

Model Comparisons:		Total Runoff (m^3)	Change in Runoff (m^3)	% Change in Runoff	Number of Events	Change in Number of Events
Watershed 7	2011 Vegetation	157.36	-81.98	-52.06%	6	-4
	2011 Grass Only	75.44			2	
Watershed 8	2011 Vegetation	68.89	-47.35	-68.73%	4	-2
	2011 Grass Only	21.54			2	
Watershed 7	2012 Vegetation	227.19	-92.73	-40.83%	10	-4
	2012 Grass Only	134.42			6	
Watershed 8	2012 Vegetation	105.63	17.18	16.26%	5	2
	2012 Grass Only	122.81			7	

Table 14: Statistical metrics to compare runoff between variable vegetation and grass only vegetation.

Grass Only Metrics:		Bias (-)	CC (-)
2011	Watershed 7	2.0857	0.9939
	Watershed 8	3.1980	0.5486
2012	Watershed 7	1.6902	0.9735
	Watershed 8	0.8601	0.9033

Table 15: Comparison of variable vegetation vs. bare only vegetation on total runoff (m^3) and number of runoff events for watersheds 7 and 8 during summer 2011 and summer 2012 simulations.

Model Comparisons:		Total Runoff (m^3)	Change in Runoff (m^3)	% Change in Runoff	Number of Events	Change in Number of Events
Watershed 7	2011 Vegetation	157.36	69.26	44.02%	6	0
	2011 Bare Only	226.62			6	
Watershed 8	2011 Vegetation	68.89	270.08	392.07%	4	2
	2011 Bare Only	338.97			6	
Watershed 7	2012 Vegetation	227.19	239.16	105.27%	10	1
	2012 Bare Only	466.35			11	
Watershed 8	2012 Vegetation	105.63	425.49	402.79%	5	5
	2012 Bare Only	531.12			10	

Table 16: Statistical metrics to compare runoff between variable vegetation and bare only vegetation.

Bare Only Metrics:		Bias (-)	CC (-)
2011	Watershed 7	0.4642	0.948
	Watershed 8	0.3040	0.8362
2012	Watershed 7	0.4278	0.8999
	Watershed 8	0.2265	0.7403

Table 17: Comparison of variable vegetation vs. mesquite only vegetation on total runoff (m^3) and number of runoff events for watersheds 7 and 8 during summer 2011 and summer 2012 simulations.

Model Comparisons:		Total Runoff (m^3)	Change in Runoff (m^3)	% Change in Runoff	Number of Events	Change in Number of Events
Watershed 7	2011 Vegetation	157.36	-97.86	-62.18%	6	-5
	2011 Mesquite Only	59.52			1	
Watershed 8	2011 Vegetation	68.89	-63.08	-91.62%	4	-3
	2011 Mesquite Only	5.77			1	
Watershed 7	2012 Vegetation	227.19	-174.07	-76.64%	10	-9
	2012 Mesquite Only	53.06			1	
Watershed 8	2012 Vegetation	105.63	-68.25	-64.61%	5	-4
	2012 Mesquite Only	37.38			1	

Table 18: Statistical metrics to compare runoff between variable vegetation and bare only vegetation.

Mesquite Only Metrics:		Bias (-)	CC (-)
2011	Watershed 7	2.6439	0.9933
	Watershed 8	11.9360	0.4615
2012	Watershed 7	4.2814	0.9150
	Watershed 8	2.8259	0.8150

To further investigate runoff generation differences between the grass, mesquite, and bare vegetation scenarios, additional ecohydrological mechanisms were analyzed. Actual evaporation, evaporation from bare soil, evaporation from the dry canopy were evaluated for the three different vegetation scenarios, as shown in Figure 34, while interception and evaporation from the wet canopy were also analyzed in Figure 35.

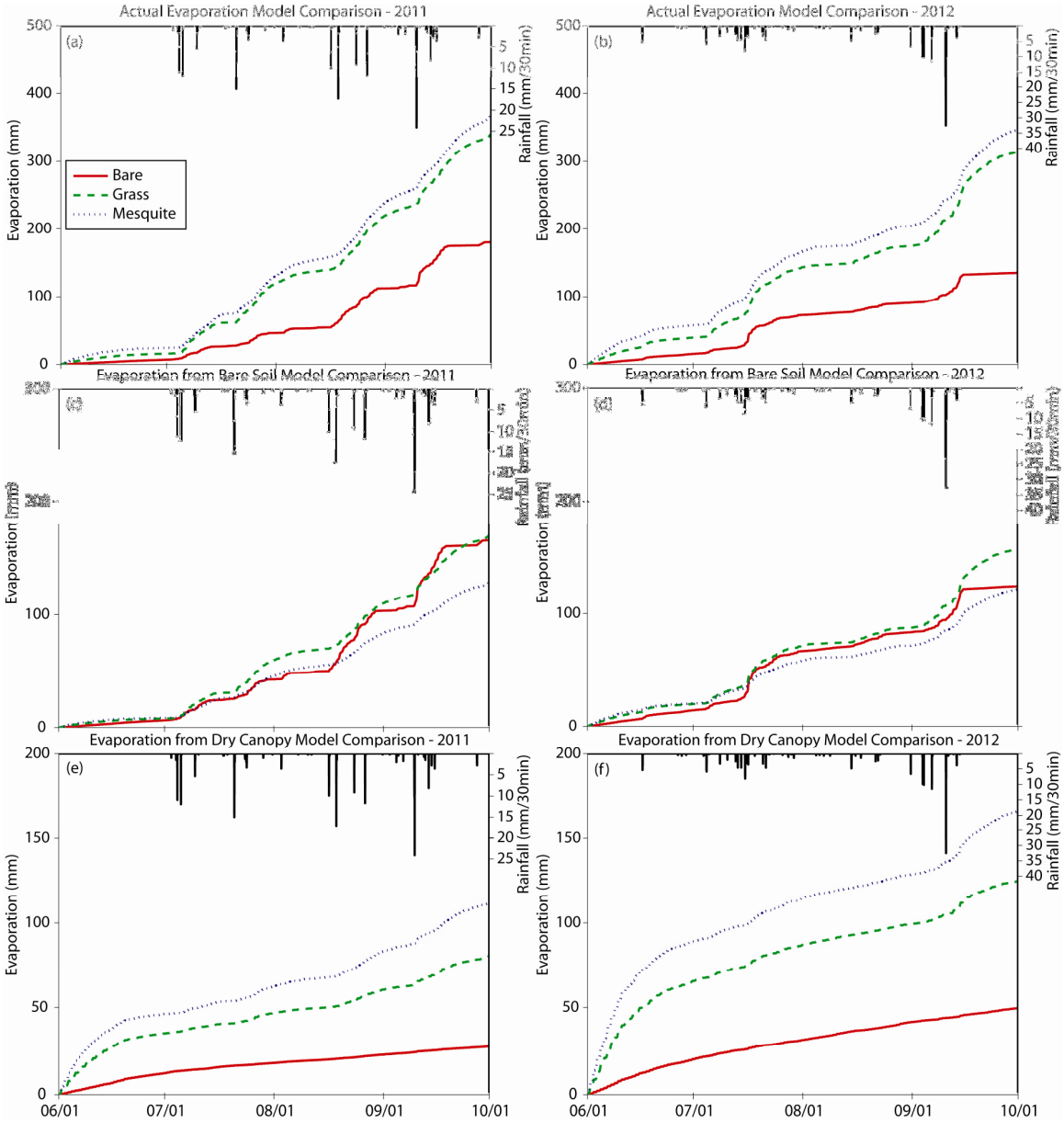

Figure 34: Cumulative comparisons of bare-only, grass-only, and mesquite-only vegetation scenarios for (a) actual evaporation in summer 2011 (b) actual evaporation in summer 2012 (c) evaporation from bare soil in summer 2011 (d) evaporation from bare soil in summer 2012 (e) evaporation from dry canopy in summer 2011 and (f) evaporation from dry canopy in summer 2012.

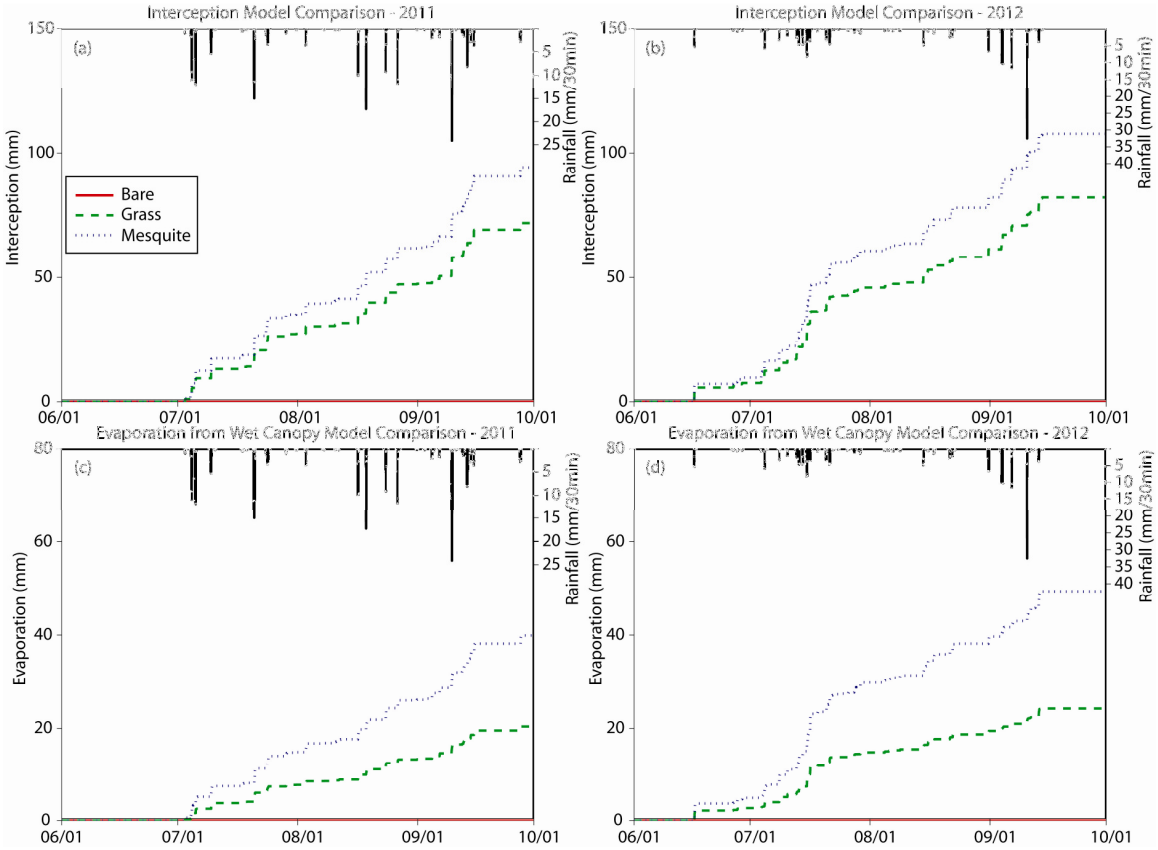

Figure 35: Cumulative comparisons of grass-only and mesquite-only vegetation scenarios for (a) interception in summer 2011 (b) interception in summer 2012 (c) evaporation from wet canopy in summer 2011 and (d) evaporation from wet canopy in summer 2012.

Cumulative plots are shown in Figures 35 and 36 to better compare the different vegetation scenarios over the entire study periods. The grass-only and mesquite-only scenarios have comparable total actual evaporation for both summer periods while bare-only scenarios have the lowest actual evaporation. Evaporation from bare soil is comparable across all three different vegetation scenarios. Evaporation from the dry canopy is highest for the mesquite-only vegetation scenario, indicating high transpiration. All three vegetation scenarios saw higher transpiration in summer 2012 compared to summer 2011, most likely due to the increased precipitation input. Grass-only vegetation has lower evaporation from dry canopy, while the bare-only scenario has the lowest

evaporation from dry canopy. The lower evapotranspiration totals indicate probable higher soil moisture for the grass and bare vegetation. As shown in Figure 35, the mesquite-only scenario has higher interception and more evaporation from the wet canopy compared to the grass-only scenario. This contributes to the higher transpiration rates seen at the mesquite-only scenario. Interception values are higher than evaporation from the wet canopy. The difference is likely representing the moisture that is moving into the soil surface as stemflow.

Many ecohydrological mechanisms have an effect on the runoff generation at the mesquite-encroached and the mesquite-treated watersheds. Evaporation, transpiration, and interception are all significant when evaluating how precipitation is distributed in these semiarid systems. By evaluating grass-only, mesquite-only, and bare-only vegetation scenarios, the sensitivity of these mechanisms is better understood. The bare-only vegetation has significantly lower evapotranspiration. Precipitation that falls onto bare vegetation is therefore more dependent on the antecedent soil moisture, as it will either infiltrate or generate runoff. This interaction between the bare vegetation and either grass or mesquite is vital in determining what key mechanisms affect runoff production in the mesquite-encroached and mesquite-treated watersheds.

3.8 Water Budget Comparisons

Through ecohydrological observations and the distributed model simulations during summer 2011 and summer 2012, a better understanding is obtained for the effect of mesquite encroachment on hydrological states and fluxes. To draw general

conclusions from the effects of mesquite encroachment, the total evapotranspiration, runoff, soil moisture storage change, and precipitation was summed for both the observations and simulations during summer 2011 and summer 2012. The resulting water budget values are presented in Table 19.

Precipitation for watershed 7 was determined from the rain gauge managed by the ARS, nearest to the basin. Precipitation for watershed 8 is calculated by averaging the four rain gauges in the basin, and the standard deviation is also included in the table. Observed runoff was determined from the outlet flumes at both watersheds 7 and 8. Observed evapotranspiration was calculated from the eddy covariance tower that lies to the north of watershed 8. Observed soil moisture storage change was determined by taking an average of the soil moisture measurements in watershed 8 and finding the difference from the initial soil moisture (at the beginning of each study period) and the final soil moisture (at the end of each study period). Simulated runoff was summed over the simulations for each study period. Simulated evapotranspiration and soil moisture storage change was determined from the basin-averaged time-series output for each simulation. The reported simulation soil moisture change was the mean soil moisture in the top 1 meter.

Table 19: Water budget variables for watersheds 7 and 8 for summer 2011 and summer 2012 study periods. The comparison includes the observed values for precipitation, runoff, evapotranspiration, and soil moisture storage change, and simulations values for runoff, evapotranspiration, and soil moisture storage change.

	Observed P (mm)			
	Watershed 7	Watershed 8		
Summer 2011	250.2	240.9 +/- 5.2		
Summer 2012	266.1	248.9 +/- 12.7		
	Observed Q Outlet (mm)		Simulated Q Outlet (mm)	
	Watershed 7	Watershed 8	Watershed 7	Watershed 8
Summer 2011	29.4	32.0	15.7	6.9
Summer 2012	50.8	74.3	22.7	10.6
	Observed ET (mm)		Simulated ET (mm)	
	Eddy Covariance Tower		Watershed 7	Watershed 8
Summer 2011	177.6		228.5	224.3
Summer 2012	198.2		222.8	215.1
	Observed dS/dt (m^3/m^3)		Simulated dS/dt (m^3/m^3)	
	Watershed 8		Watershed 7	Watershed 8
Summer 2011	0.0096		0.0013	-0.0005
Summer 2012	0.0044		0.0233	0.0045

A greater amount of precipitation fell in summer 2012 for both watersheds 7 and 8 compared to summer 2011. Generally, more observed and simulated runoff was generated for both watersheds in summer 2012 compared to summer 2011. Observed runoff generated was greater than simulated runoff for both watersheds and both study periods. Also, observed evapotranspiration was less than simulated evapotranspiration for both basins and both study periods. The observed evapotranspiration was calculated from the eddy covariance tower which is approximately 60 meters north of watershed 8 and approximately 120 meters north of watershed 7. The eddy covariance tower footprint is several hundred square meters and represents the general heterogeneous landscape. However it is not able to distinct between a grass-dominated or mesquite-dominated area.

Therefore the basin simulations are valuable in determining the basin-averaged evapotranspiration and the differences between the two watersheds are important. A greater amount of evapotranspiration for both watersheds 7 and 8 was seen in summer 2011 compared to summer 2012, when there was less precipitation input and less runoff generation. For summer 2011 the mesquite encroached watershed 8 had greater evapotranspiration compared to the mesquite treated watershed 7. However summer 2012 saw the mesquite treated watershed 7 producing more evapotranspiration than the mesquite encroached watershed 8. The total evapotranspiration for watershed 7 for both study periods was comparable, while the wetter summer 2012 period produced notably less evapotranspiration for watershed 8. This may indicate that with the greater precipitation, the vegetation in watershed 7 is only capable of a certain amount of evapotranspiration. The additional water input in summer 2012 increases the soil moisture storage. The higher soil moisture leads to higher antecedent soil moisture and more runoff generation with the onset of a rainfall event. More runoff for both watersheds was observed and simulated in the wetter summer 2012 period, correlating with the higher soil moisture also simulated in the summer 2012 period. The observed soil moisture change for the summer 2012 period is lower, but this is accounted to the already high initial soil moisture values observed at the beginning of the summer 2012 study period. The change was calculated as the difference between the final and initial soil moisture value. The actual initial and final soil moisture values were higher for summer 2012 compared to summer 2011.

Complex relationships are present for the water budgets at both watersheds.

From the comparisons, the mesquite encroached watershed variables appear to be more sensitive to precipitation input. With greater precipitation, less evapotranspiration is produced and more runoff is generated. This may be attributed to the elevated soil moisture values with more precipitation input. The greater soil moisture has a larger impact on the runoff generation than evapotranspiration. Also, the larger bare soil fraction in the mesquite encroached watershed comes into play as less evapotranspiration is produced. For the mesquite treated watershed, greater precipitation input has less of an effect on the evapotranspiration. Soil moisture is elevated and leads to greater runoff generation. The antecedent soil moisture has a strong control on runoff generation.

CONCLUSIONS AND FUTURE WORK

Effective management strategies for semiarid ecosystems requires a more complete understanding of the vegetation shifts due to various factors, both natural and anthropogenic, such as overgrazing, increasing agricultural pressure, long-term climate change, increases in CO_2 and N deposition, and wildfires. One consequence of these factors is woody plant encroachment causing historical grasslands to shift to woody savannas. This thesis examines the encroachment of *Prosopis velutina*, or the velvet mesquite tree, at two small rangeland watersheds that are located in the Santa Rita Experimental Range in the Sonoran desert in southeast Arizona. Two watersheds, which are approximately the same area and close in proximity, are the focus of this study. One has undergone mesquite removal treatment while the other represents the ongoing landscape shift from grassland to woody savanna; therefore there is a unique opportunity to investigate the ecohydrological impacts of woody plant encroachment.

A dense environmental sensor network was installed at the mesquite encroached catchment in May 2011 to characterize the study basin. Seasonality of water and energy fluxes were measured and evaluated for this semiarid ecosystem. The majority of annual precipitation, approximately 55%, falls during the North American Monsoon (NAM) season (July to September). The summer periods saw more frequent soil moisture spikes, due to the greater number of events occurring. However, a deep soil moisture spike was observed during a long storm event in December, indicating that these systems are capable of groundwater recharge in the winter time. Sensible heat flux was dominant

throughout the year, with latent heat flux spiking after precipitation events. Net radiation was highest during the summer time and lowest during the winter time. Soil moisture and temperature sensors were also installed in transects across the mesquite encroached basin at three depths. During the NAM, grass and mesquite sites generally had greater soil moisture and lower temperatures, while bare soil areas had higher temperatures and lower soil moisture.

Historical rainfall and runoff data for both watersheds was analyzed to decipher patterns between rainfall amounts and intensities and runoff production. In the past decade, watershed 7, the catchment treated for mesquite, generally produced more total runoff volume and more runoff events. However, watershed 8, the catchment representing the mesquite encroachment, generated more runoff volume for very large precipitation events. These very large precipitation events typically occurred once or twice during an average NAM season. The change in runoff generation response indicates that the mesquite encroachment is triggering an ecohydrological threshold. The mesquite-treated watershed 7 generated 6 runoff events and 157.4 m^3 of total runoff in summer 2011, compared to the mesquite-encroached watershed 8 which generated 4 runoff events and 68.9 m^3 of total runoff. In summer 2012, the mesquite-treated watershed 7 generated 10 runoff events and 227.2 m^3 of total runoff while the mesquite-encroached watershed 8 which generated 5 runoff events and 105.6 m^3 of total runoff.

A more comprehensive approach is necessary to explore the ecohydrological dynamics that directly or indirectly affect runoff generation due to woody plant encroachment. A distributed hydrologic model was applied to both catchments.

Simulation periods were set to match observations during the NAM, specifically June 1, 2011 to September 30, 2011 (summer 2011) and June 1, 2012 to September 30, 2012 (summer 2012). The distributed models were forced with meteorological data from the eddy covariance tower and precipitation data from the 6 rain gauges installed at the site. The models were able to produce greater runoff totals and more runoff events at watershed 7 compared to watershed 8, similar to the trends that have been observed over the past decade. There was one very large precipitation event in the summer 2011 simulation period and one very large precipitation event in the summer 2012 period. The models were able to produce more runoff at watershed 8 for each of these single precipitation events. Again, this is analogous to what was observed at the watersheds for the past decade. The distributed hydrologic model outputs spatial variability of soil moisture, evapotranspiration, and energy fluxes. By analyzing these hydrologic variables, the mechanism leading to the precipitation threshold which results in a shift in total runoff production between the two watersheds, can be better understood. The watershed's sensitivity to vegetation was tested using three different vegetation scenarios: grass-only, mesquite-only, and bare-only. It was found that bare vegetation produced much less evapotranspiration and was more susceptible to infiltration-excess runoff generation. Mesquite vegetation has higher evapotranspiration rates compared to grass vegetation. By analyzing the ecohydrological controls on runoff generation, it is hypothesized that lower precipitation events rely on the antecedent soil moisture for runoff generation. Due to a more uniform cover and properties of grass cover, the mesquite-treated watershed generally has higher antecedent soil moisture, leading to

more runoff under moderate precipitation events. However, very large precipitation events generate more runoff at the mesquite-encroached watershed. It is hypothesized that the dominant variable for large precipitation events is the amount of bare soil present, and that the bare vegetated areas strongly contribute to runoff generation. A water budget analysis was also conducted in an attempt to quantify the hydrologic states during the NAM. Understanding the ecohydrological dynamics affecting the runoff generation will lead to a better understanding of woody plant encroachment implications on the hydrologic cycle at a catchment scale.

This study provides a better understanding of the ecohydrological mechanisms affecting runoff generation in these Sonoran desert semiarid rangelands. However, the results are specific to these catchments, which are at a fairly high elevation in the Sonoran desert. Additionally, the general consensus of the cause of woody plant encroachment at these sites is overgrazing. The causes of woody plant encroachment are system dependent, which may lead to different ecohydrological effects. Future work at the site may include developing dynamic vegetation maps to more accurately represent the actual vegetation patterns during storm and inter-storm periods. Antecedent soil moisture has a strong control on runoff generation and so a better vegetation representation for inter-storm periods may lead to more accurate soil moisture across the different vegetation. Additionally, the simulation periods can be expanded to evaluate ecohydrological dynamics over the entire year rather than just the NAM season. Winter precipitation may lead to increased soil storage, especially at the mesquite sites, which may play a role in runoff generation during the summer periods. More analysis of

intermediate levels of woody plant encroachment and its effect on runoff generation would also be valuable to explore. The precipitation volume threshold may be a consequence of the density of woody plant encroached shrubs. In addition, the landscape will keep evolving so a better understanding of the ecohydrological effects of different levels of woody plant encroachment will give a more comprehensive knowledge of the hydrologic effects that can be expected. Lastly, different precipitation events can be simulated and applied to both basin models to obtain a better understanding of what type of storm event will reach the runoff generation threshold. A certain volume of water or length of wetting time may contribute to the threshold where more runoff is generated at the mesquite-encroached site compared to the mesquite-treated site. The implications of this study may contribute to developing more effective management strategies for semiarid rangelands undergoing woody plant encroachment. In addition a better grasp of ecohydrological mechanisms effecting runoff generation is obtained.

REFERENCES

Abrahams, A.D., Parsons, A.J., Wainwright, J. 2003. Disposition of rainwater under creosotebush. Hydrological Processes 17: 2555-2566.

Adams, D.K., Comrie, A.C. 1997. The North American Monsoon. Bull. Amer. Meteor. Soc. 78: 2197–2213.

Archer, S. 1994. Woody plant encroachment into southwestern grasslands and savannas: rates, patterns and proximate causes. Ecological Implications of Livestock Herbivory in the West: 13-68.

Archer, S., Schimel D.S., Holland E.A. 1995. Mechanisms of shrubland expansion: land use, climate or CO_2. Climatic Change 29: 91-99.

Archer, S., Boutton, T.W., Hibbard, K.A. 2001. Trees in grasslands: biogeochemical consequences of woody plant expansion. Global Biogeochemical Cycles in the Climate System: 115-138.

Bednarz, S.T., Dybala, T., Muttiah, R.S., Rosenthal, W. 2001. Brush/water yield feasibility studies.

Breshears, D.D., Nyhan, J.W., Heil, C.E., Wilcox, B.P. 1998. Effects of woody plants on microclimate in a semiarid woodland: Soil temperature and evaporation in canopy and intercanopy patches. International Journal of Plant Sciences 159: 1010–1017.

Brown, J.R., and Archer, S.R. 1990. Water relations of a perennial grass and seedlings vs adult woody plants in a subtropical savanna, Texas. Oikos 57: 366-374.

Browning, D.M., Archer, S.R., Asner, G.P., McClaran, M.P., Wessman, C.A. 2008. Woody plants in grasslands: post-encroachment stand dynamics. Ecological Applications 18(4): 928-944.

Burba, G.G., and D.J. Anderson. 2010. A Brief Practical Guide to Eddy Covariance Flux Measurements: Principles and Workflow Examples for Scientific and Industrial Applications. LI-COR Biosciences, Lincoln, USA, 211 pp.

Burgess, T.L. 1995. Desert grassland, mixed shrub savanna, shrub steppe, or semidesert scrub? The dilemma of coexisting growth forms. The desert grasslands: 31-67.

Burrows, W.H., Carter, J.O., Scanlan J.C., Anderson E.R. 1990. Management of savannas for livestock production in north-east Australia – contrasts across the tree grass continuum. Journal of Biogeography 17: 503-512.

Cable, J.M., Barron-Gafford, G.A., Ogle, K., Pavao-Zuckerman, M., Scott, R.L., Williams, D.G., Huxman, T.E. 2012. Shrub encroachment alters sensitivity of soil respiration to temperature and moisture. Journal of Geophysical Research 117: G01001, doi:10.1029/2011JG001757.

Cavanaugh, M.L., Kurc, S.A., Scott, R.L. 2011. Evapotranspiration partitioning in semiarid shrubland ecosystems: a two-site evaluation of soil moisture control on transpiration. Ecohydrology 4(5): 671-681.

D'Odorico, P., Okin, G.S., Bestelmeyer, B.T. 2012. A synthetic review of feedbacks and drivers of shrub encroachment in arid grasslands. Ecohydrology 5: 520-530, doi:10.1002/eco.259.

Douglas, M.W., Maddox, R.A., Howard, K., Reyes, S., 1993. The Mexican monsoon. Journal of Climate 6: 1665-1677.

Dugas, W.A., Fritschen, L.J., Gay, L.W., Held, A.A., Matthias, A.D., Reicosky, D.C., Steduto, P., Steiner, J.L. 1991. Bowen ratio, eddy correlation, and portable chamber measurements of sensible and latent heat flux over irrigated spring wheat. Agric. For. Meteorol. 56: 1–20.

Duniway, M.C., Snyder, K.A., Herrick, J.E. 2010. Spatial and temporal patterns of water availability in a grass-shrub ecotone and implications for grassland recovery in arid environments. Ecohydrology 3: 55-67.

Dunne, T. 1978. Field studies of hillslope flow processes. Hillslope Hydrology: 227-293.

Eldridge, D.J., Bowker, M.A., Maestre, F.T., Roger, E., Reynolds, J.F., Whitford, W.G. 2011. Impacts of shrub encroachment on ecosystem structure and functioning: towards a global synthesis. Ecology Letters 14: 709-722.

Fensham, R.J. 1998. The influence of cattle grazing on tree mortality after drought in savanna woodland in noth Queensland. Australian Journal of Ecology 23: 414-428.

Gochis, D.J., Brito-Castillo, L., Shuttleworth, W.J., 2006. Hydroclimatology of the North American monsoon region in northwest Mexico. Journal of Hydrology 316: 53-70, doi:10.1016/j.jhydrol.2005.04.021.

Gosz, J.R. 1993. Ecosystem hierarchies. Ecological Applications 3: 369-376.

Gutiérrez-Jurado, H. A., Vivoni, E. R., Harrison, J. B. J., Guan, H. 2006. Ecohydrology of root zone water fluxes and soil development in complex semiarid rangelands. Hydrological Processes 20(15): 3289-3316, doi: 10.1002/hyp.6333.

Harrington, G.N. 1991. Effects of soil moisture on shrub seedling survival in a semi-arid grassland. Ecology 72: 1138-1149.

Huenneke, L.F., Clason, D., Muldavin, E. 2001. Spatial heterogeneity in Chihuahuan Desert vegetation: Implications for sampling methods in semiarid ecosystems. Journal of Arid Environments 47: 257-270.

Huenneke, L.F., Anderson, J.P., Remmenga, M., Schlesinger, W.H. 2002. Desertification alters patterns of aboveground net primary production in Chihuahuan ecosystems. Global Change Biology 8: 247-264.

Huenneke L.F., Schlesinger W.H. 2004. Patterns net primary production in chihuahan desert ecosystems. In Structure and Function of a Chihuahuan Desert Ecosystem: The Jornada Basin Long-Term Ecological Research Site, Havstad KM, Huenneke LF, Schlesinger WH (eds). Oxford University Press: Oxford; 232–246.

Huxman, T.E., Snyder, K.A., Tissue, D., Leffler, A.J., Ogle, K., Pockman, W.T., Sandquist, D.R., Potts, D.L., Schwinning, S. 2004. Precipitation pulses and carbon fluxes in semiarid and arid ecosystems. Oecologia 141: 254-268.

Huxman, T.E., Wilcox, B.P., Breshears, D.D., Scott, R.L., Snyder, K.A., Small, E.E., Hutline, K., Pockman, W.T., Jackson, R.B. 2005. Ecohydrological implications of woody plant encroachment. Ecology 86(2): 308-319.

International Organization of Standards (ISO 4359). 1983. Liquid flow measurement in open channels - Rectangular, trapezoidal, and U-shaped flumes. Reference number: ISO 4359-1983(E).

Ivanov, V.Y., Vivoni, E.R., Bras, R.L., Entekhabi, D. 2004a. Catchment hydrologic response with a fully distributed triangulated irregular network model, Water Resour. Res. 40(11): W11102, doi:10.1029/2004WR003218.

Ivanov, V.Y., Vivoni, E.R., Bras, R.L., Entekhabi, D. 2004b. Preserving high-resolution surface and rainfall data in operational-scale basin hydrology: a fully-distributed physically-based approach, Journal of Hydrology 298(1-4): 80-11.

Kemp, P.R. 1983. Phenological patterns of Chihuahuan Desert plants in relation to the timing of water availability. Journal of Ecology 71: 427-436.

Kurc S.A, Small E.E. 2004. Dynamics of evapotranspiration in semiarid grassland and shrubland ecosystems during the summer monsoon season, central New Mexico. Water Resources Research 40: W09305, doi:10.1029/2004WR003068.

Kurc S.A, Small E.E. 2007. Soil moisture variations and ecosystem-scale fluxes of water and carbon in semiarid grassland and shrubland. Water Resources Research 43: W06416, doi:10.1029/2006WR005011.

Laio, F., A Porporato, L. Ridolgi and I. Rodriguez-Iturbe. 2001. Plants in water-controlled ecosystems: active roles in hydrologic processes. Adv. Water Resources 24: 707-723.

Lemberg, B., Mjelde, J.W., Conner, J.R., Griffin, R.C., Rosenthal, W.D., Stuth, J.W. 2002. An interdisciplinary approach to valuing water from brush control. Journal of the American Water Resources Association 38: 409-422.

Mahmood, T.H, and E.R. Vivoni. 2011a. A climate-induced threshold in hydrologic response in a semiarid ponderosa pine hillslope. Water Resources Research 47: W09529, doi:10.1029/2011WR010384.

Moran, M.S., Scott, R.L., Keefer, T.O., Emmerich, W.E., Hernandez, M., Nearing, G.S., Paige, G.B., Cosh, M.H., O'Neill, P.E. 2009. Partioning evapotranspiration in semiarid grassland and shrubland ecosystmes using time series of soil surface temperature. Agricultural and Forest Meteorology 149: 59-72.

Mueller, E.N., Wainwright, J., Parsons A.J. 2007. Impact of connectivity on the modeling of overland flow within semiarid shrubland environments. Water Resources Research 43: W09412.

Nie, W., Yuan, Y., Kepner, W., Erickson, C., Jackson, M. 2012. Hydrological impacts of mesquite encroachment in the upper San Pedro watershed. Journal of Arid Environments 82: 147-155.

Oba, G., Post, E., Syvertsen, P.O., Stenseth, N.C. 2000. Bush cover and range condition assessments in relation to landscape and grazing in southern Ethiopia. Landscape Ecology, 15: 535-546.

O'Donnell, F.C. and K.K. Caylor. 2012. A model-based evaluation of woody plant encroachment effects on coupled carbon and water cycles. Journal of Geophysical Research 117: G02012, doi:10.1029/2011JG001899.

Ogle, K., and J.F. Reynolds. 2004. Plant responses to precipitation in desert ecosystems: integrating functional types, pulses, thresholds and delays. Oecologia 141: 282-294.

Potts, D.L., Scott, R.L., Bayram, S., Carbonara, J. 2010. Woody plants modulate the temporal dynamics of soil moisture in a semi-arid mesquite savanna. Ecohydrology 3: 20-27.

Roques, K.G., O'Connor, T.G., Watkinson, A.R. 2001. Dynamics of shrub encroachment in an African savanna: relative influences of fire, herbivory, rainfall and density dependence. Journal of Applied Ecology 38: 268-280.

Savage, M, and Swetnam, T.W. 1990. Early 19th century fire decline following sheep pasturing in a Navajo ponderosa pine forest. Ecology 71: 2374-2378.
Scholes, R.J., and Archer, S.R. 1997. Tree-grass interactions in savannas. Annual Review of Ecology and Systematics 28: 517-544.

Schwinning, S.; Sala, O.E.; Loik, M.E.; Ehleringer, J.R. 2004. Thresholds, memory, and seasonality:understanding pulse dynamics in arid/semiarid ecosystems. Oecologia 141(2): 191-193.

Scott, R.L., Edwards, E.A., Shuttleworth, W.J., Huxman, T.E., Watts, C.J., Goodrich, D.C. 2004. Interannual and seasonal variations in fluxes of water and carbon dioxide from a riparian woodland ecosystem. Agricultural and Forest Meteorology, 122: 64-84.

Scott, R.L., Huxman, T.E., Cable, W.L., Emmerich, W.E. 2006. Partitioning of evapotranspiration and its relation to carbon dioxide exchange in a Chihuahuan desert shrubland. Hydrol. Processes, 20: 3227-3243.

Scott, R.L., Jenerette, G.D., Potts, D.L., Huxman, T.E. 2009. Effects of seasonal drought on net carbon dioxide exchange from a woody-plant-encroached semiarid grassland. Journal of Geophysical Research 114: G04004, doi:10.1029/2008JG000900.

Scott, R.L. 2010. Using watershed water balance to evaluate the accuracy of eddy covariance evaporation measurements for three semiarid ecosystems. Agricultural and Forest Meteorology. 150: 219-225.

Seyfried, M. S., L. E. Grant, E. Du, and K. Humes. 2005. Dielectric Loss and Calibration of the Hydra Probe Soil Water Sensor. Vadose Zone Journal 4:1070-1079.

Turnbull, L., Wainwright, J., Brazier, R.E. 2009. Changes in hydrology and erosion over a transition from grassland to shrubland. Hydrological Processes, doi:10.1002/hyp.7491.

Van Auken, O.W. 2000. Shrub invasions of North American semiarid grasslands. Annual Review of Ecology and Systematics 31: 197-215.

Van Auken, O.W. 2009. Causes and consequences of woody plant encroachment into western North American grasslands. Journal of Environmental Management 90:2931-2942.

Vivoni, E.R., Entekhabi, D., Bras, R.L., Ivanov, V.Y. 2007. Controls on runoff generation and scale-dependence in a distributed hydrologic model, Hydrol. Earth Syst. Sci., 11(5), 1683– 1701.

Vivoni, E. R., Moreno, H.A., Mascaro, G., Rodrıguez, J.C., Watts, C.J., Garatuza-Payan, J., Scott, R. (2008b), Observed relation between evapotranspiration and soil moisture in the North American monsoon region, Geophys. Res. Lett., 35, L22403, doi:10.1029/2008GL036001.

Vivoni, E.R., Rodriguez, J.C., Watts, C.J. 2010. On the spatiotemporal variability of soil moisture and Evapotranspiration in a mountainous basin within the North American monsoon region. Water Resources Research 46: doi: 10.1029/2009WR008240

Watts, C.J., Scott, R.L., Garatuza-Payan, J, Rodrıguez, J.C., Prueger, J.H., Kustas, W.P., Douglas, M. 2007. Changes in vegetation condition and surface fluxes during NAME 2004. Journal of Climate 20(9): 1810 -1820

Webb, E.K., Pearman, G.I., Leuning, R. 1980. Correction of flux measurements for density effects due to heat and water vapor transfer. Quart. J. R. Meteorol. Soc. 106: 85-106.

Wilcox, B.P. 2002. Shrub control and streamflow on rangelands: a process-based viewpoint. Journal of Range Management 55: 318-326.

Wilcox, B.P. 2003. Runoff from rangelands: the role of shrubs. Shrub Management.

Wilcox, B.P., Thurow, T.L. 2006. Emerging issues in rangeland ecohydrology: vegetation change and the water cycle. Rangeland Ecology and Management 59: 220-224.

Wilczak, J.M., Oncley, S.P., Stage, S.A. 2001. Sonic anemometer tilt correction algorithms. Bound-Lay. Meteorol. 99: 127-150

APPENDIX A

SAMPLING SENSORS

A.1. Watershed Sensor Network Locations

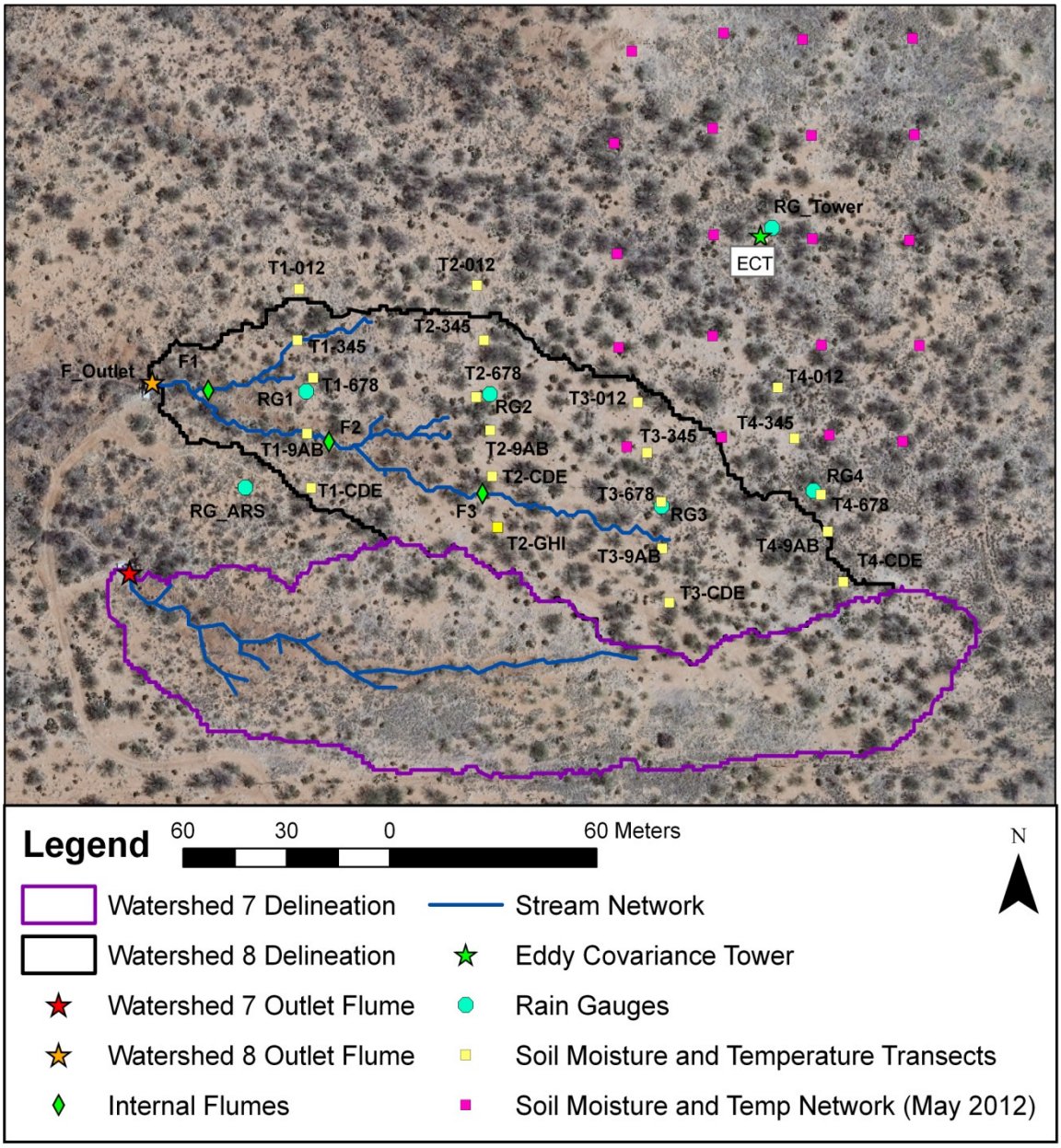

A.2. Mini-flume Dimensions

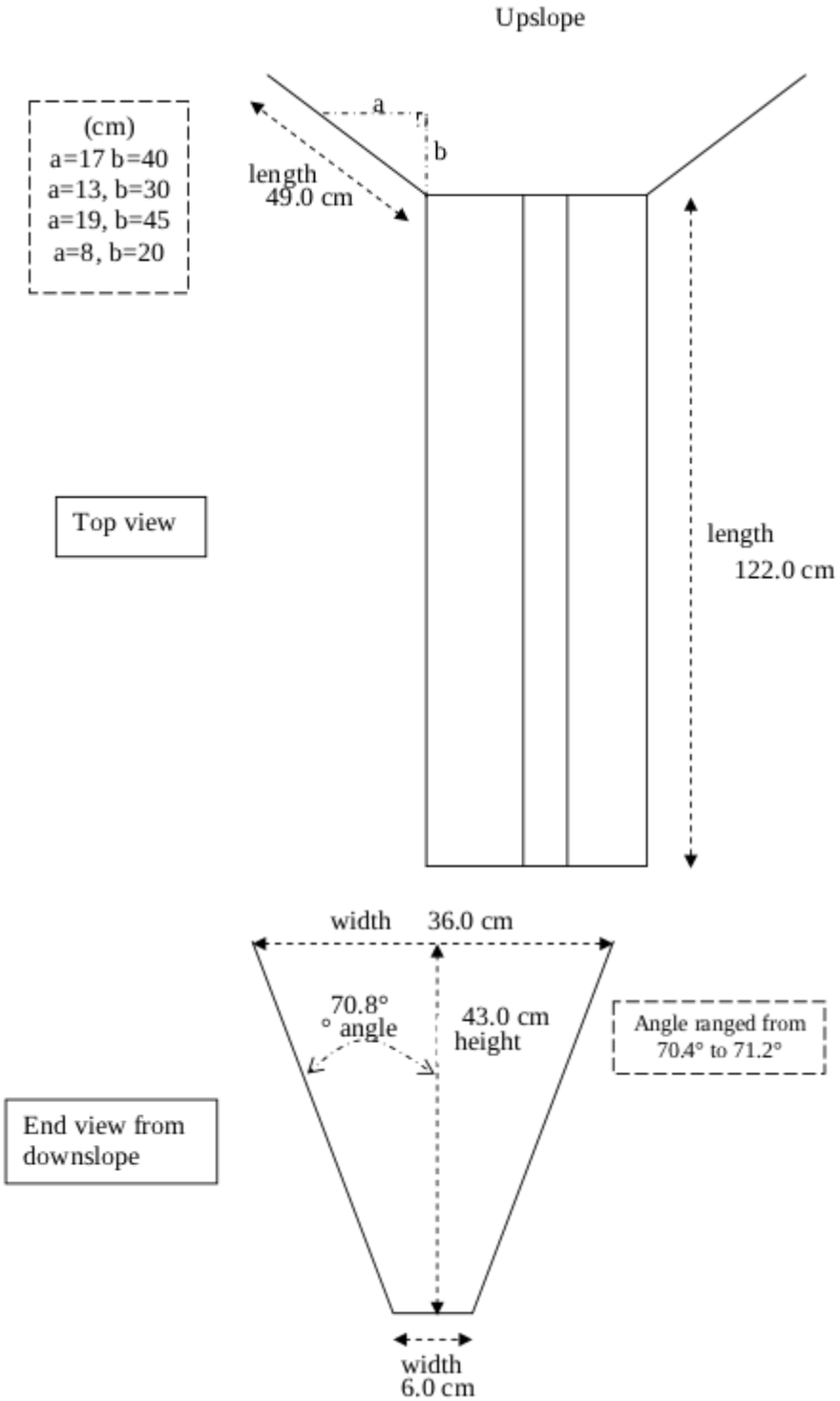

APPENDIX B

SENSOR CALIBRATIONS AND CORRECTIONS

B.1. Soil Moisture Sensor Corrections

Two different types of soil moisture sensors are used at the watershed site, the Hydra probe (HP) and the CS616. Each soil moisture sensor is set with a default factory calibration. This default calibration is generally for a generic soil type, such as loam. To obtain accurate soil moisture readings, soil moisture sensor corrections were performed for the two different types of probes using actual soil from the field site. Using the site soil, an experiment was set up to determine the actual soil moisture through gravimetric analysis and compare it to the soil moisture probe readings. The experimental procedure is described below.

Required Equipment:

1) Cylindrical sampling devices
2) Scale to weigh samples
3) Oven to dry samples
4) Datalogger programmed to measure volumetric water content for each probe
5) CS616 probe
6) Hydra probe
7) 18 buckets: 9 for the CS616 (diameter = 18 to 20 inches) and 9 for the Hydra probe (diameter = 8 inches). The number of buckets actually used may be variable depending on how much soil is available for analysis.

Procedure:

1) In the field, the sensors are placed at depths varying from 5 to 30 cm. Obtain soil from the field from just below the surface (about 5 cm depth) up to a 30 cm depth. Mix the soil well.
2) Mark each bucket at a 10 cm height.
3) Measure the volume of the two types of buckets up to the 10 cm height. To measure the volume most accurately, add water to a height of 10 cm and then measure the amount of water in the bucket with a graduated cylinder.
4) Sieve the soil from the site using a sieve number 4 (4.75 mm openings). This will leave soil that is composed of sand, silt, and clay, and a few larger particles. The larger opening is chosen so to maintain as close as possible field conditions without affecting the experiment.

5) Pack each bucket with the sieved soil to the 10 cm mark. Continue to mix the soil well and keep each bucket as similar to one another as possible. Each bucket should be packed as uniformly as possible in bulk density with dry soil.

6) Choose one CS616 bucket and bury the CS616 probe at approximately a 5 cm depth. Choose one HP bucket and bury the Hydra probe at approximately a 5 cm depth.

7) Identical amounts of water can now be added to the top of each bucket. Add 1 liter of water to each bucket, and then add 500 ml as necessary. Attempt to achieve full saturation. Extra water may be on top of the soil and this is alright.

8) The buckets must be allowed to equilibrate. Cover the buckets for a 24 hour period to prevent evaporation and allow equilibration to be achieved.

9) Uncover the buckets and allow evaporation to occur.

10) Samples may begin to be taken once there is no water ponding on the surface. Take samples as deemed necessary from the estimate porosity value (~0.4 wfv) to almost dry (~0.0 wfv). Water fraction by volume (wfv) is a dimensionless quantity that signifies the percentage of water in the soil displayed in decimal form. It is equivalent to units of (m^3/m^3). Eight sampling points can be measured since there are eight buckets without a sensor, and should be taken so that a broad range of soil moisture points are represented. An example of readings to take samples at would be (in [wfv]): 0.38, 0.33, 0.28, 0.23, 0.18, 0.13, 0.08, and 0.03. The soil moisture readings are taken from the ninth bucket that contains the soil moisture sensor (HP or CS616). The readings are read from the datalogger.

11) Determine the volume of each cylindrical sampling device and record as $Vol_{cylinder}$. Also determine the weight of each cylindrical sampling device and record as $M_{Container}$.

12) Take samples of the soil using the cylindrical sampling devices. Sample cylinders should be pushed evenly into the soil at a depth of approximately 5 cm, to match the probe measurement depth as closely as possible. Remove the container and gently trim the ends of excess soil. Remove excess soil from outside the container. As soon as the sample is taken, record the soil moisture reading from the probe, which is read from the datalogger.

13) Weigh and record the wet soil weight ($M_{Wet+Container}$)

14) Dry the sample in the oven for 24 hours. The oven needs to be at 105 degrees Celsius.

15) Weigh and record the dry soil weight ($M_{Dry+Container}$)

16) Volumetric water content, θ_V, can now be calculated using the following measurements and equations.

    a. Measurements:

        i. Mass of dry soil (M_{Dry}) = $M_{Dry+Container}$ - $M_{Container}$

        ii. Mass of wet soil (M_{Wet}) = $M_{Wet+Container}$ - $M_{Container}$

        iii. Mass of container ($M_{Container}$)

        iv. Volume of cylinder ($Vol_{Cylinder}$)

    b. Equations

        Bulk density: $\rho_b = \frac{M_{Dry}}{Vol_{Container}}$

        Gravimetric water content: $\theta_g = \frac{M_{Wet} - M_{Dry}}{M_{Dry}}$

        Volumetric water content: $\theta_v = \theta_g \times \rho_b$

17) To find the correction equation, the measured volumetric water content calculated using the equations in step 16 is plotted against the volumetric water content that was read from the soil moisture sensor. A relationship between actual measured and calculated water content as determined from the probes can be determined.

Using the above procedure, correction equations were determined for each sensor, the Hydra probe and the CS616, and applied to obtain numerically correct soil moisture values for the actual soil at the field site. For the Hydra probe, a power relationship is used and is shown below. The data is plotted in the figure below. The high R^2 values indicate a good fit.

$$Soil\ Moisture_{Corrected} = \left(\frac{HydraProbeReading}{0.7983}\right)^{1.27845}$$

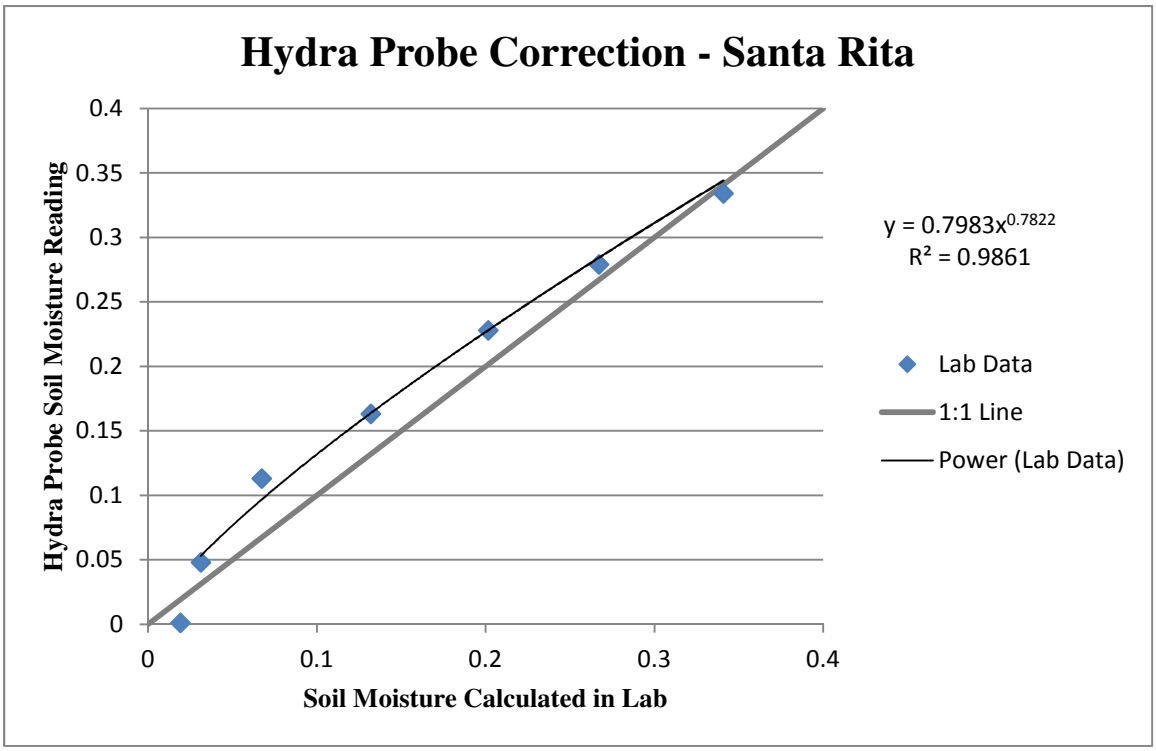

For the CS616, a logarithmic relationship best fit the data and is shown below. The data is plotted in the next figure.

$$Soil\ Moisture_{Corrected} = 0.1944 * \ln(CS616\ Reading) + 0.5749$$

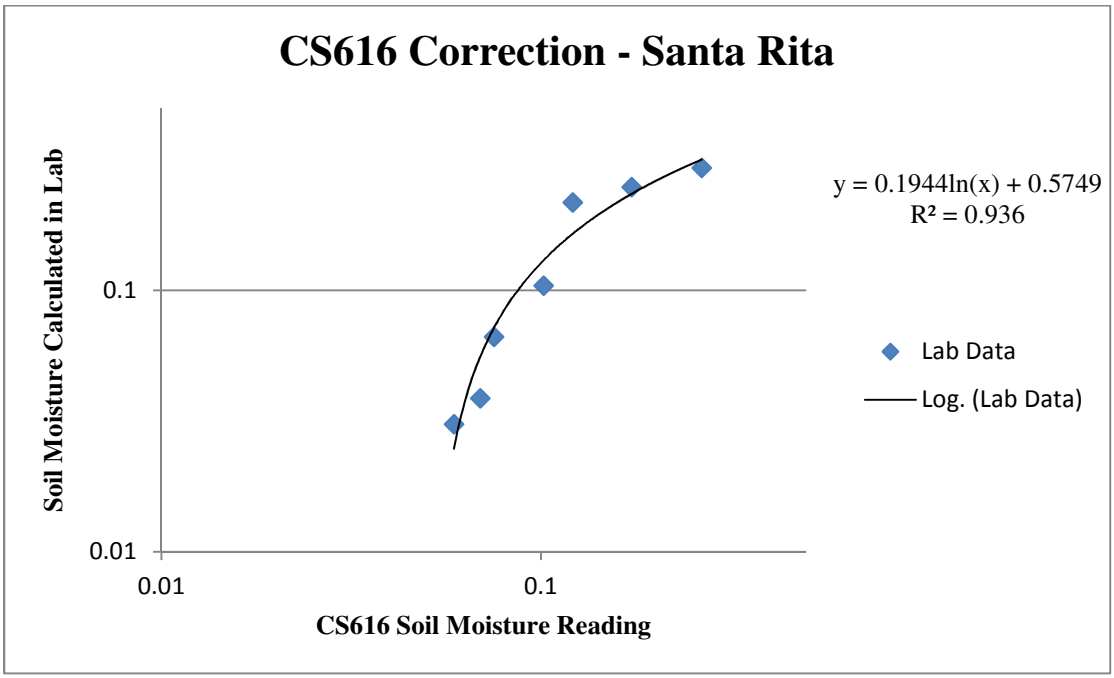

Again, the high R^2 values indicate a good fit. These corrections are applied to each soil moisture value that is measure in the field. This allows a more accurate soil moisture value as related to the actual soil texture type, compared to the factory default setting.

B.2. Flume Calibration Curves and Discharge Calculation Curves

Flume calibration curves are necessary to develop appropriate pressure transducer readings (psi) and head relationships for each mini-flume at the watershed site. At each mini-flume, a small cross-section of the flume was isolated. Water was then filled to the top of the flume within the cross-section. An initial pressure reading was taken, with the pressure transducer, as well as the height that was represented in the flume, measured using a ruler. Water was slowly removed and as the level in the flume dropped, more pressure and height readings were taken. A representative range of water heights in the flume were read with their corresponding pressure measurements. These readings were used to develop a linear relationship between the pressure transducer readings and the actual height in the mini-flumes. The resulting linear equations developed for each mini-flume are summarized in the table below.

Flume 1[a]	Height [cm] = 64.795 * (PSI) + 16.5
Flume 1[b]	Height [cm] = 69.149 * (PSI) – 4.5757
Flume 2	Height [cm] = 75.582 * (PSI) - 4.2383
Flume 3	Height [cm] = 70.860 * (PSI) - 4.3107

The calibrations for flumes 2 and 3 are valid for the entire study period presented in this thesis. Unfortunately, the pressure transducer at flume 1 needed to undergo repair from early May 2012 through August 22, 2012. The repaired pressure transducer needed a new calibration curve relating the pressure readings (psi) to height in the flume (cm). Flume 1^a calibration is valid for data from May 2011 through May 2012. Flume 1^b calibration is valid for data from August 22, 2012 to present time.

After the heights in each mini-flume are determined, a relationship between the head in the flume and the flow rate in the flume was determined for each mini-flume. These relationships were developed using the ISO 4359 method, which was developed for liquid flow measurements in open channels using a rectangular, trapezoidal, or U-shaped flumes. The dimensions of the trapezoidal mini-flumes were used along with the heads as determined from the pressure-height relationships. The ISO 4359 method is summarized below.

Variables:

A = Cross-sectional area of approach channel [m^2]

b = Bottom width of flume throat [m]
B = Bottom width of approach channel [m]
C = Parshall flume constant [empirical units]
C_d = Coefficient of discharge for trapezoidal flumes [unit-less]
C_s = Shape coefficient for trapezoidal flume [unit-less]
C_v = Coefficient of approach velocity for trapezoidal flumes [unit-less]
F = Froude number of flow in approach channel [unit-less]
g = Acceleration due to gravity, 9.8066 m/s^2.
h = Measured head [m]. If there is a hump, then it is the vertical distance between the top of the hump and the water surface.
H = Total head [m]. Measured head plus velocity head. $H = h * C_v^{2/3}$
k = Constant used in trapezoidal flume computation [unit-less]
L = Length of flume throat [m]
m = Side slope of trapezoidal flume throat. Horizontal to vertical (H:V)
M = Side slope of trapezoidal flume approach channel. Horizontal to vertical (H:V)
n=Parshall flume power constant [unit-less]
P=Hump height [m]
Q=Flow rate through flume [m^3/s]
T=Top width of approach channel [m]
V=Velocity in approach channel [m/s]

Equations:

$$k = \sqrt{1 + m^2} - m$$

$$C_d = \left(1 - \frac{0.006\,kL}{b}\right)\left(1 - \frac{0.003L}{h}\right)^{3/2}$$

$$T = B + 2M(P + h)$$

$$A = (P + h)[B + M(P + h)]$$

Procedure:

1) Let H = h and obtain C_s from the graph below.

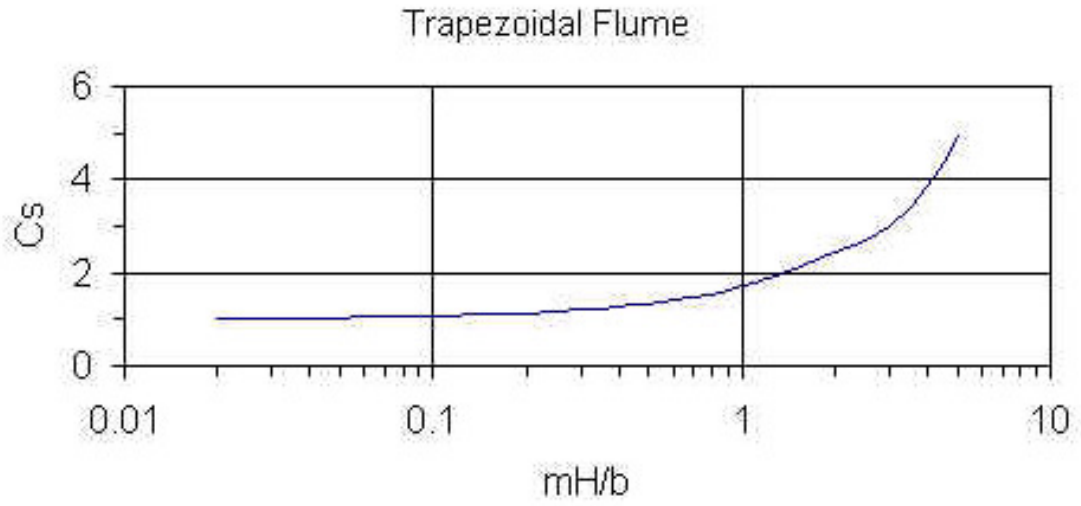

2) Calculate C_v from numerical solution of the equation below.

$$\sqrt{C_v^{2/3}-1} = \frac{2}{3\sqrt{3}}\frac{bhC_vC_s}{A}$$

3) Calculate flow rate, Q, velocity, V, and Froude number, F, using the equations below.

$$Q = bC_dC_sC_v\left(\frac{2h}{3}\right)^{3/2}\sqrt{g}$$

$$V = \frac{Q}{A} \qquad F = V\sqrt{\frac{T}{gA}}$$

4) Since Cs and Cv are functions of both H and h, re-compute H ($H = h * C_v^{2/3}$), C_s, C_v, and Q. Re-compute Q until there are at least four significant digis of accuracy.

Using this method, three power relationships between height and flow rate were developed for each mini-flume. These three relationships are summarized in the table below.

Flume 1	Q [ft^3/sec] = 0.0024 * (Height [cm])$^{1.7654}$
Flume 2	Q [ft^3/sec] = 0.0024 * (Height [cm])$^{1.7648}$
Flume 3	Q [ft^3/sec] = 0.0013 * (Height [cm])$^{2.1392}$

These two relationships enable one to calculate the flow rate for each mini-flume at the site given the pressure transducer reading.

APPENDIX C

NETWORK MAINTENANCE

The following guides are presented to detail the field tasks necessary to collect data at the site and maintain the instrument network.

C.1. Monthly Maintenance and Field Tasks

The field site should be visited every 28 days. After 28 days, the storage capacity on the transect dataloggers and the data card at the tower will be full and data for each additional day will overwrite a previous day. Frequent visits are also encouraged to help verify that all instruments are working and that there is a research presence at the site.

1) Collect Data

    a. At four dataloggers (soil moisture transects) using USB-Computer connection. Once the computer is connected, use Loggernet to connect to the appropriate datalogger. Verify with the Public tab that all sensors are running. If sensor reads a NaN value, it is not working. If a sensor is not working, the cables should be checked for damage and the connection to the data logger should be examined. Download the 30 minute average tables stored on the datalogger using the data collection tab within Loggernet.

    b. At the tower by taking out the data card and using CompactFlash to PC Card adapter. Make sure to use the keyboard display on the datalogger and go to the PcCard menu, move the cursor to "Remove Card" and press Enter. The status will show "You may now remove the card." Remove the card. Insert into PC and then copy data files to another drive just as one would from any other disk. Meanwhile, connect to the datalogger using the USB-Computer connection with Loggernet. Similarly to the soil moisture transect dataloggers, verify with the public tab that all sensors are running. Next, download the 30 minute average tables stored on the datalogger using the data collection tab within Loggernet.

    c. Reload each datalogger program after all data has been collected.

2) Clean out sediment and debris from rain gauges.

3) Double check the all soil moisture sensors and heat flux plates haven't been tampered with or unburied due to wildlife or significant runoff events.

4) Clean sediment, dirt, etc. from mini-flumes. Rinse the flumes out with water.

5) Fill the stills at each mini-flume with water.

6) Clean out the mini-flume stills and ensure that nothing is obstructing the pressure transducers.

7) Visually inspect the pressure transducers and check the indicating desiccant or enclosure humidity indicator.

8) Check the battery condition at the tower and each transect. Ensure that an appropriate voltage is being maintained.

9) Clean off the tower equipment. This includes: Apogee, Relative Humidity/Temperature Probe, Pyranometer, Radiometer, Sonic Anemometer, and Infrared Gas Analyzer.

10) Ensure the tower equipment is level. This includes: Pyranometer, Radiometer, and the Sonic Anemometer.

C.2. Individual Instrument Maintenance

This guide is provided as a reference to service the field instruments appropriately over a longer time period to maintain an operating condition that provides reliable data. The field instruments are listed with a description of their individual requirements.

- TE525MM (Rain Gauge): 9.6 inch collector, 0.1 mm tip. Located at the transects.

  TE525 (Rain Gauge): 6 inch collector, 0.254 mm tip. Located at the tower. This sensor is factory calibrated. The following calibration check is advised every 12 months:

  a. Use a metal can that will hold at least one quart of water.

  b. Punch a very small hole in the bottom of the can.

  c. Place the can in the top funnel of the rain gauge and pour 16 fluid ounces (1 pint) of water into the can.

  d. If it takes less than 45 minutes for the water to run out, the hole in the can is too large.

  e. The following number of tips should occur: 100 +/- 3

  f. Adjusting screws are located on the bottom of the rain gauge adjacent to the large center drain hole. Adjust both screws the same number of turns. Clockwise rotation increases the number of tips per volume of water, while counter clockwise rotation decreases the number of tips. One half turn of both screws causes a 2% to 3% change.

  g. Check and re-level the rain gauge lid.

- CS450 (Pressure Transducer)

This sensor is recommended to be factory recalibrated and checked every two to three years. The desiccant in the tube changes color from blue to pink when it is no longer able to keep the vent tube dry. Pink desiccant needs to be replaced.

- SI-111 (Apogee)

  Every few months, gently clean the lens with a moistened cotton swab. It is important to keep the lens and view clean. Distilled water or alcohol works well for most dust/dirt.

- CMP3 (Pyranometer)

  Recalibration every 2 years is recommended. The sensor should be returned to the manufacturer or a calibration lab with facilities to calibrate radiation sensors.
- CNR2 (Long and Short Wave Radiometer)

  Recalibration every 2 years is recommended. The sensor should be returned to the manufacturer or a calibration lab with facilities to calibrate radiation sensors.
- LI-7500 (IRGA, Open Path Infrared Gas Analyzer)

  The CO_2 flux readings should be examined every year to determine if they are drifting from expected values. If they are drifting, recalibration of the sensor is recommended.

APPENDIX D

SOIL CHARACTERIZATION

D.1. Lab Soil Characterization

Upon installation of the soil moisture sensors, soil samples were taken at each location at each depth. These samples were used to determine soil texture at the experimental site. Five locations at three different depths were randomly chosen within the watershed to sample. The following table indicates the particle size classifications which were used with the appropriate sieve to determine percentages of each particle type within the soil sample. The experimental procedure followed is described below.

Particle Type	Particle Size
Sand	0.05 mm to 2 mm
Silt	0.002 mm to 0.05 mm
Clay	< 0.002 mm

Required Equipment:

1) Three soil sampling containers
2) Scale to weight samples
3) Three sieves with the following specifications:
    a. 2 mm opening screen
    b. 0.05 mm opening screen
    c. 0.002 mm opening screen

Procedure:

1) Obtain a sample and clearly label the location and depth.
2) Weigh three soil sampling containers and record. Label one container as "Soil+Silt+Clay," another container as "Silt+Clay," and the last container as "Clay."
3) Sift the sample so that all rocks and larger particles are removed using the sieve with a 2 mm opening screen. The remaining material should only contain particles that are less than 2 mm in size. Place/Sieve the material into the soil sampling container labeled "Soil+Silt+Clay". Weigh and record.
4) Place the "Soil+Silt+Clay" material into the sieve with a 0.05 mm opening screen, and sieve the material into the container labeled "Silt+Clay." Weigh and record.
5) Place the "Silt+Clay" material into the sieve with a 0.002 mm opening screen, and sieve the material into the container labeled "Clay." Weigh and record.

6) The percentages of sand, silt, and clay are determined using the following equations:

    a. Mass of Clay = Mass of "Clay" Container with Sample – Mass of Empty "Clay" Container

    b. Mass of Silt = Mass of "Silt+Clay" Container with Sample – Mass of Empty "Silt+Clay" Container – Mass of Clay

    c. Mass of Sand = Mass of "Sand+Silt+Clay" Container with Sample – Mass of Empty "Sand+Silt+Clay" Container – Mass of Clay – Mass of Silt

    d. Total Mass = Mass of "Sand+Silt+Clay" Container with Sample – Mass of Empty "Sand+Silt+Clay" Container

    e. $\text{Percent of Clay (\%)} = \frac{\text{Mass of Clay (g)}}{\text{Total Mass (g)}}$

    f. $\text{Percent of Silt (\%)} = \frac{\text{Mass of Silt (g)}}{\text{Total Mass (g)}}$

    g. $\text{Percent of Sand (\%)} = \frac{\text{Mass of Sand (g)}}{\text{Total Mass (g)}}$

7) The soil texture is determined using the sand, silt, and clay percentages with the USDA soil texture triangle, shown in the figure below, which has classified soil into twelve major soil texture classifications.

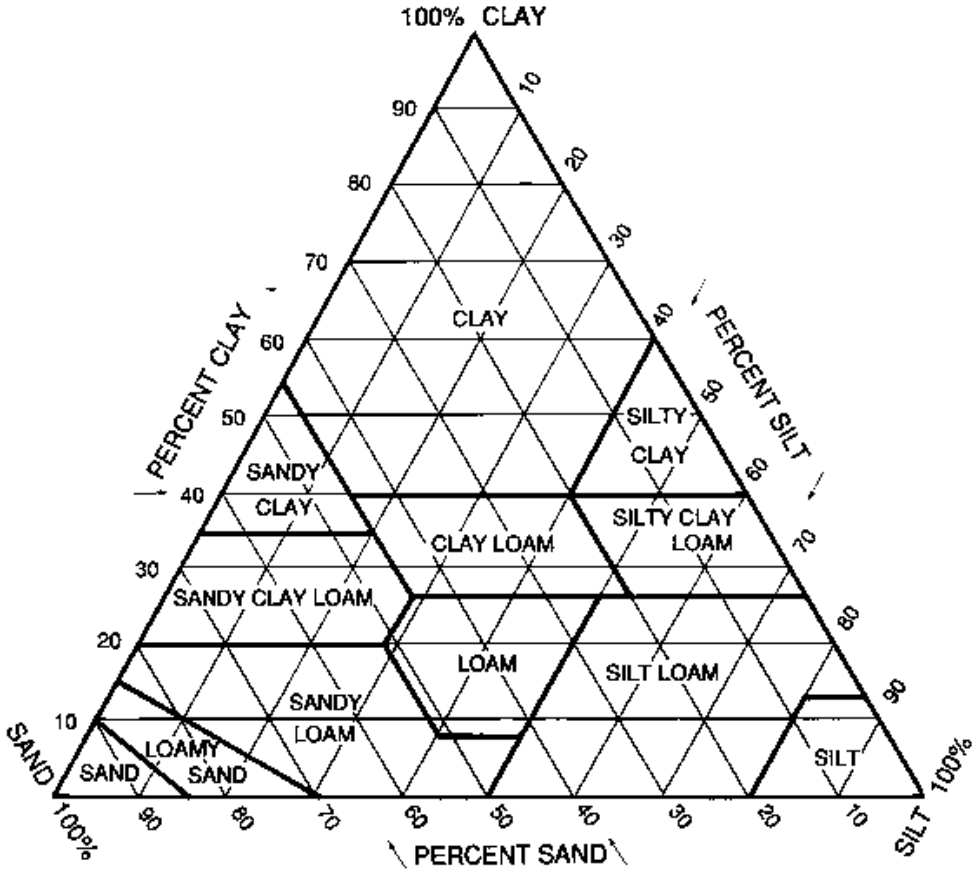

The results of the soil texture analysis, averaged at the five different sites at the study site, gave a soil texture of sandy loam, with the average sand, silt, and clay percentages summarized in the table below.

Averages	Sand %	Silt %	Clay %
5 cm	64.55857	24.79811	10.64332
15 cm	70.73742	20.80347	8.459109
30 cm	75.63174	17.74207	6.62619

Sandy loam matches with what has been reported in other studies at the site (Polyakov et al., 2010). SSURGO classifies the site as Continental Sandy Loam, with approximately 66.0% sand, 23.0% silt, and 11.0% clay. Our calculations are summarized on the next page. We obtained the same soil classification; however saw slightly lower clay percentages and slightly higher sand percentages. We believe this difference is due to our experimental procedure and the difficulty of sifting clay by hand. A more accurate soil texture analysis would most likely be obtained if a mechanical sieve shaker were used instead.

Location/ Sensor ID	Depth (cm)	**Sand+Silt+Clay and Container(g)**	**Silt+Clay and Container(g)**	**Clay and Container(g)**	**Sand+Silt+Clay (g)**	**Silt+Clay (g)**	**Clay (g)**	Sand Weight (g)	Silt Weight (g)	Clay Weight (g)	**Sand %**	**Silt %**	**Clay %**
Transect 1 - 6	5 cm	139.66	72.614	34.265	118.648	51.723	13.463	66.925	38.26	13.463	56.40634	32.24665	11.34701
Transect 1 - 7	15 cm	129.002	57.776	31.179	107.99	36.885	10.377	71.105	26.508	10.377	65.84406	24.54672	9.60922
Transect 1 - 8	30 cm	131.273	43.657	28.035	110.261	22.766	7.233	87.495	15.533	7.233	79.35263	14.08748	6.55989
Transect 2 - g	5 cm	143.156	74.566	38.145	122.144	53.675	17.343	68.469	36.332	17.343	56.0560	29.7452	14.1988
Transect 2 - h	15 cm	141.242	60.579	31.842	120.23	39.688	11.04	80.542	28.648	11.04	66.9899	23.8277	9.1824
Transect 2 - i	30 cm	138.12	59.439	30.124	117.108	38.548	9.322	78.56	29.226	9.322	67.0834	24.9565	7.9602
Transect 3 - 0	5 cm	122.541	53.069	31.723	101.529	32.178	10.921	69.351	21.257	10.921	68.3066	20.9369	10.7565
Transect 3 - 1	15 cm	127.658	52.692	29.862	106.646	31.801	9.06	74.845	22.741	9.06	70.1808	21.3238	8.4954
Transect 3 - 2	30 cm	122.028	46.86	27.436	101.016	25.969	6.634	75.047	19.335	6.634	74.2922	19.1405	6.5673
Transect 4 - 9	5 cm	115.858	50.321	28.404	94.846	29.43	7.602	65.416	21.828	7.602	68.9708	23.0141	8.0151
Transect 4 - a	15 cm	137.884	53.614	30.098	116.872	32.723	9.296	84.149	23.427	9.296	72.0010	20.0450	7.9540
Transect 4 - b	30 cm	136.741	50.436	28.372	115.729	29.545	7.57	86.184	21.975	7.57	74.4705	18.9883	6.5411
Tower	5 cm	139.72	52.879	31.366	118.708	31.988	10.564	86.72	21.424	10.564	73.0532	18.0476	8.8991
Tower	15 cm	117.319	41.432	27.596	96.307	20.541	6.794	75.766	13.747	6.794	78.6713	14.2741	7.0545
Tower	30 cm	136.851	40.63	27.176	115.839	19.739	6.374	96.1	13.365	6.374	82.9600	11.5376	5.5025
Tower	50 cm	112.069	44.729	34.955	91.057	23.838	14.153	67.219	9.685	14.153	73.8208	10.6362	15.5430
Tower	75 cm	125.532	40.556	27.01	104.52	19.665	6.208	84.855	13.457	6.208	81.1854	12.8750	5.9395
Tower	100 cm	136.753	56.746	32.555	115.741	35.855	11.753	79.886	24.102	11.753	69.0213	20.8241	10.1546

Container ID	Container Weight (g)	Container Purpose
Sd	21.012	Sand+Silt+Clay
St	20.891	Silt+Clay
C (Orange Label)	20.802	Clay

Averages	**Sand %**	**Silt %**	**Clay %**
5 cm	**64.5586**	**24.7981**	**10.6433**
15 cm	**70.7374**	**20.8035**	**8.4591**
30 cm	**75.6317**	**17.7421**	**6.6262**

APPENDIX E

FIELD DATALOGGER PROGRAMS

E.1. Santa Rita Eddy Covariance Tower Datalogger – CR5000

```
'CR5000 Series Datalogger
'To create a different opening program template, type in new
'instructions and select Template | Save as Default Template
'date: June 23 2008
'program author: Luis Mendez-Barroso and Ryan Templeton
'Edited: Nolie Pierini (Last Edit: July 20, 2011)
'Declare Public Variables

Public Batt_Volt
Public VW
Public PA_uS
Public VW_2
Public PA_uS_2
Public VW_3
Public PA_uS_3
Public VW_4
Public PA_uS_4
Public VW_5
Public PA_uS_5
Public VW_6
Public PA_uS_6
Public AirTC
Public RH
Public Rain_mm
Public PTemp_C
Public Temp_C
Public Temp_C_2
Public Temp_C_3
Public Temp_C_4
Public Solar_Wm2
Public Solar_kJ
Public shf
Public shf_cal
Public shf_2
Public shf_cal_2
Public BP_mbar
Public Net_shortwave
Public Net_longwave
'===Soil heatflux calibration variables
Public shf_mV
Public shf_mV_run
Public shf_mV_0
```

```
Public shf_mV_180
Public shf_mV_360
Public V_Rf
Public V_Rf_run
Public V_Rf_180
Public V_Rf_360
Public shf_cal_on               'HFP01SC calibration flag.
Public shf_2_mV
Public shf_2_mV_run
Public shf_2_mV_0
Public shf_2_mV_180
Public shf_2_mV_360
Public V_Rf_2
Public V_Rf_2_run
Public V_Rf_2_180
Public V_Rf_2_360
Public shf_cal_2_on 'HFP01SC calibration flag.
Public wind(5)          'Wind, sonic temperature, and diagnostic data from CSAT3.
Alias wind(1) = Ux
Alias wind(2) = Uy
Alias wind(3) = Uz
Alias wind(4) = Ts
Alias wind(5) = diag_csat
Units wind = m/s
Units Ts = degC
Units diag_csat = unitless

'Declare variables for the Apogee surface temperature probe
Dim TT_K_6
Dim SBT_K_7
Dim m_8
Dim b_9
Public BattV
Public TT_C
Public SBT_C
Public TTmV
Public diag_bits(9)                 'Warning flags.
Alias diag_bits(1) = del_T_f          'Delta temperature warning flag.
Alias diag_bits(2) = track_f          'Tracking (signal lock) warning flag.
Alias diag_bits(3) = amp_h_f          'Amplitude warning high flag.
Alias diag_bits(4) = amp_l_f          'Amplitude low warning flag.
Alias diag_bits(5) = chopper_f                'Chopper warning flag.
Alias diag_bits(6) = detector_f               'Detector warning flag.
Alias diag_bits(7) = pll_f            'PLL warning flag.
```

```
Alias diag_bits(8) = sync_f          'Synchronization warning flag.
Alias diag_bits(9) = agc             'Automatic gain control.
Units diag_bits = unitless

'CS7500 has a fixed delay of 302.369 mSec (six scans at 20 Hz or three scans at 10 Hz).
Public irga(4)                       'Co2, h2o, and pressure from the CS7500 (LI-7500).
Alias irga(1) = co2
Alias irga(2) = h2o
Alias irga(3) = press
Alias irga(4) = diag_irga
Units co2 = mg/(m^3)
Units h2o = g/(m^3)
Units press = kPa

'Analog variables with three or six  delay.
Public fw                            'Fine wire thermocouple temperature.
Units fw = degC
Public tc_ref                        'Thermocouple reference temperature.
Units tc_ref = degC

'Flux variables.
Public Fc                            'CO2 flux.
Public LE                            'Latent heat flux from CS7500 (LI-7500).
Public Hs                            'Sensible heat flux using sonic temperature.
Public H                             'Sensible heat flux using finewire thermocouple.
Public tau                           'Momentum flux.
Public u_star                        'Friction velocity.
Public cov_out_1(32)                 'Covariances of wind and scalars + windspeed.
Units Fc = mg/(m^2 s)
Units LE = W/m^2
Units Hs = W/m^2
Units H = W/m^2
Units tau = kg*m/s^2
Units u_star = m/s

'Aliases for covariances.
Alias cov_out_1(1) = Uz_Uz_1
Alias cov_out_1(2) = Uz_Ux_1
Alias cov_out_1(3) = Uz_Uy_1
Alias cov_out_1(4) = Uz_co2_1
Alias cov_out_1(5) = Uz_h2o_1
Alias cov_out_1(6) = Uz_Ts_1
Alias cov_out_1(7) = Uz_fw_1
Alias cov_out_1(8) = Ux_Ux_1
```

```
Alias cov_out_1(9) = Ux_Uy_1
Alias cov_out_1(10) = Ux_co2_1
Alias cov_out_1(11) = Ux_h2o_1
Alias cov_out_1(12) = Ux_Ts_1
Alias cov_out_1(13) = Ux_fw_1
Alias cov_out_1(14) = Uy_Uy_1
Alias cov_out_1(15) = Uy_co2_1
Alias cov_out_1(16) = Uy_h2o_1
Alias cov_out_1(17) = Uy_Ts_1
Alias cov_out_1(18) = Uy_fw_1
Alias cov_out_1(19) = co2_co2_1
Alias cov_out_1(23) = h2o_h2o_1
Alias cov_out_1(26) = Ts_Ts_1
Alias cov_out_1(28) = fw_fw_1
Alias cov_out_1(31) = wnd_dir_compass
Units wnd_dir_compass = degrees

'Alternate Flux variables using running mean.
Public cov_out_2(22)
'Aliases for alternative covariances.
Alias cov_out_2(1) = Uz_Uz_2
Alias cov_out_2(2) = Uz_Ux_2
Alias cov_out_2(3) = Uz_Uy_2
Alias cov_out_2(4) = Uz_co2_2
Alias cov_out_2(5) = Uz_h2o_2
Alias cov_out_2(6) = Uz_Ts_2
Alias cov_out_2(7) = Uz_fw_2
Alias cov_out_2(8) = Ux_Ux_2
Alias cov_out_2(9) = Ux_Uy_2
Alias cov_out_2(10) = Ux_co2_2
Alias cov_out_2(11) = Ux_h2o_2
Alias cov_out_2(12) = Ux_Ts_2
Alias cov_out_2(13) = Ux_fw_2
Alias cov_out_2(14) = Uy_Uy_2
Alias cov_out_2(15) = Uy_co2_2
Alias cov_out_2(16) = Uy_h2o_2
Alias cov_out_2(17) = Uy_Ts_2
Alias cov_out_2(18) = Uy_fw_2
Alias cov_out_2(19) = co2_co2_2
Alias cov_out_2(20) = h2o_h2o_2
Alias cov_out_2(21) = Ts_Ts_2
Alias cov_out_2(22) = fw_fw_2

'moving average variables
```

```
Dim primes(7)                   'fluctuations from means, consistent with cov_in
Dim move_avg(7)                 'moving averages
Dim x_prod(22)                  'cross products...to compute covariance

'Diagnostic variables.
Public disable_flag_on(2)       'Intermediate processing disable.
    'disable_flag_on(1)        'Set high during site maintenance, flag(7) is set high.
    'disable_flag_on(2)        'Set high when CS7500 (LI-7500) failed to send data.
Public n(2)                     'Number of samples in the on-line covariances.
Public warnings(2)
Alias warnings(1) = csat_warnings    'Number of scans that at least one CSAT3
                                     ' warning flag was on.
Alias warnings(2) = irga_warnings    'Number of scans that the CS7500 (LI-7500)
Public flag(8)

'Measurement variables without delays.
Dim wind_in(5)                  'CSAT3 data, before adding delay.
Dim fw_in                       'TC signal, before adding delay.
Dim tc_ref_in                   'TC reference temperature, before adding delay.

'Arrays to store delayed data.
Dim analog_data(3)   'Three or six scan old data from the Data Table 3_6_scan.
Dim csat_data(5)     'One or four scan old data from the Data Table 1_4_scan.
Dim cov_in(7)        'Array used in the covariance instruction.
Dim j                'Counter variable.
Dim rTime(9)         'Real time from CR5000 clock.
Dim scan_count       'Counts the number scans that have been executed.
Dim hex_number       'Used to break down the diagnostic bits from the CSAT3.
Dim wind_east        'Uy wind in compass coordinate system.
Dim wind_north       'Ux wind in compass coordinate system.
Dim delays_loaded    'A flag that gets set after three or six scans have been executed.
' This flag is to ensure that the Data Table 1_4_scan and 3_6_scan are loaded ‘with data.

'Declare Units
Units Batt_Volt=Volts
Units PA_uS=uSec
Units PA_uS_2=uSec
Units PA_uS_3=uSec
Units PA_uS_4=uSec
Units PA_uS_5=uSec
Units PA_uS_6=uSec
Units AirTC=Deg C
Units RH=%
Units Rain_mm=mm
```

```
Units PTemp_C=Deg C
Units Temp_C=Deg C
Units Temp_C_2=Deg C
Units Temp_C_3=Deg C
Units Temp_C_4=Deg C
Units Solar_Wm2=W/m²
Units Solar_kJ=kJ/m²
Units shf = W/m^2
Units shf_2 = W/m^2
Units BP_mbar=mbar
Units Net_shortwave=W/m²
Units Net_longwave=W/m²
Units TT_C=Deg C
Units SBT_C=Deg C

'Declare Constants
Const SCAN_INTERVAL = 50        '100 (mSec)                    50 (mSec)
Const CSAT_OPT = 10             '10 (Hz)                       20 (Hz)
Const ANALOG_DELAY = 4          '4 (3 scan delay)              7 (6 scan delay)
Const CSAT_DELAY = 2            '2 (1 scan delay)              5 (4 scan delay)
Const GAMMA = 400               'time constant in seconds
Const ANGLE_FROM_NORTH = 240    'Negative when West of North, positive
when East of North.
Const CP = 1003                 'Estimate of heat capacity of air [J/(kg K)].
Const LV = 2440                 'Estimate of the latent heat of vaporization [J/g].
Const RHO = 1.2                 'Estimate for air density at sea level [kg/m^3].
Const SDM_PER = 30              'Default SDM clock speed, 30 uSec bit period.
Const A_0 = 6.107799961         'Coefficients for the sixth order approximating
Const A_1 = 4.436518521e-1          ' saturation vapor pressure polynomial (Lowe,
Const A_2 = 1.428945805e-2          ' Paul R., 1976.:  An approximating polynomial for
Const A_3 = 2.650648471e-4          ' computation of saturation vapor pressure, J. Appl.
Const A_4 = 3.031240396e-6          ' Meteor., 16, 100-103).
Const A_5 = 2.034080948e-8
Const A_6 = 6.136820929e-11

'constants to convert voltage to ppm of  co2.
'Const Crange = 1000
'Const Vrange = 5

'constants to convert voltage to ppt of  h20.
'Const Hrange = 80
Const HFP01SC_CAL = 1000/61.7   'Unique multiplier for HFP01SC 1
(1000/sensitivity).
```

```
Const HFP01SC_CAL_2 = 1000/62.5 'Unique multiplier for HFP01SC 2
(1000/sensitivity).
Const CAL_INTERVAL = 180     'HFP01SC insitu calibration interval (minutes).

'Define Data Tables
DataTable(Met,True,1344)
  CardOut (0,1344)
        DataInterval(0,30,Min,10)
        Average(1,VW,FP2,False)
        Average(1,VW_2,FP2,False)
        Average(1,VW_3,FP2,False)
        Average(1,VW_4,FP2,False)
        Average(1,VW_5,FP2,False)
        Average(1,VW_6,FP2,False)
        Average(1,AirTC,FP2,False)
        Average(1,RH,FP2,False)
        Totalize(1,Rain_mm,FP2,False)
        Average(1,Temp_C,FP2,False)
        Average(1,Temp_C_2,FP2,False)
        Average(1,Temp_C_3,FP2,False)
        Average(1,Temp_C_4,FP2,False)
        Average(1,PTemp_C,FP2,False)
        Average(1,Solar_Wm2,FP2,False)
        Totalize(1,Solar_kJ,IEEE4,False)
        Average (1,shf,IEEE4,shf_cal_on)
  Average (1,shf_2,IEEE4,shf_cal_2_on)
  Average(1,Net_shortwave,FP2,False)
        Average(1,Net_longwave,FP2,False)
        Average(1,BP_mbar,FP2,False)
        Minimum(1,Batt_Volt,FP2,False,False)
        Average(1,PA_uS,FP2,False)
        Average(1,PA_uS_2,FP2,False)
        Average(1,PA_uS_3,FP2,False)
        Average(1,PA_uS_4,FP2,False)
        Average(1,PA_uS_5,FP2,False)
        Average(1,PA_uS_6,FP2,False)
        Sample(1,TT_C,FP2)
        Sample(1,SBT_C,FP2)
EndTable

DataTable(Tips,True,1000)
  DataEvent (0,Rain_mm>0,Rain_mm=0,0)
  Sample (1,Rain_mm,FP2)
EndTable
```

```
DataTable (raw_in,TRUE,1)
  Sample (5,wind_in(1),IEEE4)
  Sample (3,irga(1),IEEE4)
  Sample (1,fw_in,IEEE4)
  Sample (1,tc_ref_in,IEEE4)
EndTable

'Delay the analog measurements by three or six scans.
DataTable (scan_3_6,TRUE,ANALOG_DELAY)
  Sample (1,tc_ref_in,IEEE4)
  Sample (1,fw_in,IEEE4)
EndTable

'Delay the CSAT3 measurements by one or four scans.
DataTable (scan_1_4,TRUE,CSAT_DELAY)
  Sample (5,wind_in(1),IEEE4)
EndTable

'Set flag(8) high to save time series data.  Set flag(5) also
'to break up the time series data file into one hour periods.
DataTable (ts_data,flag(8),-1)
  DataInterval (0,SCAN_INTERVAL,mSec,50)
  CardOut (0,-1)
  Sample (3,wind(1),IEEE4)
  Sample (2,irga(1),IEEE4)
  Sample (1,Ts,IEEE4)
  Sample (1,press,IEEE4)
  Sample (1,diag_csat,IEEE4)
'  Sample (1,diag_irga,IEEE4)
EndTable

'Compute the covariances of vertical wind, co2, h2o, natural log of
' the krypton voltage, sonic temperature, and finewire thermocouple
' temperature, as well as the other cross products, required to rotate
' the data into natural wind coordinates.  This data is output every
' 30 minutes.
DataTable (comp_cov,TRUE,1)
  DataInterval (0,30,min,1)
  Covariance (7,cov_in(1),IEEE4,(disable_flag_on(1) OR disable_flag_on(2) OR NOT
(flag(7))),28)
  WindVector (1,wind_east,wind_north,IEEE4,(disable_flag_on(1) OR NOT
(flag(7))),0,1,2)
EndTable
```

```
'Alternative covariance calculation for 21 days
DataTable (alt_cov,TRUE,1)
  DataInterval (0,30,min,1)
  Average (22,x_prod(1),IEEE4,(disable_flag_on(1) OR disable_flag_on(2) OR NOT
(flag(7))))
EndTable

'This table will hold 28 days of flux data.  This data is output every 30 minutes.
DataTable (flux,TRUE,1344)
  DataInterval (0,30,Min,10)
  CardOut (0,1344)
  Sample (1,Fc,IEEE4)
  Sample (1,LE,IEEE4)
  Sample (1,Hs,IEEE4)
  Sample (1,H,IEEE4)
  Sample (1,u_star,IEEE4)
  Sample (19,cov_out_1(1),IEEE4)
  Sample (1,cov_out_1(23),IEEE4)
  Sample (1,cov_out_1(26),IEEE4)
  Sample (1,cov_out_1(28),IEEE4)

  Average (3,wind(1),IEEE4,(disable_flag_on(1) OR NOT (flag(7)))
  Average (2,irga(1),IEEE4,(disable_flag_on(2) OR NOT (flag(7)))
  Average (1,fw_in,IEEE4,(disable_flag_on(1) OR NOT (flag(7))))
  Average (1,Ts,IEEE4,(disable_flag_on(1) OR NOT (flag(7)))

  Average (1,press,IEEE4,disable_flag_on(2))
  Average (1,tc_ref,FP2,FALSE)

  Sample (1,wnd_dir_compass,FP2)
  WindVector (1,Uy,Ux,FP2,(disable_flag_on(1) OR NOT (flag(7))),0,1,2)
  Average (1,Batt_volt,FP2,FALSE)

  Totalize (1,n(1),IEEE4,FALSE)
  Totalize (2,warnings(1),IEEE4,FALSE)
  Sample (22,cov_out_2(1),IEEE4)
EndTable

'Define subroutines
'Sub hfp01sc_cal 'Begin HFP01SC calibration one minute into every CAL_INTERVAL
minutes.
  'If ( IfTime (1,CAL_INTERVAL,Min) ) Then
    'shf_cal_on = TRUE
```

```
   'Move (shf_mV_0,1,shf_mV_run,1)
   'SW12=TRUE
  'EndIf

  'If ( IfTime (4,CAL_INTERVAL,Min) ) Then
   'Move (shf_mV_180,1,shf_mV_run,1)
   'Move (V_Rf_180,1,V_Rf_run,1)
   'SW12=FALSE
  'EndIf

  'If ( IfTime (19,CAL_INTERVAL,Min) ) Then
   'Move (shf_mV_360,1,shf_mV_run,1)
  'Compute new HFP01SC calibration factors.
     'shf_cal = V_Rf_180*V_Rf_180*128.7/ ABS(((shf_mV_0+shf_mV_360)/2)-
shf_mV_180)
   'Stop filtering data
   'shf_cal_on = FALSE
   'EndIf
'EndSub 'End HFP01SC calibration sequence.

'Sub hfp01sc_cal_2  'Begin HFP01SC PLATE 2 calibration one minute into every
CAL_INTERVAL minutes.
  'If ( IfTime (1,CAL_INTERVAL,Min) ) Then
   'shf_cal_2_on = TRUE
   'Move (shf_2_mV_0,1,shf_2_mV_run,1)
   'SW12=TRUE
  'EndIf

  'If ( IfTime (4,CAL_INTERVAL,Min) ) Then
   'Move (shf_2_mV_180,1,shf_2_mV_run,1)
   'Move (V_Rf_2_180,1,V_Rf_2_run,1)
   'SW12=FALSE
  'EndIf

  'If ( IfTime (19,CAL_INTERVAL,Min) ) Then
   'Move (shf_2_mV_360,1,shf_2_mV_run,1)
  'Compute new HFP01SC calibration factors.
     'shf_cal_2 = V_Rf_180*V_Rf_180*128.7/ ABS(((shf_mV_0+shf_mV_360)/2)-
shf_mV_180)
   'Stop filtering data
   'shf_cal_2_on = FALSE
   'EndIf
'EndSub 'End HFP01SC calibration sequence.
```

```
'Main Program
BeginProg
flag(1) = TRUE
  flag(7) = TRUE
  flag(8) = TRUE

'initiate moving average
  For j = 1 To 7
    move_avg(j) = 0
  Next j

 'Set all CSAT3 variables to NaN.
  For j = 1 To 5
    wind_in(j) = NaN
  Next j

 'Set all CS7500 (LI-7500) variables to NaN.
  For j = 1 To 4
      irga(j) = NaN
  Next j

 'Set the SDM clock speed.
  SDMSpeed (SDM_PER)

Scan(SCAN_INTERVAL,mSec,10,0)

   'Get CSAT3 wind and sonic temperature data.
    CSAT3 (wind_in(1),1,3,91,CSAT_OPT)

   'Get CS7500 (LI-7500) data.
    CS7500 (irga(1),1,7,6)

   'Convert CS7500 (LI-7500) data from molar density [mmol/m^3] to mass density.
   ' 44 [g/mol] - molecular weight of carbon dioxide
   ' 0.018 [g/mmol] - molecular weight of water vapor
    If (NOT (co2 = -99999)) Then (co2 = co2 * 44)
    h2o = h2o * 0.018

                    'Get the battery voltage from the Status Table.
    Batt_Volt = Status.Battery(1,1)

          'If Batt_volt is < 11 Turn OFF IRGA
          If Batt_Volt < 11 Then
                WriteIO (&B10,&B00)
```

```
            flag(1) = TRUE
        EndIf
        If (flag(1) = TRUE AND Batt_Volt > 11.5) Then 'Turning IRGA back ON
            WriteIO (&B10,&B10)
            flag(1) = FALSE
        EndIf

  'Call humedad table.
    'CallTable moisture

  'Display the raw, unshifted turbulence data.
    CallTable raw_in

   'Delay the analog measurements by three or six scans.
    CallTable scan_3_6

   'Delay the CSAT3 measurements by one or four scans.
    CallTable scan_1_4

    If (NOT delays_loaded) Then (scan_count = scan_count + 1)
    If (scan_count = ANALOG_DELAY) Then (delays_loaded = TRUE)

   'Load in analog measurements that have been delayed by three or six scans.
    GetRecord (analog_data(1),scan_3_6,ANALOG_DELAY)
    tc_ref = analog_data(1)
    fw = analog_data(2)

   'Load in CSAT3 measurements that have been delayed by one or four scans.
    GetRecord (csat_data(1),scan_1_4,CSAT_DELAY)
    Ux = csat_data(1)
    Uy = csat_data(2)
    Uz = csat_data(3)
    Ts = csat_data(4)
    diag_csat = csat_data(5)
    wind_east = -1 * csat_data(2)
    wind_north = csat_data(1)

  'Turn on the intermediate processing disable flag when the CSAT3 is reporting NaN, a
    'Lost Trigger (&hf000), No Data (&hf03f), or an SDM error (&hf001).
    If ( (diag_csat = NaN) OR (diag_csat = &hf000) OR (diag_csat = &hf03f) OR
(diag_csat = &hf001))
      disable_flag_on(1) = TRUE
    Else
```

```
        'Check for any warning flags in CSAT3 data.  Filter all measurements 'associated
        with the CSAT3, when the warning flags are set.
      If (diag_csat AND &hf000)
       csat_warnings = 1
       disable_flag_on(1) = TRUE
      Else
       csat_warnings = 0
       disable_flag_on(1) = FALSE
      EndIf
    EndIf

'Keep the four most significant bits of the diagnostic word.
    diag_csat = INT ((diag_csat AND &hf000)/&h1000 + 0.5)

   'Break down the four most significant bits of the diagnostic word
   ' into a delta temperature flag, poor signal lock (tracking flag),
   ' amplitude high flag, and amplitude low flag.
    hex_number = &h0008
    For j = 1 To 4
     If ( ((diag_csat AND hex_number) = hex_number) AND NOT (diag_csat = &h000f) )
       diag_bits(j) = 1
     Else
       diag_bits(j) = 0
     EndIf

     If ( diag_csat = NaN ) Then ( diag_bits(j) = NaN )

     hex_number = INT ((hex_number/&h0002) + 0.5)
    Next j

   'Compute the AGC.
    agc = INT ((diag_irga AND &h000f) * 6.25 + 0.5)

   'Keep the four most significant bits of the CS750 (LI-7500) diagnostic word
   ' and swap bits.
    diag_irga = (NOT (INT ((diag_irga AND &h00f0)/&h0010 + 0.5)) AND &h000f)

   'Turn on the intermediate processing disable flag when the CS7500 (LI-7500)  'has
failed to send data to the CR5000 via SDM.
'    If ( (ABS (co2) >= 99990) OR (co2 = NaN) )
     If ( (co2 >=2000) OR (co2<=0) OR (co2 = NaN) OR (h2o <=0) OR (h2o >=50) )
      disable_flag_on(2) = TRUE
        irga_warnings = 1
     Else
```

```
'Check for any warning flags in CS7500 (LI-7500) data.  Filter all measurements
'associated with the CS7500 (LI-7500), when the warning flags are set.
      If (diag_irga AND &h000f)
        irga_warnings = 1
        disable_flag_on(2) = TRUE
      Else
        irga_warnings = 0
        disable_flag_on(2) = FALSE
      EndIf
    EndIf

   'Decompose the warning flags.  Li-Cor uses reverse logic, e.g. bit set is okay.
   'The program changes the logic, e.g. bit not set is okay.
    hex_number = &h0008
    For j = 1 To 4
      If ( (diag_irga AND hex_number) = hex_number)
        diag_bits(j+4) = 1
      Else
        diag_bits(j+4) = 0
      EndIf

      If ( (ABS (co2) >= 99990) OR (co2 = NaN) ) Then ( diag_bits(j+4) = NaN )
      hex_number = INT ((hex_number/&h2) + 0.5)
    Next j

   'Perform time series and flux processing only after the Table 3_6_scan is loaded with
data.
    If (delays_loaded)

     'Write a file mark to the time series table every day.  The file mark is written 'only to
the PC Card if flag(5) is set high by the station operator and time series 'data are being
stored [flag(8) is high].  Both flag(8) and flag(5) must be set high 'by the station operator
using PC9000 or the CR5000 keyboard.

      If (flag(5) AND flag(8) AND IfTime (0,1440,Min) ) Then (FileMark (ts_data))
      CallTable ts_data

     'Load cov_in() array for the covariance computation.
      cov_in(1) = Uz
      cov_in(2) = Ux
      cov_in(3) = Uy
      cov_in(4) = co2
      cov_in(5) = h2o
      cov_in(6) = Ts
```

```
    cov_in(7) = fw

    CallTable comp_cov

'compute deviations from moving average
        For j = 1 To 7
                If (NOT disable_flag_on(1) AND NOT disable_flag_on(2) AND flag(7)
AND NOT (cov_in(j) = NaN) )
                        move_avg(j)=move_avg(j)*EXP(-1/(CSAT_OPT*GAMMA)) +
cov_in(j)*(1-EXP(-1/(CSAT_OPT*GAMMA)))
                        primes(j)=cov_in(j)-move_avg(j)
                EndIf
        Next j
        If (NOT disable_flag_on(1) AND NOT disable_flag_on(2) AND flag(7))
                x_prod(1)=primes(1)*primes(1)
                x_prod(2)=primes(1)*primes(2)
                x_prod(3)=primes(1)*primes(3)
                x_prod(4)=primes(1)*primes(4)
                x_prod(5)=primes(1)*primes(5)
                x_prod(6)=primes(1)*primes(6)
                x_prod(7)=primes(1)*primes(7)
                x_prod(8)=primes(2)*primes(2)
                x_prod(9)=primes(2)*primes(3)
                x_prod(10)=primes(2)*primes(4)
                x_prod(11)=primes(2)*primes(5)
                x_prod(12)=primes(2)*primes(6)
                x_prod(13)=primes(2)*primes(7)
                x_prod(14)=primes(3)*primes(3)
                x_prod(15)=primes(3)*primes(4)
                x_prod(16)=primes(3)*primes(5)
                x_prod(17)=primes(3)*primes(6)
                x_prod(18)=primes(3)*primes(7)
                x_prod(19)=primes(4)*primes(4)
                x_prod(20)=primes(5)*primes(5)
                x_prod(21)=primes(6)*primes(6)
                x_prod(22)=primes(7)*primes(7)
        EndIf

        CallTable alt_cov

    'Keep track of the number of samples in the covariances.
     If (NOT disable_flag_on(1) AND NOT disable_flag_on(2) AND flag(7))
       n(1) = 1
     Else
```

```
  n(1) = 0
 EndIf

 If (comp_cov.Output(1,1))

  GetRecord (cov_out_1(1),comp_cov,1)

  wnd_dir_compass = wnd_dir_compass + ANGLE_FROM_NORTH
       wnd_dir_compass = wnd_dir_compass MOD 360

 'Compute on-line fluxes.
  Fc = Uz_co2_1
  LE = LV * Uz_h2o_1
  Hs = RHO * CP * Uz_Ts_1
  H = RHO * CP * Uz_fw_1
  tau = SQR ((Uz_Ux_1)^2 + (Uz_Uy_1)^2)
  u_star = SQR (tau)
  tau = RHO * tau

 EndIf

     If (alt_cov.Output(1,1))
          GetRecord (cov_out_2(1),alt_cov,1)
     EndIf

 CallTable flux

EndIf

          'Default Datalogger Battery Voltage measurement Batt_Volt:
          Battery(Batt_Volt)
     'CS616 Water Content Reflectometer measurements VW and PA_uS:
          PortSet(1,1)
          PeriodAvg(PA_uS,1,mV5000,1,0,0,100,5,1,0)
          PortSet(1,0)
          VW=-0.0663+(-0.0063*PA_uS)+(0.0007*PA_uS^2)
     'CS616 Water Content Reflectometer measurements VW_2 and PA_uS_2:
          PortSet(2,1)
          PeriodAvg(PA_uS_2,1,mV5000,2,0,0,100,5,1,0)
          PortSet(2,0)
          VW_2=-0.0663+(-0.0063*PA_uS_2)+(0.0007*PA_uS_2^2)
     'CS616 Water Content Reflectometer measurements VW_3 and PA_uS_3:
          PortSet(3,1)
          PeriodAvg(PA_uS_3,1,mV5000,3,0,0,100,5,1,0)
```

```
        PortSet(3,0)
        VW_3=-0.0663+(-0.0063*PA_uS_3)+(0.0007*PA_uS_3^2)
'CS616 Water Content Reflectometer measurements VW_4 and PA_uS_4:
        PortSet(4,1)
        PeriodAvg(PA_uS_4,1,mV5000,4,0,0,100,5,1,0)
        PortSet(4,0)
        VW_4=-0.0663+(-0.0063*PA_uS_4)+(0.0007*PA_uS_4^2)
'CS616 Water Content Reflectometer measurements VW_5 and PA_uS_5:
        PortSet(5,1)
        PeriodAvg(PA_uS_5,1,mV5000,33,0,0,100,5,1,0)
        PortSet(5,0)
        VW_5=-0.0663+(-0.0063*PA_uS_5)+(0.0007*PA_uS_5^2)
'CS616 Water Content Reflectometer measurements VW_6 and PA_uS_6:
        PortSet(6,1)
        PeriodAvg(PA_uS_6,1,mV5000,34,0,0,100,5,1,0)
        PortSet(6,0)
        VW_6=-0.0663+(-0.0063*PA_uS_6)+(0.0007*PA_uS_6^2)
'HMP45C (6-wire) Temperature & Relative Humidity Sensor 'measurements
AirTC and RH:
        VoltSe(AirTC,1,mV1000,5,0,0,250,0.1,-40.0)
        VoltSe(RH,1,mV1000,6,0,0,250,0.1,0)
        If RH>100 AND RH<108 Then RH=100
        fw=AirTC*1.0
        fw_in=AirTC*1.0
        If (fw_in = NaN) Then fw_in = 0
        'TE525/TE525WS Rain Gauge measurement Rain_mm:
        PulseCount(Rain_mm,1,1,2,0,0.254,0)
        'Wiring Panel Temperature measurement PTemp_C:
        PanelTemp(PTemp_C,250)
        tc_ref=PTemp_C*1.0
        tc_ref_in=PTemp_C*1.0
'Type E (chromel-constantan) Thermocouple measurements Temp_C:
        TCDiff(Temp_C,1,mV20C,6,TypeE,PTemp_C,True,0,250,1,0)
'Type E (chromel-constantan) Thermocouple measurements Temp_C_2:
        TCDiff(Temp_C_2,1,mV20C,7,TypeE,PTemp_C,True,0,250,1,0)
'Type E (chromel-constantan) Thermocouple measurements Temp_C_3:
        TCDiff(Temp_C_3,1,mV20C,8,TypeE,PTemp_C,True,0,250,1,0)
'Type E (chromel-constantan) Thermocouple measurements Temp_C_4:
        TCDiff(Temp_C_4,1,mV20C,9,TypeE,PTemp_C,True,0,250,1,0)
'For TE525MM Rain Gage, use multiplier of 0.1 in PulseCount instruction
        CallTable(Tips)
NextScan
SlowSequence
shf_cal = HFP01SC_CAL
```

```
        shf_cal_2 = HFP01SC_CAL_2
        Scan(1,Sec,1,0)
        'CM3 Pyranometer measurements Solar_kJ and Solar_Wm2:
                VoltDiff(Solar_Wm2,1,mV50,5,True,0,250,75.1880,0)
                If Solar_Wm2<0 Then Solar_Wm2=0
                Solar_kJ=Solar_Wm2*0.2
                'CS100 Barometric Pressure Sensor measurement BP_mbar:
                PortSet(7,1)
                VoltSe(BP_mbar,1,mV5000,7,1,0,250,0.2,600.0)
                BP_mbar=BP_mbar*1.0
                'CNR2 Net radiation measurements
                VoltDiff(Net_shortwave,1,mV20,20,True,200,250,64.3087,0.0)
                VoltDiff(Net_longwave,1,mV20,19,True,0,250,78.6782,0.0)
                'Measure the HFP01SC soil heat flux plate 1.
    VoltDiff(shf_mV,1,mV50,11,FALSE,200,200,1,0)
    shf = shf_mV * shf_cal
   'Measure voltage across the heater (Rf_V).
    VoltDiff(V_Rf, 1, mV5000, 12, FALSE, 200, 200, 0.001, 0)
   'Maintain filtered values for calibration.
    AvgRun (shf_mV_run,1,shf_mV,100)
    AvgRun (V_Rf_run,1,V_Rf,100)
    'Call hfp01sc_cal
         'Measure the HFP01SC soil heat flux plate 2.
    VoltDiff(shf_2_mV,1,mV50,13,FALSE,200,200,1,0)
    shf_2 = shf_2_mV * shf_cal_2
   'Measure voltage across the heater (Rf_V).
    VoltDiff(V_Rf_2, 1, mV5000, 14, FALSE, 200, 200, 0.001, 0)
   'Maintain filtered values for calibration.
    AvgRun (shf_2_mV_run,1,shf_2_mV,100)
    AvgRun (V_Rf_2_run,1,V_Rf_2,100)
    'Call hfp01sc_cal_2
    'Run the Apogee program to calculate the target temperature
          'Measure IRR-P sensor body thermistor temperature
                BrHalf(SBT_C,1,mV5000,31,1,1,5000,True,0,250,1,0)
                SBT_C=24900*(1/SBT_C-1)
                SBT_C=LOG(SBT_C)
                SBT_C=1/(1.129241e-3+2.341077e-4*SBT_C+8.775468e-
8*(SBT_C^3))-273.15
                'Measure IRR-P mV output of thermopile
                VoltDiff(TTmV,1,mV20,15,True,0,250,1,0)
'Calculate slope (m) and offset (b) coefficients for target temperature calculation
        m_8=1340820000+(7418550*SBT_C)+(72785*SBT_C^2)
        b_9=14841900+(118490*SBT_C)+(23378*SBT_C^2)
        'Calculate target temperature using calculated slope (m) and offset (b)
```

```
                SBT_K_7=SBT_C+273.15
                TT_K_6=SBT_K_7^4+TTmV*m_8+b_9
                TT_K_6=SQR(SQR(TT_K_6))
                'Convert target temperature into desired units
                TT_C=TT_K_6-273.15
  'Call Output Tables
                CallTable (Met)
        NextScan
EndProg
```

E.2. Santa Rita Transect Datalogger – CR800

```
'CR800 Series for Hydraprobe Transect #1 in the Santa Rita Experimental Range,
'Watershed 8
'Created by Ryan Templeton 5-5-2010
'Edited by Nolie Pierini 5-5-2011
'Declare Variables and Units
Public BattV
Public HP(2)
Public HP_1(2)
Public HP_2(2)
Public HP_3(2)
Public HP_4(2)
Public HP_5(2)
Public HP_6(2)
Public HP_7(2)
Public HP_8(2)
Public HP_9(2)
Public HP_a(2)
Public HP_b(2)
Public HP_c(2)
Public HP_d(2)
Public HP_e(2)
Public Rain_mm
Public CS450_1(2)
Public CS450_2(2)

Alias HP(1)=Temp_C
Alias HP(2)=SW_wfv
Alias HP_1(1)=Temp_C_1
Alias HP_1(2)=SW_wfv_1
Alias HP_2(1)=Temp_C_2
Alias HP_2(2)=SW_wfv_2
Alias HP_3(1)=Temp_C_3
Alias HP_3(2)=SW_wfv_3
Alias HP_4(1)=Temp_C_4
Alias HP_4(2)=SW_wfv_4
Alias HP_5(1)=Temp_C_5
Alias HP_5(2)=SW_wfv_5
Alias HP_6(1)=Temp_C_6
Alias HP_6(2)=SW_wfv_6
Alias HP_7(1)=Temp_C_7
Alias HP_7(2)=SW_wfv_7
```

Alias HP_8(1)=Temp_C_8
Alias HP_8(2)=SW_wfv_8
Alias HP_9(1)=Temp_C_9
Alias HP_9(2)=SW_wfv_9
Alias HP_a(1)=Temp_C_a
Alias HP_a(2)=SW_wfv_a
Alias HP_b(1)=Temp_C_b
Alias HP_b(2)=SW_wfv_b
Alias HP_c(1)=Temp_C_c
Alias HP_c(2)=SW_wfv_c
Alias HP_d(1)=Temp_C_d
Alias HP_d(2)=SW_wfv_d
Alias HP_e(1)=Temp_C_e
Alias HP_e(2)=SW_wfv_e
Alias CS450_1(1)=Level_1
Alias CS450_1(2)=PTemp_C_1
Alias CS450_2(1)=Level_2
Alias CS450_2(2)=PTemp_C_2

Units BattV=Volts
Units Temp_C=C
Units SW_wfv=Wfv(m3m-3)
Units Temp_C_1=C
Units SW_wfv_1=Wfv(m3m-3)
Units Temp_C_2=C
Units SW_wfv_2=Wfv(m3m-3)
Units Temp_C_3=C
Units SW_wfv_3=Wfv(m3m-3)
Units Temp_C_4=C
Units SW_wfv_4=Wfv(m3m-3)
Units Temp_C_5=C
Units SW_wfv_5=Wfv(m3m-3)
Units Temp_C_6=C
Units SW_wfv_6=Wfv(m3m-3)
Units Temp_C_7=C
Units SW_wfv_7=Wfv(m3m-3)
Units Temp_C_8=C
Units SW_wfv_8=Wfv(m3m-3)
Units Temp_C_9=C
Units SW_wfv_9=Wfv(m3m-3)
Units Temp_C_a=C
Units SW_wfv_a=Wfv(m3m-3)
Units Temp_C_b=C
Units SW_wfv_b=Wfv(m3m-3)

```
Units Temp_C_c=C
Units SW_wfv_c=Wfv(m3m-3)
Units Temp_C_d=C
Units SW_wfv_d=Wfv(m3m-3)
Units Temp_C_e=C
Units SW_wfv_e=Wfv(m3m-3)
Units Rain_mm=mm
Units Level_1=psig
Units PTemp_C_1=C
Units Level_2=psig
Units PTemp_C_2=C

'Define Data Tables
DataTable(Avgs,True,1400)
  DataInterval(0,30,Min,10)
  Minimum(1,BattV,FP2,False,False)
  Average(1,Temp_C,FP2,0)
  Average(1,SW_wfv,FP2,0)
  Average(1,Temp_C_1,FP2,0)
  Average(1,SW_wfv_1,FP2,0)
  Average(1,Temp_C_2,FP2,0)
  Average(1,SW_wfv_2,FP2,0)
  Average(1,Temp_C_3,FP2,0)
  Average(1,SW_wfv_3,FP2,0)
  Average(1,Temp_C_4,FP2,0)
  Average(1,SW_wfv_4,FP2,0)
  Average(1,Temp_C_5,FP2,0)
  Average(1,SW_wfv_5,FP2,0)
  Average(1,Temp_C_6,FP2,0)
  Average(1,SW_wfv_6,FP2,0)
  Average(1,Temp_C_7,FP2,0)
  Average(1,SW_wfv_7,FP2,0)
  Average(1,Temp_C_8,FP2,0)
  Average(1,SW_wfv_8,FP2,0)
  Average(1,Temp_C_9,FP2,0)
  Average(1,SW_wfv_9,FP2,0)
  Average(1,Temp_C_a,FP2,0)
  Average(1,SW_wfv_a,FP2,0)
  Average(1,Temp_C_b,FP2,0)
  Average(1,SW_wfv_b,FP2,0)
  Average(1,Temp_C_c,FP2,0)
  Average(1,SW_wfv_c,FP2,0)
  Average(1,Temp_C_d,FP2,0)
  Average(1,SW_wfv_d,FP2,0)
```

```
  Average(1,Temp_C_e,FP2,0)
  Average(1,SW_wfv_e,FP2,0)
  Totalize(1,Rain_mm,FP2,0)
  Average(1,Level_1,FP2,0)
  Average(1,PTemp_C_1,FP2,0)
  Average(1,Level_2,FP2,0)
  Average(1,PTemp_C_2,FP2,0)
EndTable

DataTable(Tips,True,1800)
  DataEvent (0,Rain_mm>0,Rain_mm=0,0)
  Sample (1,Rain_mm,FP2)
EndTable

DataTable(PT,True,-1)
        DataInterval(0,1,min,10)
        Average(1,Level_1,FP2,0)
        Average(1,Level_2,FP2,0)
EndTable

'Main Program
BeginProg
  Scan(1,Sec,1,0)
    'Default Datalogger Battery Voltage measurement BattV
    Battery(BattV)
    'For TE525MM Rain Gage, use multiplier of 0.1 in PulseCount instruction
    PulseCount(Rain_mm,1,1,2,0,0.1,0)
    'Call Data Tables and Store Data
    CallTable(Tips)
  NextScan

  SlowSequence
  Scan (30,Sec,3,0)
    'Hydraprobe Sensor '0' measurements of Soil Temperature (Temp_C) and Moisture
(SW_wfv)
    SDI12Recorder(HP(),1,"0","M!",1,0)
    'Hydraprobe Sensor '1' measurements of Soil Temperature (Temp_C) and Moisture
(SW_wfv)
    SDI12Recorder(HP_1(),1,"1","M!",1,0)
    'Hydraprobe Sensor '2' measurements of Soil Temperature (Temp_C) and Moisture
(SW_wfv)
    SDI12Recorder(HP_2(),1,"2","M!",1,0)
    'Hydraprobe Sensor '3' measurements of Soil Temperature (Temp_C) and Moisture
(SW_wfv)
```

```
   SDI12Recorder(HP_3(),1,"3","M!",1,0)
   'Hydraprobe Sensor '4' measurements of Soil Temperature (Temp_C) and Moisture
(SW_wfv)
   SDI12Recorder(HP_4(),1,"4","M!",1,0)
   'Hydraprobe Sensor '5' measurements of Soil Temperature (Temp_C) and Moisture
(SW_wfv)
   SDI12Recorder(HP_5(),1,"5","M!",1,0)
   'Hydraprobe Sensor '6' measurements of Soil Temperature (Temp_C) and Moisture
(SW_wfv)
   SDI12Recorder(HP_6(),1,"6","M!",1,0)
   'Hydraprobe Sensor '7' measurements of Soil Temperature (Temp_C) and Moisture
(SW_wfv)
   SDI12Recorder(HP_7(),1,"7","M!",1,0)
   'Hydraprobe Sensor '8' measurements of Soil Temperature (Temp_C) and Moisture
(SW_wfv)
   SDI12Recorder(HP_8(),1,"8","M!",1,0)
   'Hydraprobe Sensor '9' measurements of Soil Temperature (Temp_C) and Moisture
(SW_wfv)
   SDI12Recorder(HP_9(),1,"9","M!",1,0)
   'Hydraprobe Sensor 'a' measurements of Soil Temperature (Temp_C) and Moisture
(SW_wfv)
   SDI12Recorder(HP_a(),3,"A","M!",1,0)
   'Hydraprobe Sensor 'b' measurements of Soil Temperature (Temp_C) and Moisture
(SW_wfv)
   SDI12Recorder(HP_b(),3,"B","M!",1,0)
   'Hydraprobe Sensor 'c' measurements of Soil Temperature (Temp_C) and Moisture
(SW_wfv)
   SDI12Recorder(HP_c(),3,"C","M!",1,0)
   'Hydraprobe Sensor 'd' measurements of Soil Temperature (Temp_C) and Moisture
(SW_wfv)
   SDI12Recorder(HP_d(),3,"D","M!",1,0)
   'Hydraprobe Sensor 'e' measurements of Soil Temperature (Temp_C) and Moisture
(SW_wfv)
   SDI12Recorder(HP_e(),3,"E","M!",1,0)
   'Read Pressure Transducer (CS450) Sensor 'f' every 60 seconds
   SDI12Recorder(CS450_1,3,"F","M1!",1,0)
   SDI12Recorder(CS450_2,3,"G","M1!",1,0)

   CallTable(PT)
   CallTable(Avgs)
  NextScan

EndProg
```

APPENDIX F

SAMPLED DATA PROCESSING

F.1. Eddy Covariance Data Processing

The eddy covariance tower datasets are measured using the three-dimensional sonic anemometer and the open-path gas analyzer at 20 Hz. This data undergoes a filtering process to remove and periods that overlap with rainfall occurrences and periods of equipment malfunction. Next, data is de-spiked for any samples that are +/- 3 standard deviations from the mean. Signal lag is then removed and finally 30 minutes block averaging is performed. Additional corrections to the datasets include coordinate plane rotation (Lee et al., 2004) stability, and density fluctuation (Webb et al., 1980). The 30 minute block averages of fluxes were visually inspected for outliers or values that were out of the expected range. Values that were removed were replaced with a linear interpolation of neighboring data. Negative latent heat fluxes were set to equal zero.

The de-spiking (+/- 3 standard deviation), corrections, and 30 minute block averaging processing was all performed using the EdiRE data software tool made available freely through the University of Edinburgh. To use this data software tool, a processing file describing the corrections to be made to the raw flux data is needed. The processing file used to apply these corrections to the datasets at the eddy covariance tower is included here:

Santa Rita 20 HZ Processing File:

Extract
    From Time =
    To Time =
    Channel = 1
    Label for Signal = SECONDS
Extract
    From Time =
    To Time =
    Channel = 2
    Label for Signal = NANOSECONDS
Extract
    From Time =
    To Time =
    Channel = 3
    Label for Signal = RECORD
Extract
    From Time =
    To Time =
    Channel = 4
    Label for Signal = Ux
Extract
    From Time =
    To Time =

```
        Channel = 5

        Label for Signal = Uy
Extract
        From Time =
        To Time =
        Channel = 6
        Label for Signal = Uz
Extract
        From Time =
        To Time =
        Channel = 7
        Label for Signal = co2
Extract
        From Time =
        To Time =
        Channel = 8
        Label for Signal = h2o
Extract
        From Time =
        To Time =
        Channel = 9
        Label for Signal = Ts
Extract
        From Time =
        To Time =
        Channel = 10
        Label for Signal = press
Extract
        From Time =
        To Time =
        Channel = 11
        Label for Signal = diag_csat
Despike
        From Time =
        To Time =
        Signal = co2
        Standard Deviations = 4
        Spike width = 200
        Spike % consistency = 50
        Replace spikes =
        Storage Label spike count = co2spike
        Outlier Standard Deviations = 4
Despike
```

From Time =
To Time =
Signal = h2o

Standard Deviations = 4
Spike width = 200
Spike % consistency = 50
Replace spikes =
Storage Label spike count = h2ospike
Outlier Standard Deviations = 4

Remove Lag
From Time =
To Time =
Signal = co2
Min Lag (sec) = -1
Lag (sec) = 0.3
Max Lag (sec) = 1
Below Min default (sec) =
Above Max default (sec) =

Remove Lag
From Time =
To Time =
Signal = h2o
Min Lag (sec) = -1
Lag (sec) = 0.3
Max Lag (sec) = 1
Below Min default (sec) =
Above Max default (sec) =

Raw Subset
From Time =
To Time =
Subset start time(s) =
Subset length(s) =
Signal for condition = diag_csat
Condition operators = <
Condition (lower limit) = 4096
Condition upper limit =
Storage Label % removed = csat_error
Number of signals = 6
Signal Subset = Ux
Signal Subset = Uy
Signal Subset = Uz
Signal Subset = co2

Signal Subset = h2o
Signal Subset = press
Signal Subset = Ts
1 chn statistics
From Time =
To Time =
Signal = Ux
Storage Label Mean = Ux_mean
Storage Label Std Dev =
Storage Label Skewness =
Storage Label Kurtosis =
Storage Label Maximum =
Storage Label Minimum =
Storage Label Variance =
Storage Label Turbulent Intensity =
Alt Turbulent Intensity Denominator =
1 chn statistics
From Time =
To Time =
Signal = Uy
Storage Label Mean = Uy_mean
Storage Label Std Dev =
Storage Label Skewness =
Storage Label Kurtosis =
Storage Label Maximum =
Storage Label Minimum =
Storage Label Variance =
Storage Label Turbulent Intensity =
Alt Turbulent Intensity Denominator =
1 chn statistics
From Time =
To Time =
Signal = Uz
Storage Label Mean = Uz_mean
Storage Label Std Dev =
Storage Label Skewness =
Storage Label Kurtosis =
Storage Label Maximum =
Storage Label Minimum =
Storage Label Variance =
Storage Label Turbulent Intensity =
Alt Turbulent Intensity Denominator =
1 chn statistics
From Time =

To Time =
Signal = co2
Storage Label Mean = co2_mean
Storage Label Std Dev =
Storage Label Skewness =
Storage Label Kurtosis =
Storage Label Maximum =
Storage Label Minimum =

Storage Label Variance =
Storage Label Turbulent Intensity =
Alt Turbulent Intensity Denominator =
1 chn statistics
From Time =
To Time =
Signal = h2o
Storage Label Mean = H2O_mean
Storage Label Std Dev =
Storage Label Skewness =
Storage Label Kurtosis =
Storage Label Maximum =
Storage Label Minimum =
Storage Label Variance =
Storage Label Turbulent Intensity =
Alt Turbulent Intensity Denominator =
1 chn statistics
From Time =
To Time =
Signal = press
Storage Label Mean = press_mean
Storage Label Std Dev =
Storage Label Skewness =
Storage Label Kurtosis =
Storage Label Maximum =
Storage Label Minimum =
Storage Label Variance =
Storage Label Turbulent Intensity =
Alt Turbulent Intensity Denominator =
1 chn statistics
From Time =
To Time =
Signal = Ts
Storage Label Mean = Ts_mean
Storage Label Std Dev =

Storage Label Skewness =
Storage Label Kurtosis =
Storage Label Maximum =
Storage Label Minimum =
Storage Label Variance =
Storage Label Turbulent Intensity =
Alt Turbulent Intensity Denominator =

Wind direction

From Time =
To Time =

Signal (u) = Ux
Signal (v) = Uy
Orientation = 240
Wind Direction Components = U+N_V+E
Wind Direction Output = N_0_deg-E_90_deg
Storage Label Wind Direction = Wind_dir
Storage Label Wind Dir Std Dev =

Rotation coefficients

From Time =
To Time =
Signal (u) = Ux
Signal (v) = Uy
Signal (w) = Uz
Storage Label Alpha =
Storage Label Beta =
Storage Label Gamma =
Optional mean u = Ux_mean
Optional mean v = Uy_mean
Optional mean w = Uz_mean

Rotation

From Time =
To Time =
Signal (u) = Ux
Signal (v) = Uy
Signal (w) = Uz
Alpha =
Beta =
Gamma =
Do 1st Rot = x
Do 2nd Rot = x
Do 3rd Rot = x

Gas conversion

From Time =

To Time =
Storage Label = e
Apply to =
Apply by =
Measured variable = H2O_mean
Convert from = Absolute density g/m3
Convert to = Partial Pressure kPa
Temperature (C) = Ts_mean
Pressure (kPa) = press_mean
Water vapour = H2O_mean
Water vapour units = Partial pressure kPa
Molecular weight (g/mole) = 18

Sensible heat flux coefficient
From Time =
To Time =
Storage Label = rhoCp
Apply to =
Apply by =
Vapour pressure (KPa) = e
Min or QC =
Max or QC =
Temperature (C) = Ts_mean
Min or QC =
Max or QC =
Pressure (KPa) = press_mean
Min or QC =
Max or QC =
Alternate rhoCp = 1296.0243
Latent heat of evaporation
From Time =
To Time =
Storage Label = L
Apply to =
Apply by =
Temperature (C) = Ts_mean
Min or QC =
Max or QC =
Pressure (KPa) = press_mean
Min or QC =
Max or QC =
LE flux coef, L = 2440
Friction Velocity
From Time =

To Time =
Signal (u) = Ux
Signal (v) = Uy
Signal (w) = Uz
Storage Label U* (uw) =
Storage Label U* (uw vw) = ustar
2 chn statistics
From Time =
To Time =
Signal = h2o
Signal = Uz
Storage Label Covariance = h2o_cov
Storage Label Correlation =

Storage Label Flux = LE
Flux coefficient = L
2 chn statistics
From Time =
To Time =
Signal = Ts
Signal = Uz
Storage Label Covariance = Ts_cov
Storage Label Correlation =
Storage Label Flux = H
Flux coefficient = rhoCp
2 chn statistics
From Time =
To Time =
Signal = co2
Signal = Uz
Storage Label Covariance = co2_cov
Storage Label Correlation =
Storage Label Flux = FC
Flux coefficient = 1
User defined
From Time =
To Time =
Storage Label = Wind_sp
Apply to =
Apply by =
Equation = SQRT(Ux_mean^2+Uy_mean^2)
Variable = Ux_mean
Variable = Uy_mean

Stability - Monin Obhukov
From Time =
To Time =
Storage Label = Stability
Apply to =
Apply by =
Measurement height (m) = 7
Zero plane displacement (m) = 2.0
Virtual Temperature (C) = Ts_mean
Min or QC =
Max or QC =
H flux (W/m2) = H
Min or QC =
Max or QC =
H flux coef, RhoCp = rhoCp
Min or QC =
Max or QC =
Scaling velocity (m/s) = ustar
Min or QC =
Max or QC =
Frequency response
From Time =
To Time =
Storage Label = H_frqres
Apply to =
Apply by =
Correction type = WX
Measurement height (m) = 7
Zero plane displacement (m) = 2.0
Boundary layer height (m) = 1000
Stability Z/L = Stability
Wind speed (m/s) = Wind_sp
Sensor 1 Flow velocity (m/s) = Wind_sp
Sensor 1 Sampling frequency (Hz) = 20
Sensor 1 Low pass filter type =
Sensor 1 Low pass filter time constant =
Sensor 1 High pass filter type =
Sensor 1 High pass filter time constant =
Sensor 1 Path length (m) = 0.15
Sensor 1 Time constant (s) = 0
Sensor 1 Tube attenuation coef =
Sensor 2 Flow velocity (m/s) = Wind_sp
Sensor 2 Sampling frequency (Hz) = 20
Sensor 2 Low pass filter type =

Sensor 2 Low pass filter time constant =
Sensor 2 High pass filter type =
Sensor 2 High pass filter time constant =
Sensor 2 Path length (m) = 0.15
Sensor 2 Time constant (s) = 0
Sensor 2 Tube attenuation coef =
Path separation (m) =
Get spectral data type = Model
Get response function from = model
Reference Tag =
Reference response condition =
Sensor 1 subsampled =
Sensor 2 subsampled =
Apply velocity distribution adjustment =
Use calculated distribution =
Velocity distribution std dev=
Stability distribution std dev=

Frequency response

From Time =

To Time =
Storage Label = CLE_frqres
Apply to =
Apply by =
Correction type = WX
Measurement height (m) = 7
Zero plane displacement (m) = 2.0
Boundary layer height (m) = 1000
Stability Z/L = Stability
Wind speed (m/s) = Wind_sp
Sensor 1 Flow velocity (m/s) = Wind_sp
Sensor 1 Sampling frequency (Hz) = 20
Sensor 1 Low pass filter type =
Sensor 1 Low pass filter time constant =
Sensor 1 High pass filter type =
Sensor 1 High pass filter time constant =
Sensor 1 Path length (m) = 0.15
Sensor 1 Time constant (s) = 0
Sensor 1 Tube attenuation coef =
Sensor 2 Flow velocity (m/s) = Wind_sp
Sensor 2 Sampling frequency (Hz) = 20
Sensor 2 Low pass filter type =
Sensor 2 Low pass filter time constant =
Sensor 2 High pass filter type =

Sensor 2 High pass filter time constant =
Sensor 2 Path length (m) = 0.125
Sensor 2 Time constant (s) = 0.0
Sensor 2 Tube attenuation coef =
Path separation (m) = 0.05
Get spectral data type = Model
Get response function from = model
Reference Tag =
Reference response condition =
Sensor 1 subsampled =
Sensor 2 subsampled =
Apply velocity distribution adjustment =
Use calculated distribution =
Velocity distribution std dev=
Stability distribution std dev=
Mathematical operation
From Time =
To Time =
Storage Label = Hc
Apply to =
Apply by =

Measured variable A = H
Operation = *
Measured variable B = H_frqres
Mathematical operation
From Time =
To Time =
Storage Label = LEc
Apply to =
Apply by =
Measured variable A = LE
Operation = *
Measured variable B = CLE_frqres
Mathematical operation
From Time =
To Time =
Storage Label = FCc
Apply to =
Apply by =
Measured variable A = FC
Operation = *
Measured variable B = CLE_frqres
Webb correction

From Time =
To Time =
Storage Label = WPL_LE
Apply to =
Apply by =
Scalar value type = Partial Pressure (kPa)
Scalar value = e
Min or QC =
Max or QC =
Water vapour value type = Partial Pressure (kPa)
Water vapour value = e
Min or QC =
Max or QC =
Temperature (C) = Ts_mean
Min or QC =
Max or QC =
Pressure (KPa) = press_mean
Min or QC =
Max or QC =
H flux (W/m2) = Hc
Min or QC =
Max or QC =
LE flux (W/m2) = LEc

Min or QC =
Max or QC =
H flux coef, RhoCp = rhoCp
Min or QC =
Max or QC =
LE flux coef, L = L
Min or QC =
Max or QC =
Scalar molecular wt. = 18
Scalar flux type = LE (W/m2)
Scalar flux coefficient = L
Min or QC =
Max or QC =
Alternate water vapour pressure (kPa) =
Alternate temperature (C) =
Alternate pressure (kPa) =

Mathematical operation
From Time =
To Time =

Storage Label = LEcw
Apply to =
Apply by =
Measured variable A = LEc
Operation = +
Measured variable B = WPL_LE

Webb correction

From Time =
To Time =
Storage Label = WPL_FC
Apply to =
Apply by =
Scalar value type = Density (mg/m3)
Scalar value = co2_mean
Min or QC =
Max or QC =
Water vapour value type = Partial Pressure (kPa)
Water vapour value = e
Min or QC =
Max or QC =
Temperature (C) = Ts_mean
Min or QC =
Max or QC =
Pressure (KPa) = press_mean
Min or QC =
Max or QC =

H flux (W/m2) = Hc
Min or QC =
Max or QC =
LE flux (W/m2) = LEcw
Min or QC =
Max or QC =
H flux coef, RhoCp = rhoCp
Min or QC =
Max or QC =
LE flux coef, L = L
Min or QC =
Max or QC =
Scalar molecular wt. = 44
Scalar flux type = Fx (mg/m2/s)
Scalar flux coefficient = 1
Min or QC =
Max or QC =

Alternate water vapour pressure (kPa) =
Alternate temperature (C) =
Alternate pressure (kPa) =
Mathematical operation
From Time =
To Time =
Storage Label = FCcw
Apply to =
Apply by =
Measured variable A = FCc
Operation = +
Measured variable B = WPL_FC
Plot Value
From Time =
To Time =
Left Axis Value = Hc
Right Axis Value = H
Left Axis Minimum =
Left Axis Maximum =
Right Axis Minimum =
Right Axis Maximum =
Match Left/Right Axes =
Plot Value
From Time =
To Time =
Left Axis Value = LEcw
Right Axis Value = LEc
Left Axis Minimum =

Left Axis Maximum =
Right Axis Minimum =
Right Axis Maximum =
Match Left/Right Axes =
Plot Value
From Time =
To Time =
Left Axis Value = LEc
Right Axis Value = LE
Left Axis Minimum =
Left Axis Maximum =
Right Axis Minimum =
Right Axis Maximum =
Match Left/Right Axes =
Plot Value

From Time =
To Time =
Left Axis Value = LEcw
Right Axis Value = Hc
Left Axis Minimum =
Left Axis Maximum =
Right Axis Minimum =
Right Axis Maximum =
Match Left/Right Axes =

Plot Value
From Time =
To Time =
Left Axis Value = FCcw
Right Axis Value = FCc
Left Axis Minimum =
Left Axis Maximum =
Right Axis Minimum =
Right Axis Maximum =
Match Left/Right Axes =

APPENDIX G

POINT-SCALE AND BASIN-SCALE MODELING PARAMETERS

G.1 Point-Scale Soil and Vegetation Modeling Parameters

2011	**Soil Parameters**	**ID**	**Ks [mm/hr]**	**thetaS [-]**	**thetaR [-]**	**m [-]**	**PsiB [mm]**	**f [mm^{-1}]**	**As [-]**	**Au [-]**	**n [-]**	**ks [J/msK]**	**Cs [J/m^{3}K]**
	Grass Cover	1	2.5	0.24	0.03	2	0	0.01	1	1	0.4	1.1	1200000
	Vegetation Parameters	**ID**	**P [-]**	**S [mm]**	**K [mm/hr]**	**b2 [mm^{-1}]**	**Al [-]**	**h [m]**	**Kt [-]**	**Rs [s/m]**	**V [-]**	**LAI [-]**	
	Grass	1	0.301	0.4	0.12	4.7	0.12	0.50	0.940	115	0.5	0.8	
2012	**Soil Parameters**	**ID**	**Ks [mm/hr]**	**thetaS [-]**	**thetaR [-]**	**m [-]**	**PsiB [mm]**	**f [mm^{-1}]**	**As [-]**	**Au [-]**	**n [-]**	**ks [J/msK]**	**Cs [J/m^{3}K]**
	Grass Cover	1	2.5	0.24	0.03	2	0	0.01	1	1	0.4	1.1	1200000
	Vegetation Parameters	**ID**	**P [-]**	**S [mm]**	**K [mm/hr]**	**b2 [mm^{-1}]**	**Al [-]**	**h [m]**	**Kt [-]**	**Rs [s/m]**	**V [-]**	**LAI [-]**	
	Grass	1	0.301	0.4	0.12	4.7	0.12	0.50	0.940	115	0.5	0.8	

2011	**Model**	**IWT [mm] from surface**
	Point	900
	Watershed 7	900
	Watershed 8	900
2012	**Model**	**IWT [mm] from surface**
	Point	800
	Watershed 7	800
	Watershed 8	800

G.2 Basin-Scale Soil and Vegetation Modeling Parameters

	Soil Parameters	ID	Ks [mm/hr]	thetaS [-]	thetaR [-]	m [-]	PsiB [mm]	f [mm^{-1}]	As [-]	Au [-]	n [-]	ks [J/msK]	Cs [J/m^3K]
2011	Grass Cover	1	2.5	0.24	0.005	2	0	0.01	1	1	0.4	1.1	1200000
	Mesquite Cover	2	6	0.29	0.005	1.06	0	0.01	1	1	0.38	4	1200000
	Bare Cover	3	0.6	0.34	0.005	0.8	0	0.01	1	1	0.45	3	1200000
	Vegetation Parameters	**ID**	**P [-]**	**S [mm]**	**K [mm/hr]**	**b2 [mm^{-1}]**	**Al [-]**	**h [m]**	**Kt [-]**	**Rs [s/m]**	**V [-]**	**LAI [-]**	
	Grass	1	0.301	0.4	0.12	4.7	0.12	0.50	0.940	115	0.5	0.8	
	Mesquite	2	0.091	0.8	0.12	4.7	0.08	1.70	0.800	60	0.65	1.6	
	Bare	3	1.0	0	0.12	4.7	0.18	0.05	0.980	72	0.08	0.02	
2012	**Soil Parameters**	**ID**	**Ks [mm/hr]**	**thetaS [-]**	**thetaR [-]**	**m [-]**	**PsiB [mm]**	**f [mm^{-1}]**	**As [-]**	**Au [-]**	**n [-]**	**ks [J/msK]**	**Cs [J/m^3K]**
	Grass Cover	1	2.5	0.24	0.005	2	0	0.01	1	1	0.4	1.1	1200000
	Mesquite Cover	2	6	0.29	0.005	1.06	0	0.01	1	1	0.38	4	1200000
	Bare Cover	3	0.6	0.34	0.005	0.8	0	0.01	1	1	0.45	3	1200000
	Vegetation Parameters	**ID**	**P [-]**	**S [mm]**	**K [mm/hr]**	**b2 [mm^{-1}]**	**Al [-]**	**h [m]**	**Kt [-]**	**Rs [s/m]**	**V [-]**	**LAI [-]**	
	Grass	1	0.301	0.4	0.12	4.7	0.12	0.50	0.940	115	0.5	0.8	
	Mesquite	2	0.091	0.8	0.12	4.7	0.08	1.70	0.800	60	0.65	1.6	
	Bare	3	1.0	0	0.12	4.7	0.18	0.05	0.980	72	0.08	0.02	

APPENDIX H

ENVIRONMENTAL SENSOR NETWORK DATASETS FROM JUNE 2011 TO SEPTEMBER 2012

H.1 Environmental Sensor Network Datasets from June 2011 to September 2012

In this section, the raw datasets collected from the Santa Rita field sites from June 2011 to September 2012 are presented in the folder "Appendix H." The folders are organized by date of collection. In each folder, the raw datasets from transects 1 to 4 and the eddy covariance tower are included. The datasets from each transect include the number of tips for each rain gauge and the 30 minute averages from the soil moisture and temperature sensors. In addition, transects 1 and 2 include the 1 minute pressure transducer data. The eddy covariance tower data includes raw flux data, with H_2O and CO_2 concentrations and wind speed in three directions recorded at 20 hertz (Hz). These fluxes are stored in a file named "2622.ts_data.dat." Also, 30 minute averages of soil moisture at six depths, relative humidity, air temperature, surface temperature, two ground heat flux measurements, barometric pressure, incoming solar radiation, net longwave and net shortwave radiation and rain gauge tips are included. Missing data periods, due to equipment malfunction or thefts, are summarized in Figure 7 in Section 2.4. A table is included to describe the folders containing available data sets. A second table is used to describe the data associated with the file names within each folder. All specified data folders are located in:

F:\NicolePierini_ThesisAppendices\Appendix H**Folder Name\File Name**

Folder Name	Date Range
6.9.11	5/26/2011 to 6/9/2011
6.28.11	6/9/2011 to 6/28/2011
7.20.11	6/28/2011 to 7/20/2011
7.23.11	7/20/2011 to 7/23/2011
7.28.11	7/23/2011 to 7/28/2011
8.4.11	7/28/2011 to 8/4/2011
9.3.11	8/4/2011 to 9/3/2011
9.17.11	9/3/2011 to 9/17/2011
10.13.11	9/17/2011 to 10/13/2011
11.11.11	10/13/2011 to 11/11/2011
12.15.11	11/11/2011 to 12/15/2011
1.10.12	12/15/2011 to 1/10/2012
2.3.12	1/10/2012 to 2/3/2012
2.8.12	2/3/2012 to 2/8/2012
3.3.12	2/8/2012 to 3/3/2012
3.22.12	3/3/2012 to 3/22/2012
4.18.12	3/22/2012 to 4/18/2012
5.7.12	4/18/2012 to 5/7/2012
5.25.12	5/7/2012 to 5/25/2012
6.6.12	5/25/2012 to 6/6/2012
7.4.12	6/6/2012 to 7/4/2012
7.18.12	7/4/2012 to 7/18/2012
8.16.12	7/18/2012 to 8/16/2012
9.13.12	8/16/2012 to 9/13/2012
10.7.12	9/13/2012 to 10/7/2012

Dataset	File Name
Transect 1 Averages	**CR800_1_Avgs.dat**
Transect 2 Averages	**CR800_2_Avgs.dat**
Transect 3 Averages	**CR800_3_Avgs.dat**
Transect 4 Averages	**CR800_4_Avgs.dat**
Transect 1 Rain Gauge Tips	**CR800_1_Tips.dat**
Transect 2 Rain Gauge Tips	**CR800_2_Tips.dat**
Transect 3 Rain Gauge Tips	**CR800_3_Tips.dat**
Transect 4 Rain Gauge Tips	**CR800_4_Tips.dat**
Transect 1 Pressure Transducers	**CR800_1_PT.dat**
Transect 2 Pressure Transducers	**CR800_2_PT.dat**
EC Tower 20 Fluxes	**2622.ts_data.dat**
EC Tower Averages	**CR5000_Met_2012.dat**
EC Tower Rain Gauge Tips	**CR5000_Tips.dat**

APPENDIX I

GIS REPOSITORY FOR SANTA RITA WATERSHEDS 7 AND 8

I.1 Raster and Vector Datasets for Santa Rita Watersheds 7 and 8

In this section, the raster and vector datasets used for each Santa Rita study basin is presented in the folder "Appendix I\Raster_and_Vector\." This folder contains shapefiles and raster grids. The lists and descriptions of each shape file are given below:

subbasin1.shp: Subbasin within watershed 8 derived from internal flume 1.

subbasin2.shp: Subbasin within watershed 8 derived from internal flume 2.

subbasin3.shp: Subbasin within watershed 8 derived from internal flume 3.

ws7_poly.shp: Watershed 7 boundary polygon.

ws8_poly.shp: Watershed 8 boundary polygon.

ws7_stream: Watershed 7 stream network.

ws8_stream: Watershed 8 stream network.

The list and descriptions of the raster files are given below:

canopyzero: Canopy heights derived from the bare earth DEM and the canopy DEM.

dem_final_no0: Bare earth DEM as derived from LiDAR products and processed to fill any holes or missing data points.

raster_adj14: Adjusted bare earth DEM to obtain flow directions and accumulations to match what was observed in the field.

veg_123_meter: Vegetation classification at 1 meter resolution derived for watersheds 7 and 8. Vegetation classification of 1 is grass, 2 is mesquite, and 3 is bare.

The folders containing the GIS data used to derive TINs through TIAP are Appendix I\Raster_and_Vector\sr7_tin for watershed 7 and Appendix I\Raster_and_Vector\sr8_tin for watershed 8.

Additionally, differential GPS (dGPS) points were taken at the field sites. A summary of the file names and descriptions can be found below. The pathname of these points is Appendix I\Raster_and_Vector\dGPS.

ARSRainGauge.shp: Location of rain gauge operated by the ARS.

DeploymentWatershedBoundary.shp: Field estimation of watershed 8 boundary.

Export_OutletFlume7.shp: Location of watershed 7 outlet flume.

Export_SM2_GHI.shp: Location of soil moisture and temperature sensors G, H, and I at transect 2.

Export_WS7SteamNetwork.shp: Field estimation of stream network in watershed 7.

flume1.shp: Internal flume 1 location.

flume2.shp: Internal flume 2 location.

flume3.shp: Internal flume 3 location.

OutletFlume.shp: Watershed 8 outlet flume location.

RainGauge1.shp: Location of rain gauge at transect 1.

RainGauge2.shp: Location of rain gauge at transect 2.

RainGauge3.shp: Location of rain gauge at transect 3.

RainGauge4.shp: Location of rain gauge at transect 4.

RainGaugeAtTower: Location of rain gauge at the eddy covariance tower site.

StreamNetwork.shp: Field estimation of the stream network in watershed 8.

tower.shp: Eddy covariance tower location.

transect1.shp: Five soil moisture and temperature sensor locations along transect 1, plus the location of the transect 1 datalogger.

transect2.shp: Five soil moisture and temperature sensor locations along transect 2, plus the location of the transect 2 datalogger.

transect3.shp: Five soil moisture and temperature sensor locations along transect 3, plus the location of the transect 3 datalogger.

transect4.shp: Five soil moisture and temperature sensor locations along transect 4, plus the location of the transect 4 datalogger.

I.2 Light Detection and Radar (LiDAR) Datasets

In this section, the raw and processed light detection and radar (LiDAR) products are presented in "Appendix I\LiDAR\." The coordinate system for the data is: NAD_1983_HARN_StatePlane_Arizona_Central_FIPS_0202_Feet_Intl.

A list of the files and descriptions included in this folder is below:

Appendix I\LiDAR\OrthoImage\: Includes the orthoimage obtained from the data collection flight.

AppendixI\LiDAR\RawPoints\: Includes the raw points obtained from the data collection flight. Pt6_LAStoMpt files are the data that was imported from the raw .las data into ArcGIS using the LAS to Multipoint function. A resolution of 0.6 was specified as it was the recommended resolution from the organization that conducted the flight.

APPENDIX J

MODEL SETUP FOR SANTA RITA WATERSHEDS 7 AND 8

J.1 Point-Scale Model Setup for Watershed 8 for Summer 2011 and 2012

The model setup for the point-scale eddy covariance tower simulations is presented in the folder, "Appendix J\Point\." The model setup follows the conventions of tRIBS model organization. Both the validation (summer 2012) and calibration (summer 2011) periods are included and the tRIBS model used to run both is found at: Appendix J\Point\tribs. The following list gives the file name paths:

Calibration Period – Summer 2011: Appendix J\Point\2011

Input: Appendix J\Point\2011\Input

Output: Appendix J\Point\2011\Output\2011\hyd or voronoi

Rain: Appendix J\Point\2011\Rain

Weather: Appendix J\Point\2011\Weather

The *.in* file to run the model is: tower2011_elem.in.

Validation Period – Summer 2012: Appendix J\Point\2012

Input: Appendix J\Point\2012\Input

Output: Appendix J\Point\2012\Output\2012\hyd or voronoi

Rain: Appendix J\Point\2012\Rain

Weather: Appendix J\Point\2012\Weather

The *.in* file to run the model is: tower2012_elem.in.

J.2 Basin-Scale Model Setup for Watersheds 7 and 8 for Summer 2011 and 2012

The model setups for the basin-scale simulations for watershed 7 is presented in the folder, "Appendix J\Basin\SantaRita7" and the model setup for the basin-scale simulations for watershed 8 is presented in the folder, "Appendix J\Basin\SantaRita8." The model setup follows the conventions of tRIBS model organization. Both the validation (summer 2012) and calibration (summer 2011) periods are included. In addition, the actual tRIBS model used for each simulation is included, found at Appendix J\SantaRita7\tribs for watershed 7 or Appendix J\SantaRita8\tribs for watershed 8. The following list gives the file name paths:

Watershed 7 Calibration Period – Summer 2011: Appendix J\SantaRita7\2011

Input: Appendix J\SantaRita7\2011\Input

Output: Appendix J\SantaRita7\2011\Output\2011\hyd or voronoi

Base name for spatial output: ws7Run19

Base name for spatial output, bare-only model: ws7bare

Base name for spatial output, grass-only model: ws7grass

Base name for spatial output, mesquite-only model: ws7mesquite

Rain: Appendix J\SantaRita7\2011\Rain

Weather: Appendix J\SantaRita7\2011\Weather

The *.in* file to run the model is: ws7Run19.in. To run the bare-only vegetation model, use: ws7bare.in. To run the grass-only vegetation model, use: ws7grass.in and to run the mesquite-only vegetation model, use: ws7mesquite.in.

Watershed 7 Validation Period – Summer 2012: Appendix J\SantaRita7\2012

Input: Appendix J\SantaRita7\2012\Input

Output: Appendix J\SantaRita7\2012\Output\2012\hyd or voronoi

Base name for spatial output: ws7Run19

Base name for spatial output, bare-only model: ws7bare

Base name for spatial output, grass-only model: ws7grass

Base name for spatial output, mesquite-only model: ws7mesquite

Rain: Appendix J\SantaRita7\2012\Rain

Weather: Appendix J\SantaRita7\2012\Weather

The *.in* file to run the model is: ws7Run19.in. To run the bare-only vegetation model, use: ws7bare.in. To run the grass-only vegetation model, use: ws7grass.in and to run the mesquite-only vegetation model, use: ws7mesquite.in.

Watershed 8 Calibration Period – Summer 2011: Appendix J\SantaRita8\2011

Input: Appendix J\SantaRita8\2011\Input

Output: Appendix J\SantaRita8\2011\Output\2011\hyd or voronoi

Base name for spatial output: ws8Run19

Base name for spatial output, bare-only model: ws8bare

Base name for spatial output, grass-only model: ws8grass

Base name for spatial output, mesquite-only model: ws8mesquite

Rain: Appendix J\SantaRita8\2011\Rain

Weather: Appendix J\SantaRita8\2011\Weather

The *.in* file to run the model is: ws8Run19.in. To run the bare-only vegetation model, use: ws8bare.in. To run the grass-only vegetation model, use: ws8grass.in and to run the mesquite-only vegetation model, use: ws8mesquite.in.

Watershed 8 Validation Period – Summer 2012: Appendix J\SantaRita8\2012

Input: Appendix J\SantaRita8\2012\Input

Output: Appendix J\SantaRita8\2012\Output\2012\hyd or voronoi

Base name for spatial output: ws8Run19

Base name for spatial output, bare-only model: ws8bare

Base name for spatial output, grass-only model: ws8grass

Base name for spatial output, mesquite-only model: ws8mesquite

Rain: Appendix J\SantaRita8\2012\Rain

Weather: Appendix J\SantaRita8\2012\Weather

The *.in* file to run the model is: ws8Run19.in. To run the bare-only vegetation model, use: ws8bare.in. To run the grass-only vegetation model, use: ws8grass.in and to run the mesquite-only vegetation model, use: ws8mesquite.in.

APPENDIX K

PHOTOGRAPHS OF WATERSHED 7 AND 8 STUDY SITES

K.1 Photographs of Watershed 7 and 8 Study Sites

Photographs taken at the watershed 7 and 8 study sites are presented in the folder, "Appendix K." Photographs include images of the sensors for different times of the year, images of the vegetation at different times of the year, and images of the flumes and eddy covariance tower. The following table describes the folder organization of the images available. It specifies the date of the photographs included in the folder, the number of photographs, and a brief description of the types of photographs included. All specified data folders are located in:

F:\NicolePierini_ThesisAppendices\Appendix K**Folder Name**\

Folder Name	**Photograph Date**	**Number of Photos**	**Summary of Contents and Comments**
1.17.11	1/7/2011	12	Views from Russ Scott's EC Tower. WS 8 Flume.
2.15.11	2/15/2011	9	General WS8 Photos.
3.31.11	3/31/2011	28	Internal flume location possibilities, EC Tower site.
5.20.11	5/16/2011 to 5/20/2011	210	Field Deployment. All sensors and sensor locations. EC Tower Equipment.
7.20.11	7/20/2011	50	All transect sensors, internal flumes, and EC sensors. Views from EC Tower.
7.28.11	7/28/2011	43	Green-up at internal flumes and in watershed 8.
8.4.11	8/4/2011	66	All transect sensors and internal flumes.
9.3.11	9/3/2011	35	Approximately half of the transect sensors.
9.17.11	9/17/2011	90	All transect sensors, internal flumes, and EC sensors. Views from EC Tower.
4.18.12	4/18/2012	54	All transect sensors and internal flumes. Watershed 7 flume.
5.3.12	5/3/2012	9	Ecohydrology class field trip. Helicopter in flight.
9.13.12	9/13/2012	25	All transect sensors.